

University of Central Florida

STARS

Electronic Theses and Dissertations, 2020-

2022

Heat Transfer Characterization of Carbon Dioxide in Micro Impinging Jet(s) Near Critical Conditions

Stephen Adeoye

University of Central Florida



Part of the [Heat Transfer, Combustion Commons](#)

Find similar works at: <https://stars.library.ucf.edu/etd2020>

University of Central Florida Libraries <http://library.ucf.edu>

This Doctoral Dissertation (Open Access) is brought to you for free and open access by STARS. It has been accepted for inclusion in Electronic Theses and Dissertations, 2020- by an authorized administrator of STARS. For more information, please contact STARS@ucf.edu.

STARS Citation

Adeoye, Stephen, "Heat Transfer Characterization of Carbon Dioxide in Micro Impinging Jet(s) Near Critical Conditions" (2022). *Electronic Theses and Dissertations, 2020-*. 1167.

<https://stars.library.ucf.edu/etd2020/1167>

HEAT TRANSFER CHARACTERIZATION OF CARBON DIOXIDE IN MICRO
IMPINGING JET(S) NEAR CRITICAL CONDITIONS

by

STEPHEN A. ADEOYE

B.Eng. Federal University of Technology Akure, 2018

A dissertation submitted in partial fulfilment of the requirements
for the degree of Doctor of Philosophy
in the Department of Mechanical and Aerospace Engineering
in the College of Engineering and Computer Science
at the University of Central Florida
Orlando, Florida

Summer Term
2022

Major Professor: Yoav Peles

© 2022 Stephen Adeoye

ABSTRACT

The continuous growth and demand of increased operating performances of electronics has brought about an increase in the chip power density posing threat to the thermal management of these devices. Although numerous thermal solutions ranging from passive to active cooling together with a variety of working fluids have been adopted, however, the question whether these available cooling methods could meet up with the ever-growing need for increased operating performances is a concerning one. Jet impingement cooling has been effectively used in many industrial applications due to its high heat transfer capability. The limited study at the micro scale suggests that it exhibits excellent heat transfer performance relative to conventional parallel flow in microchannels. Recently, Carbon dioxide in its supercritical state (304 K and 7.3 MPa) has been proven to be an excellent working fluid in dissipating high heat fluxes. Owing to the properties of this fluid (sCO₂) and its high specific heat near the pseudocritical point, the heat transfer rate can be enhanced significantly compared traditional working fluids. However, knowledge about the heat transfer characteristics of micro jet impingement with Carbon dioxide in this state are lacking. In addition, flow boiling has been recognized to significantly enhance heat transfer rate due to its large thermal capacity giving an opportunity to further enhance the cooling ability of Carbon dioxide.

In line of this continuous innovation the flow and the heat transfer characteristic of micro jet impingement with CO₂ in both single-phase and two-phase were experimentally studied. A micro fluidic device was manufactured leveraging MEMS techniques. The micro device included a circular serpentine heater of diameter 2.01 mm and three resistance temperature detectors (RTDs) sputtered on a glass substrate made of fused silica, providing heating and temperature

measurements, respectively. The heater, RTDs and their vias were sputtered with the calculated lengths, widths and thicknesses to achieve the desired resistances. The RTDs were arranged on the heater in a concentric manner to measure the average radial temperature distribution as the flow was assumed to be symmetric. The effects of the working fluid was investigated under governing parameters such as radial position, heat flux, mass flow rate, inlet temperature and inlet pressure. Results from the single-phase investigation showed a higher sensitivity of the heat transfer rate to the proximity to the pseudocritical temperature of the fluid with the optimum heat transfer rate recorded around the pseudocritical temperature subject to the increased specific heat around this region. By utilizing the flow boiling process, a further enhancement was observed pre the critical heat flux condition, suggesting a need to operating within the nucleate boiling region in its industrial adoption. It was recorded that the single jet performed better than the multi jet as a result of the interjet spacing which governs the effect of the colliding jets. Finally, several correlations with minimal mean absolute errors were introduced due to discrepancies from literatures.

My family and friends

ACKNOWLEDGEMENT

This dissertation and my PhD journey have been a cumulative effort of a number of people who have continuously geared and shaped me to who I am today. First and foremost, I would like to whole-heartedly give all gratitude to God for life and giving me a purpose within this society. I give the warmest appreciation to my academic advisor, Dr. Yoav Peles for the opportunity to work with him, his guidance and continuous mentorship throughout my program. I whole-heartedly appreciate him for believing in my abilities and for his continuous push which opened me to new potentials in myself. Dr. Peles exercised professional patience and trust in my ability which enhanced my overall research skills. I would like to extend my gratitude to Dr. Shawn Putnam, Dr. Louis Chow, and Dr. Aravinda Kar who served as my dissertation committee. This would not have been possible without their feedbacks, suggestions, and advice towards my research. I would like to give thanks to my past and present lab partners – Dr. Arash Nayebzadeh, Dr. Ehsan Sourtiji, Dr. Mostafa Asadzadzeh, Anatoly Parahovnik, Pranzal Ahmed and Soroush Niazi for their support and insightful conversations. Special thanks to Anatoly Parahovnik for his highly impactful involvement in my research, his support and exchange of ideas both in and out of the lab. I give sincere thanks to the management and staff at Cornell Nanoscale Facility – Michael Skvarla, Jeremy Clark, Garry Bordonaro and a lot more for the knowledge passed during my microfabrication experience. Sincere thanks to UCF MAE staff and Advising faculty: Dr. Jihan Gou, Lynn Grabenhorst, Noreen Hodapp, Rodrigo Lenartowicz, Tami Salter and a lot more. I thank you all for your involvement in ensuring I had an eventful journey at UCF. I thank the board and members of Tau Beta Pi Honor society for the mentorships and exposure I gained through my

involvements with this organization. I am sincerely grateful for my friends who were a constant source of motivation and fuel: Emmanuel Okogbue, Abigail Adeyeye, Gift Idama, Adedamola Okunmadewa, Ibrahim Bilau, Richard Owoputi, John Ajiniran, Ileri Giwa, Omotoye Adekoya, Richard Eruba, Tosin Adebayo, Tofunmi Ilesanmi, Jordan Ijewere, and a lot more that I cannot fit in due to limited space. I sincerely appreciate every one of you. Most importantly I am extremely grateful to my family for their nonstop support and guidance throughout my academic journey. My dad, Mr. Taiwo Adeoye, my mum, Mrs. Bolaji Adeoye and my two awesome sisters, Biola Adeoye and Biodun Adeoye, we did it! Thank you!

TABLE OF CONTENTS

LIST OF FIGURES	xii
LIST OF TABLES	xvi
LIST OF ABBREVIATIONS.....	xvii
CHAPTER ONE: INTRODUCTION.....	1
1.1. Moore’s Law and Advances in Microfabrication	1
1.2. Jet Impingement	5
1.2.1. Background	5
1.2.2. Jet Hydrodynamics.....	6
1.2.3. Multiple Jets.....	9
1.2.4. Highlighted factors affecting the heat transfer of impinging jet(s).....	11
1.3. Carbon Dioxide	17
1.3.1. Supercritical Carbon Dioxide (sCO ₂)	19
1.4. Flow Boiling.....	20
1.5. Objectives.....	22
1.6. Dissertation Overview.....	23
CHAPTER TWO: METHODOLOGY	26
2.1. Microfluidic Device	27

2.1.1.	Heat generation and temperature measurement	27
2.1.2.	Device design and layout	28
2.1.3.	Mask Layout and Configuration	29
2.1.4.	Microfabrication	35
2.1.5.	Conclusion	42
2.2.	Micro Device Housing	44
2.2.1.	Fluid Flow Direction.....	47
2.2.2.	Electrical connection.....	49
2.2.3.	Conclusion	49
2.3.	Experimental Loop.....	51
2.4.	Data Acquisition and Processing.....	53
2.5.	Data Reduction.....	56
2.6.	Heat Loss Estimation	59
CHAPTER THREE: SINGLE MICRO IMPINGING JET WITH SCO ₂		61
3.1.	Introduction	61
3.2.	Results And Discussion.....	63
3.2.1.	Heat Flux and Radial Position Effect.....	64
3.2.2.	Mass Flux Effect	69
3.2.3.	Inlet Temperature Effect.....	71
3.2.4.	Comparison To Available Correlations	74

3.2.5.	New Correlations	76
3.3.	Conclusion.....	79
CHAPTER FOUR:	FLOW BOILING OF CARBON DIOXIDE IN A SINGLE JET	
IMPINGEMENT.....		81
4.1.	Introduction	81
4.2.	Results And Discussion.....	82
4.2.1.	Boiling Curve.....	83
4.2.2.	Heat Flux and Radial Position Effect.....	84
4.2.3.	Mass Flux Effect.....	87
4.2.4.	Pressure Effect	89
4.2.5.	Comparison To Available Correlations	91
4.2.6.	New Correlations	93
4.3.	Conclusion.....	97
CHAPTER FIVE:	SINGLE-PHASE CO ₂ IN MULTIPLE JET IMPINGEMENT	99
5.1.	Introduction	99
5.2.	Results And Discussion.....	99
5.2.1.	Heat Flux and Radial Position Effect.....	100
5.2.2.	Mass Flux Effect.....	102
5.2.3.	Inlet Temperature Effect.....	103

5.2.4. Comparison to Single Jet and New Correlation.....	105
5.3. Conclusion.....	106
CHAPTER SIX: FUTURE WORKS AND CONCLUSION	107
APPENDIX A: COPYRIGHT PERMISSION	109
APPENDIX B: COPYRIGHT PERMISSION	110
LIST OF REFERENCES	111

LIST OF FIGURES

Figure 1: Moore’s law.....	2
Figure 2: Advances in microfabrication, UNIVAC computer – from left to right; Apple MacBook Pro, Apple iPhone 13, Sony PlayStation 5	3
Figure 3:Hydrodynamics of single jet.....	8
Figure 4: Hydrodynamics of multi-jet [60].....	10
Figure 5: Cross flow effect [61].....	16
Figure 6: Periodic table showing the composition of Carbon dioxide.....	18
Figure 7: Thermophysical properties of Carbon dioxide	20
Figure 8: (a) Boiling curve (b) Schematic of flow boiling in jet impingement	22
Figure 9: Microfluidic device consideration.....	29
Figure 10: Photomasks’ patterns used for photolithography operation	30
Figure 11: Mask 4	32
Figure 12: Coarse alignment markers	33
Figure 13: Vertical and horizontal fine alignment patterns	34
Figure 14: Alignment methods (a) Horizontal and vertical placement of the fine alignment methods (b) Mask 3 and 4 placement using alignment markers	35
Figure 15: Wafer cleaning process (a) Wafer pre-cleaning (b) Hametch Hot Prihana tool	36
Figure 16: Final product of metal deposition on wafer (b) AJA sputtering tool	37
Figure 17: Highlighted photolithography steps	39
Figure 18: Etching (a) Wet etching with Aluminum etchant (b) Dry etching with AJA ion mill	40

Figure 19: SiO ₂ deposition (a) To electrically insulate the heater from the RTDs (b) To electrically protect and insulate the micro device from the environment.....	41
Figure 20: Final micro device images (a) CAD model showing layout (b) Real-life image with microscopic images of the device	43
Figure 21: Micro device package (a) CAD model showing the top piece and bottom piece (b) Real-life image of package after manufacture.....	45
Figure 22: CAD model of single jet configuration	46
Figure 23: CAD model of multi jet configuration	47
Figure 24: Sectional view of micro device package showing flow direction.....	48
Figure 25: Fluid direction state (a) pre-impingement (b) impingement (c) post-impingement....	48
Figure 26: Electrical connection (a) Designed PCB (b) Contact probe arrangement.....	49
Figure 27: (a) CAD model of final package assembly (b) Real-life image of package installation in the fluid line (c) Exploded view of device package.....	51
Figure 28: Schematic image of experimental loop	53
Figure 29: Temperature -resistance curve (a)RTD ₁ (b) RTD ₂ (c) RTD ₃	55
Figure 30: Heat loss estimation.....	60
Figure 31: Radial position and heat flux effect (a) Local surface temperature as a function of heat flux; (b) Local heat transfer coefficient as a function of radial position for a range of heat fluxes; (c) Local heat transfer coefficient as a function of heat flux. Conditions: $p = 7.45 \text{ MPa}$, $T_{in} = 21.1^\circ\text{C}$, $G = 0.53 \text{ kg/cm}^2\text{s}$ W/cm^2	65
Figure 32: Local heat transfer coefficient and surface temperature as a function of heat flux. (a) RTD1, (b) RTD2, (c)RTD3, (d) Average heat transfer coefficient and average surface temperature	

as a function of heat transfer rate. The dashed horizontal line in (d) represents the pseudocritical temperature 66

Figure 33: Specific heat effect on the heat transfer rate 69

Figure 34: Mass flux effect (a) Local surface temperature as a function of mass flux; (b) Local heat transfer coefficient as a function of mass flux; (c) Area-averaged heat transfer coefficient and surface temperature as a function of mass flux. Conditions: $p = 7.45 \text{ MPa}$, $T_{in} = 21.1^\circ\text{C}$, $q'' = 34.5 \text{ W/cm}^2$ 71

Figure 35: (a) Local surface temperature as a function of inlet temperature, (b) Local heat transfer coefficient as a function of inlet temperature (c) Local heat transfer coefficient and surface temperature as a function of inlet temperature at RTD1. All sub-figu 73

Figure 36: Comparison to available correlations 75

Figure 37: Area-averaged Nusselt vs dimensionless heat flux 77

Figure 38: Curve fitting (a) varying dimensionless heat flux (b) Varying Reynolds number 79

Figure 39: Boiling curves – (a) radial position effect ($T_{in} = 21.2^\circ\text{C}$, $T_{sat} = 21.5^\circ\text{C}$, $G = 1.0 \text{ kg/cm}^2\text{s}$); (b) mass flux effect ($T_{in} = 21.2^\circ\text{C}$, $T_{sat} = 21.5^\circ\text{C}$, $r_{avg} = 0.4$); (c) pressure effect ($G = 1.0 \text{ kg/cm}^2\text{s}$, $r_{avg} = 0.4$) 84

Figure 40: Effect of radial position and heat flux at $x_{in} = 0.002$. (a) local surface temperature distribution vs. heat flux. (b) local HTC vs. dimensionless radial position at selected heat fluxes. (c) local HTC vs. heat flux. (d) average local surface temperature 86

Figure 41: Mass flux effect on flow boiling of CO_2 . (a) local superheat temperature vs. mass flux (b) local HTC vs. mass flux (c) area-averaged HTC vs. mass flux and surface temperature. ($T_{in} =$

21.2 °C, $p_{\text{sat}} = 5.9 \text{ MPa}$, $q'' = 47.93 \text{ W/cm}^2\text{K}$ (d) Mass flux effect on HTC of flow boiling of CO ₂ at varying heat fluxes	89
Figure 42: Area-averaged HTC for three pressures as a function of averaged exit vapor quality. ($q'' = 7.4 \sim 100 \text{ W/cm}^2$, $G = 1.0 \text{ kg/cm}^2 \text{ s}$)	91
Figure 43: Comparison to available correlations	92
Figure 44: Correlation for nucleate boiling regime; (a) $q'' \propto \Delta T_{\text{sat}}$, (b) $h_{\text{avg}} \propto q''$ ($T_{\text{sat}} = 21.5 \text{ °C}$, $p_{\text{sat}} = 5.9 \text{ MPa}$, $G = 1.0 \text{ kg/cm}^2 \text{ s}$, $r_{\text{avg}} = 0.4$)	94
Figure 45: New CHF correlation vs experimental data	95
Figure 46: Comparison to single phase.....	97
Figure 47: (a) Local surface temperature as a function of heat flux; (b) Local heat transfer coefficient as a function of heat flux. ($p = 8.0 \text{ MPa}$, $T_{\text{in}} = 21.7 \text{ °C}$, $G = 1.1 \text{ kg/cm}^2\text{s}$, W/cm^2). (c) Average heat transfer coefficient and average surface temperature as a fun.....	101
Figure 48: Mass flux effect (a) local surface temperature with increasing mass flux (b) Area-averaged HTC and temperature distribution with increasing heat flux ($p = 8.0 \text{ MPa}$, $T_{\text{in}} = 21.7 \text{ °C}$, $q'' = 28.35 \text{ W/cm}^2$)	103
Figure 49: Pressure effect at varying heat flux	104
Figure 50: Comparison with single jet and proposal of new correlation (a) constant Reynolds Number (a) constant dimensionless heat flux	106

LIST OF TABLES

Table 1: Deposition rate for Titanium, Platinum and Aluminum.....	37
Table 2: Temperature-resistance correlation for each RTD	56
Table 3: Experimental Inlet conditions.....	63
Table 4: Available Nusselt correlations for jet impingement.....	75
Table 5: Experimental Inlet conditions.....	82
Table 7: Available CHF correlations	92

LIST OF ABBREVIATIONS

A = area

CHF = critical heat flux

cp = specific heat

d = diameter

G = mass flux

h = heat transfer coefficient

I = current

k = thermal conductivity

L = standoff (distance from the orifice exit to the heater surface)

\dot{m} = mass flow rate

Nu = Nusselt number

p = pressure

Pr = Prandtl number

P = power

q = heat transfer rate

q'' = heat flux

r = radial distribution of the temperature sensors

Re = Reynolds number

T = temperature

u = jet velocity

V = voltage

Subscripts

0 = initial

avg = average

e = estimated

f = liquid

g = vapor

H = heater

in = inlet

L = location

loss = loss

m = mean

max = maximum

out = outlet

pc = pseudocritical

r = local

s = surface

sat = saturation

Greek symbols

Δ = change

ζ = dimensionless heat flux

ρ = density

σ = surface tension

μ = dynamic viscosity

CHAPTER ONE: INTRODUCTION

1.1. Moore's Law and Advances in Microfabrication

We live in a world where human wants have substantially increased; from wanting electronic components such as cell phones, electronic wearables to operate faster to making them as small as possible. This wants have however been made feasibly possible as a result of the advances in microfabrication geared towards a combination of a continued miniaturization of integrated circuits and a growing improvement in their performances brought about by an ever growing transistor counts according to [1]. According to this law (Fig 1) “the number of transistors in a dense integrated circuit doubles about every two years”, to satisfy people’s expectations of ever greater performance and functionality of electronic devices. Microfabrication technology has been successfully utilized in the development of integrated micro-electromechanical systems (MEMS) [2, 3] and complex electronic components [4] for a wide range of operations with continuous innovation and reduction of the component’s physical size. A distinct example is that seen between the first commercial main frame computer UNIVAC designed by J. Presper Eckert and John Mauchly weighing about 16,000 pounds containing 700 transistors for primary logic and the popular Apple MacBook Pro weighing about 4.5 pounds with a processing unit containing about 16 billion transistors. This high energy electronic schemes promise substantial reduction in energy demand for emerging and growing computing needs. However, the diverging trend results in a substantial increase in heat flux and power density, posing challenges to the thermal management of these devices. [5-7] reported up a background heat flux of about 500 W/cm² and local hotspots heat flux of about 1000 W/cm² from high-speed microelectronic processors. Although the integration of microprocessors in now and future projects such as consumer electronics, robotics

to high-speed computing is promising in terms of their operating performances, major concern needs to be given to their thermal management to avoid thermal breakdown and lengthen their working lifecycle.

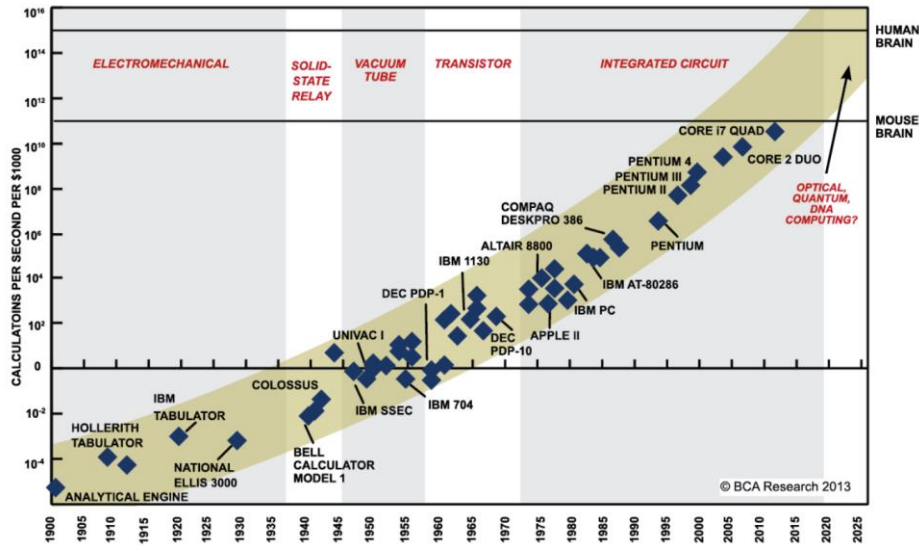


Figure 1: Moore's law

Several thermal solutions have been employed ranging from passive [8-11] to active cooling [12, 13] with active cooling being superior due to the enhanced convection. However, the consequences regarding the physical size of the device, power requirements from blower, pump, fans etc. and other external devices to control the flow of the fluid undermines the adoption of this cooling technology in certain thermal design. Passive cooling on the other hand has proven dominance in smaller devices such as consumer electronics – mobile phones, laptops etc. This includes extended surfaces such as fins, heat spreaders, thermal paste, heat pipes etc., with their performances controlled by an interplay between their thermal conductivity and length. However, with this innovation, high end devices still undergo thermal throttling such as lags, and shutdowns limiting their ability to achieve maximum performances. Micro scaled cooling has gained

considerable interest in recent times, due to their high heat transfer rate and compatibility with most miniaturized electronics. The adoption of this rose with the increased surface area to volume ratio with the scale reduction.

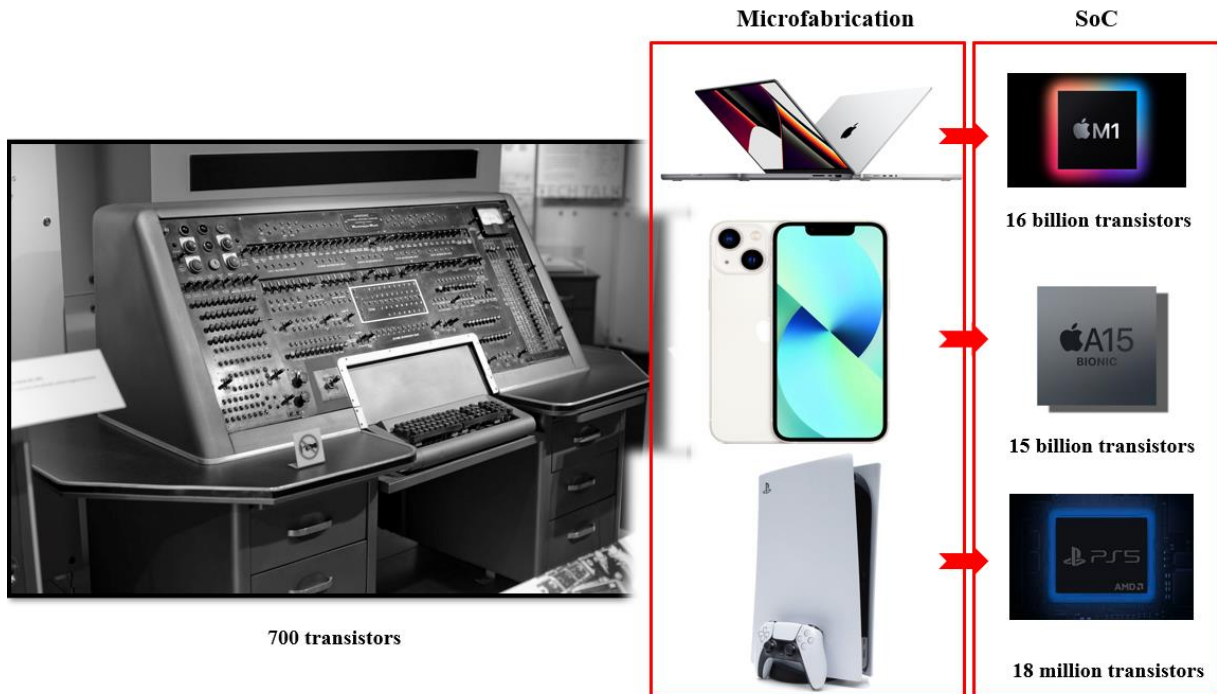


Figure 2: Advances in microfabrication, UNIVAC computer – from left to right; Apple MacBook Pro, Apple iPhone 13, Sony PlayStation 5

Micro scale cooling encompasses a range of reduced cooling scales such as microchannels [14, 15], micro jet impingement [16-18], micro pin fins [19-21] to mention a few. Microchannel has gained recognizable attention as a potential cooling solution for miniaturized electronics. Apart from their heat transfer ability, their integration in the chip design limiting the thermal contact resistance that would have been present if a heat sink was attached to the chip makes it a promising cooling method. However, the downside in its cooling ability is the inherently laminarity of the flow as the fluid flows through the small channels. Several heat transfer enhancement techniques

have been introduced and investigated to combat this downside such as micro pins [21, 22], micro pillars [23], micro impinging jets, concave and convex cavities for the sole purpose of distributing the flow. Micro jet impingement, an extension of micro scale cooling has dominated the micro cooling space as a result of its enhanced cooling ability brought about by its distinct hydrodynamic and thermal boundary layers. Generally, jet impingement cooling has been proven to be an efficient means of dissipating high heat fluxes from a heat generating surface or body [24-28]. They have been successfully employed in the field of heat and mass transfer because of their ease of control, effectiveness, and inexpensive running costs. Specific application can be seen in various industrial applications, such as metal treatment, internal combustion engines, gas turbines etc., offering very high heat transfer capabilities. In addition to its promising application, jet impingement can be used as a local heat removal as it can be locally directed to a hotspot generated within the device. Macro scaled jets (jets with larger exit nozzle diameters) have been extensively studied [25, 26] and more importantly the shift to embedding cooling in a miniaturized electronic circuit has necessitated the development of micro impinging domain, which has been proven by available limited studies to offer an overall better heat transfer capability when compared to the macro jets [29-31]. This enhancement has been attributed to a more distorted velocity boundary layer brought about by a decrease in the nozzle exit diameter. Anand et al [29], conducted a preliminary parametric analysis of micro jets to better understand its behavior and compare to macro jets. In this study, a semi-confined, single round axisymmetric submerged jet was modeled in Gambit and simulated in Fluent for varying nozzle diameter, while the mass flow was kept constant. Results showed a 37.3 % increase in heat transfer coefficient when the nozzle diameter was reduced from 0.5 mm to 0.25 mm. Glynn and Murray [32] also reported about 20 % to 70 % increase in

stagnation values when the jet diameter was reduced from 1.5 mm to 1 mm in the experimental setup.

1.2. Jet Impingement

This section details an overview of a promising thermal geometrical cooling solution termed “jet impingement”, its background and present-day knowledge of its heat transfer and flow characteristics in both its single and multi-jets configurations. First, the jet impingement technology together with its current industrial applications are introduced, followed by a detailed description of its hydrodynamics and the flow features of multiple jet arrays. Concludingly, the heat transfer dependencies such as the Reynolds number and other geometrical parameters is discussed

1.2.1. Background

Research interest in jet impingement began in the 1970’s and 1980’s, which were mostly published in Japanese journals [33-35]. Even though the proposed correlations for the heat transfer predictions have limited applicability as a result of the inadequate measurements method adopted, these studies provided some fundamental insights into the jet phenomenon in both single phase and various boiling regimes. Experimental [26, 36], numerical [37], and analytical [38] studies have been extensively conducted on macro impinging jets, widely supported by comprehensive review studies [39, 40]. However, with the growing demand for high end cooling capabilities and size reduction of integrated circuits, micro cooling domains have become a promising solution for thermal management. Not only is the size compatible with these miniaturized systems, but they also offer high heat transfer rate due to their high surface to volume ratio. Knowledge of the micro

cooling geometries have advanced through the years starting with revealing basic questions regarding continuum and incompressibility assumptions. Then channels were classified to macro, mini, micro and nano size according to their diameters. Both single-phase [40-42] and two-phase [43-45] flow heat transfer have been studied in an impingement cooling, which a range of fluids, such as water [46-48], R113 [49], transformer oil and ethylene glycol [50], HFE7000 [18], kerosene [51] etc. Likewise, some studies in chemical processes [52, 53] and cryogenic, that employed a throttling effect [54] require working with high pressured fluid. These studies confirm the feasibility of operating with high pressure within the micro domain; a condition that can be achieved with CO₂ near the critical point.

1.2.2. Jet Hydrodynamics

Jet impingement cooling is a heat removal technique in which fluid is directed to impinge on a target surface through a hole or a slot. The fluid issues out from the nozzle exit and strikes the surface it's been directed to, perpendicularly or at an angle. There are two different jet flow configurations namely, submerged, and free surface. In a submerged jet configuration, the working fluid entrains into a fluid surrounding that is almost the same as the jet itself. Martin [39] has extensively studied submerged jets. Free surface jet is characterized by fluid entraining into a fluid surrounding that is different from its state of matter. This flow configuration is developed immediately after the jet leaves the nozzle exit. Its jet shape is influenced by gravity, pressure forces and surface tension, however, gravitational effects are negligible in submerged jets. Both jets configurations have been studied and each proven its dominance in specific working conditions. Womac et al [55] investigated the effects of flow conditions with arrays of submerged

and free jets with FC-77 and water and concluded that submerged jets generally performed equally or more than free jets. Jets are also classified based on their boundaries, as confined and unconfined. Confined or semi-confined jet is characterized by fluid confined in a narrow channel bounded by the impingement surface and the surface containing the nozzle. Unconfined jets were previously studied, however the design compatibility of confined jets in various applications, has attracted more interest than its counterpart. Fluids undergo an amount of recirculation in confined jets due to bombardment of the impinged fluid with the top confinement.

In most cases, at the nozzle exit, the jet is turbulent as a result of high Reynolds number, it also develops a uniform velocity profile as a result of little or no interaction with the stagnant fluid [56]. As the fluid impinges on the target surface, a thin layer of hydrodynamic and thermal boundary is developed just beneath the jet, due to jet deceleration and resulting pressure increase, after which the flow is then forced to accelerate in a direction parallel to the target surface. Jet has been subdivided into three regions namely the free jet region, stagnation region and wall jet region due to the various distortions that occur between the periods the jet exits the nozzle and strikes the target surface. The free jet is then subdivided into the potential core, developing zone and fully developed zones. In the case of submerged jets, a potential core region is formed as the fluid exits the nozzle and proceeds towards the target surface. In this region (potential core) the jet centerline velocity is almost the same as the nozzle exit velocity, keeping the velocity profile uniform. This uniformity is as a result of little or no interaction with the stagnant fluid. The potential core – length the axial distance of the potential core, is governed by the nozzle geometry and jet velocity, according to Hollworth and Wilson [57], this distance extends over six to eight nozzle diameters

for well-formed nozzles, and over two to three nozzle diameters for square orifices for larger Reynolds number (>4000)

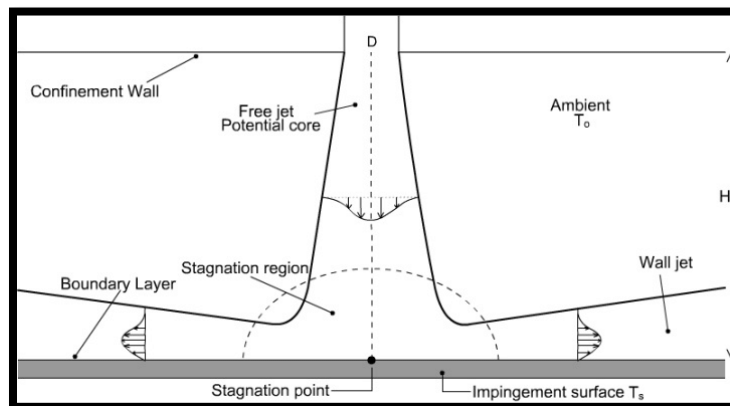


Figure 3: Hydrodynamics of single jet

Downstream the flow, the jet undergoes transfer of momentum from the ambient fluid and results in the expansion of the jet, losing energy, forming the developing and fully developed zones. Beyond the potential core is the stagnation region, where the jet velocity is then affected by the stagnant ambient fluid, reducing its velocity. This region is reported to be approximately 1.2 nozzle diameters from the surface, where the jet starts being influenced by the impingement surface, and the velocity profile is then affected due to the exchange of momentum to the ambient [25, 39, 58]. As a consequence, it builds up static pressure and moves in the radial direction towards the wall jet region. In the stagnation zone, the flow is decelerated, impinged, and accelerated in axial and radial directions in this order. The flow in the axial direction collides with the flow issuing from the nozzle exit and reduces its acceleration just before it strikes the target surface. This velocity fluctuations and high momentum are the cause of high heat transfer coefficient around the stagnation region. The final region is the wall jet region, where the fluid is being accelerated to

move radially outward, parallel to the target surface. Shear is created between this region and the ambient, which causes turbulence resulting in higher heat transfer rates in this zone.

1.2.3. Multiple Jets

Jet impingement cooling, could be made up of a single jet or an array of multiple jets, evenly or unevenly spaced depending on the desired flow structure. The emergence of multi-jets is to obtain a uniform temperature distribution over the heater surface. As reported from literatures [25, 39], the peak heat transfer coefficient is obtained at the stagnation zone and decreases radially some distances or diameters away from this zone. The idea of multi-jets is to cool much larger heated areas, while maintaining uniform heat transfer rate over the heat dissipating element. As aforementioned, the stagnation region is by far the most important region in the impinging jet, as this region exhibits enhanced heat transfer rates as a result of enhanced distortions due to the impingement effect and momentum exchange. In the view of this stagnation region's importance, there is need to generate as many stagnation regions as possible evenly spaced over a heat dissipating device ensuring a more consistent surface temperature distribution brought about by incorporating as many jets as possible. However, the flow structure of multiple jets is more complex as the jets are being affected by neighboring jets, cross flow are other features associated with a single jet, and if not properly designed, it could degrade the overall heat transfer rate. Multi-jets array come with a more different and complex hydrodynamics as there exists other interactions that come in play with the development of the boundary layer. Contrary to the single jets, there exists other geometrical parameters such as the interjet spacing (S/d) [59, 60], and crossflow [61] etc. that control the overall heat transfer process. The interplay between these parameters presents

a refined flow region in its hydrodynamics as depicted in Fig 4. There exist two important features in this flow distribution – the fountain upwash which is generated by the colliding jets and the entrainment of ambient air into several regions of the flow [59]. As depicted in Fig 4, the flow regions are classified into; free jet region, stagnation region, wall jet region, fountain formation region, fountain upwash region and the entrainment region.

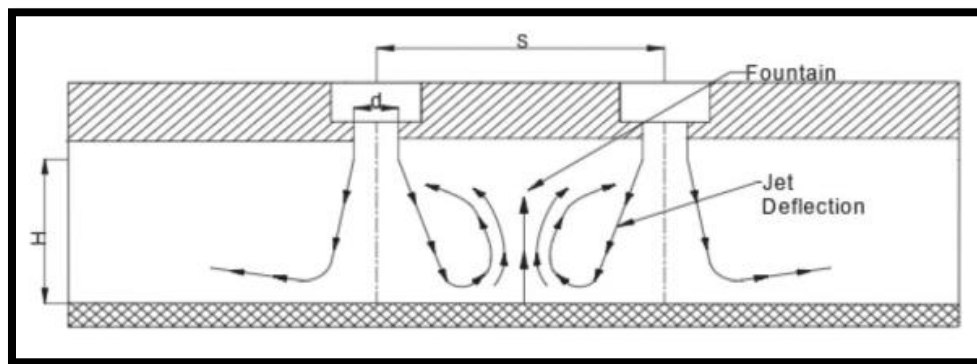


Figure 4: Hydrodynamics of multi-jet [60]

Compared to the single jet, the free, stagnation and wall jet region in the multi-jet flow region depict similar characteristics, while the fountain formation region located at the midpoint of the stagnation regions is as a result of the collision of the jets, moving perpendicularly to the surface and spreading spatially. Other parameters such as the heat flux, velocity magnitude and profile, turbulence intensity and wall temperature has been shown to influence the heat transfer rate [62] making the multiple jet impingement quite difficult to understand and correlate. The interjet spacing is one of the driving parameters that control the jets collision [60, 61]; for widely spaced jet, the rate of heat transfer is similar to that of the single jet as there exist little to no interaction between the jets, however for smaller interjet spacing, the heat transfer varies significantly solidifying the contribution of the jets collision to the overall heat transfer rate.

Another striking feature that influences the heat transfer process in a multiple jet impingement is the nozzles' spatial arrangement. Among the numerous possible arrangements, the inline, staggered, and hexagonal are the commonly most used and experimentally investigated. The main difference between these arrangements is the number of the neighboring jets of each nozzle as well as the impinged area per nozzle. Studies [63, 64] have shown that staggered jet arrangement leads to a more enhanced heat transfer rate as compared to its counterparts, however the choice of arrangement should be tailored towards the geometrical feature of the heat dissipating element.

1.2.4. Highlighted factors affecting the heat transfer of impinging jet(s)

Multiple variables control the heat transfer process of a jet including the Reynolds number (Re), Prandtl number (Pr), dimensionless standoff (L/d), interjet spacing (S/d), nozzle configurations, dimensionless radial position from the stagnation point (r/d), and system arrangement (e.g., confined jet, submerged jets, etc.).

Effect of Reynolds Number

A flow is classified as being laminar, turbulent, or transitional in nature. This flow classification postulated by Osborne Reynolds [65], has become a relevant method in analyzing and qualifying flow intensity. Laminar flow ($Re < 2300$) is characterized by a smooth flow moving slowly through a path due to its low velocities. Turbulent flow ($2300 < Re < 4000$) on the other hand is a more disturbed flow as a result of higher velocities. Transitional flow is a mixture of laminar and turbulent flow. Each of these flows behave in different manners in terms of their frictional

energy loss while flowing with different correlations to predict their behavior. General the Reynolds number takes the form;

$$Re = \frac{\rho u d}{\mu}$$

where ρ is the fluid density, u is the velocity, d is the channel diameter in which the fluid is being directed, and μ is the dynamic viscosity. The effect of Reynolds number on jet impingement has been investigated by numerous authors [25, 29, 39, 66] and has been demonstrated to be an important dimensionless parameter in predicting the behavior of the flow and its heat transfer characteristics alongside different working fluids. It's been reported that higher Reynolds number increases the heat transfer coefficient as a result of more generation of disturbance in the flow [29, 39]. The Reynolds number exponent in its Nusselt number dependency, has been reported by different authors, which varies depending on the nature of the flow (*laminar or turbulent*), its geometry and working fluid.

The average Nusselt number has been generally correlated according to:

$$Nu_{avg} = C Re^m Pr^n$$

where C , m , and n are coefficients. The value of an experimentally obtained coefficient m is calculated with a least-squares fit and has been reported for a range of Reynolds numbers. Garimella and Schrorder [67] reported an m value of 0.693 for confined air jet arrays with Reynolds numbers of 5000 to 20,000. Martin [39] reported an m value of 2/3 for a wider range of Reynolds numbers ($2000 < Re < 100,000$). Florschuetz et al. [68] reported a value of 0.73 and argued

that it is a function of geometric parameters. Kercher and Tabakoff [69] also found that m is a function of several geometric parameters and reported values ranging from 0.65 to 0.95. Robinson and Schnitzler [70] found m to be 0.46 for much lower Reynolds numbers than the previously mentioned experiments ($600 < Re < 6,500$). A value of $n = 0.42$ is widely adopted and has been confirmed by several authors [17]. Effect of transitional flows have been investigated. Zumbrunnen and Aziz [71] performed experiments to enhance convective heat transfer due to intermittency in an impingement jet. Results from this work suggests an inflection point at an approximate value of r/d of 1.9, for a submerged jet at L/d of 2 and Reynolds of 24,000. Gardon and Akfirat [58] also observed the similar trend at exactly the same location ($r/d = 1.9$) for submerged circular turbulent jets with Reynolds number greater than 25,000. Baughn and Shimizu [72] also reported these peaks in the heat transfer profiles. These peaks in the profile can be as a result of transition from laminar to turbulence flow in the channel. Transition to turbulence is by far a stochastic process, works have been done to predict the ranges at which it occurs and its effect on heat transfer profiles.

Ultimately, as demonstrated from literatures, an increase in Reynolds number significantly increases the area averaged Nusselt number, which in turns increases the heat transfer coefficients.

Standoff Effects (L/d)

The standoff effect popularly termed the nozzle-to-jet spacing, is the allowance or height designed between the nozzle exit and the target surface. As explained in Fig.3, various distortions occur between this distance, hence, the flow classification. Submerged jets have been proven to be more sensitive to this distance as compared to its counterpart free surface jet [55]. Another

important deciding factor is the length of the potential core, approximately 1.2 nozzle diameter. If the target surface is positioned within the potential core length, the heat transfer rate is only slightly affected at low Reynolds numbers, as a result of unaffected velocity profile at the potential core - significant effects are only seen at higher Reynolds numbers. By increasing the standoff, the heat transfer coefficient progressively increases to a peak and gradually diminishes, as a result of turbulence generated owing to the entrainment of the ambient fluid to the jet. This trend has been reported by many authors for a range of Reynolds number and working fluid. Anand [29] conducted a numerical study analyzing the standoff effects in micro jets. L/d values of 1, 3 and 6 were simulated at constant nozzle diameter and Reynolds number. The results showed a negligible standoff effect on the local heat transfer as there seem to be no significant difference in the profiles, especially after r/d of 0.5. The study also indicated a maximum Nusselt number at r/d of 0.5, which is somewhat counterintuitive to the maximum Nusselt number values achieved at the stagnation zone ($r/d = 0$). Pamadi and Belov [73] also suggested that this peak could be as a result of turbulence created due to non-uniform mixing in the developing jet that penetrates the boundary layer. Stevens and Webb [74] investigated the local heat transfer coefficient under an axisymmetric single-phase liquid jet and suggested a Nusselt number correlation of $Nu \sim (L/d)^{-0.032}$ for a Reynolds between 9600 to 10,500 and standoff from 1.7 to 3.4. The exponent value indicates almost a negligible standoff effect on the Nusselt number. At lower standoffs, the jet becomes very sensitive due to the acceleration and local thinning of the boundary layer, whereas the Nusselt number has been observed to diminish with an increase in this spacing. Studies have been done to understand and correlate the Nusselt number dependency on the lower standoff. Lyte and Webb [75] studied the local heat transfer for submerged impinging jets at standoffs less than one nozzle

diameter ($L/d = 0.1$ to 1.0) at fixed Reynolds. They suggested a power law relationship $Nu \sim (L/d)^{-0.191}$, which indicates an increase in the local Nusselt number as the standoff decreases. Choo et al [76] performed similar experiments in lower standoffs less than one nozzle diameter ($L/d = 0.125$ to 1.0) and reported negligible standoff effects on the Nusselt number under a fixed pumping power. Recently, the standoffs have also been correlated with the hydraulic jump diameters. Stevens and Webb [74] suggested a correlation for the hydraulic jump diameter as a function of the Reynolds number only, without taking into account the standoffs. Brechet and Neda [77] investigated both the theoretical and experimental of circular hydraulic jump and suggested a theoretical correlation for the hydraulic jump radius as a function of the standoff. Kuraan et al [78] recently investigated the heat transfer and hydrodynamics of free water jet impingement at low standoffs ($L/d = 0.08$ to 1.0). In this study, the normalized stagnation Nusselt number and hydraulic jump diameter were divided into two regions: Jet deflection region ($L/d \leq 0.4$) and Inertia dominant region ($0.4 < L/d \leq 1$). The results obtained, suggest that the in the jet deflection region, the Nusselt number and hydraulic jump diameter decrease drastically with decreasing standoffs. This result was correlated as $Nu \sim (L/d)^{-0.6}$ and $H_d \sim (L/d)^{-0.4}$, where H_d is the hydraulic jump diameter. The standoff effect is negligible on the Nusselt number and hydraulic jump diameter due to the constant average velocity of the jet.

Radial distribution to nozzle diameter (r/d)

The radial distribution to nozzle diameter (r/d) is the ratio of the radial measurement of the heater to the nozzle diameter. This is further used in classifying jet into its region (stagnation and wall jet region). With an r/d of 0, the area under the jet is said to be at the stagnation region where

the impingement effect is highly pronounced before it diminishes towards the wall jet region. Studies [29, 39] have shown maximum heat transfer rate observed at this region which decreases radially as the r/d increases. Likewise, some studies have reported a local maxima at r/d values of 0.5 attributed to transition to turbulence within the impingement domain. In most literatures, r/d markers are implemented by placing temperature sensors at various radial distances on the heater.

Cross flow

The effect of the cross flow is observed in multiple jet array as has been proven to govern the heat transfer behavior. Obot and Trabold [61] investigated the crossflow effect subdividing them into three schemes namely, the minimum, intermediate and maximum crossflows as shown in Fig 5. The crossflow effect is mainly attributed to the passage of the spent fluid after impingement. It has been reported that the crossflows undermine the heat transfer rate by delaying impingement when the downstream jets are swept away by the upstream jets. The same study has found out that the magnitude of the crossflow effect is enhanced by increasing the standoff.

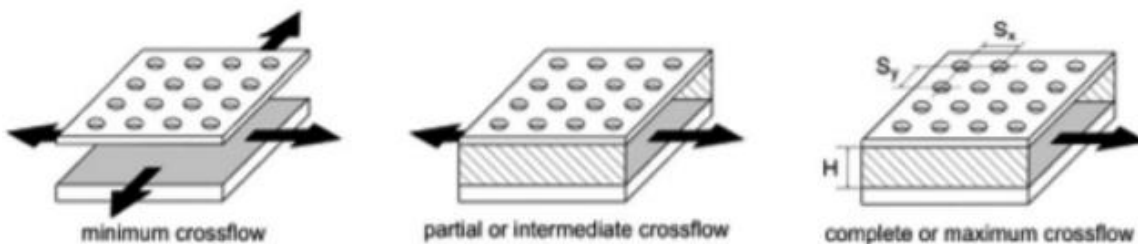


Figure 5: Cross flow effect [61]

Jet Inclination

In some cases, the position of the nozzle exit could be oriented non-perpendicular relative to the target surface. This configuration affects the hydrodynamics of the flow which therein

affects its heat transfer characteristics. Stevens and Webb [74] reported an empirical correlation for local Nusselt number along the major and minor axes for free-surface jets at higher Reynolds number as

$$Nu = ARe_d^a \exp \left[(p\theta^2 + m\theta + n)(r/d) \right]$$

Where, θ is the inclination angle of the jet relative to the target surface expressed in radians. [] also reported a correlation for axisymmetric oblique jets in both submerged and free surface configuration for Reynolds number less than 1000 as;

$$r/d = (M + N\theta)\cos\theta$$

where M takes the value of 0.119 and 0.0176 for free-surface and submerged jets respectively. N also reported as 0.00454 for free-surface jets and 0.00754 for submerged jets.

1.3. Carbon Dioxide

The first use of CO₂ as a refrigerant can be traced to the mid-nineteenth century [79] which were later displaced by chlorofluorocarbons (CHF_s) after the World War II. The adoption of CO₂ as a viable thermal fluid is already growing. Hence, its applications in hydrocarbon storage, cold-rooms, industry supermarkets, residential air conditioning etc. CO₂ effectively operates at elevated pressures; the choice of operating regime can be appreciated from its P-T phase diagram.

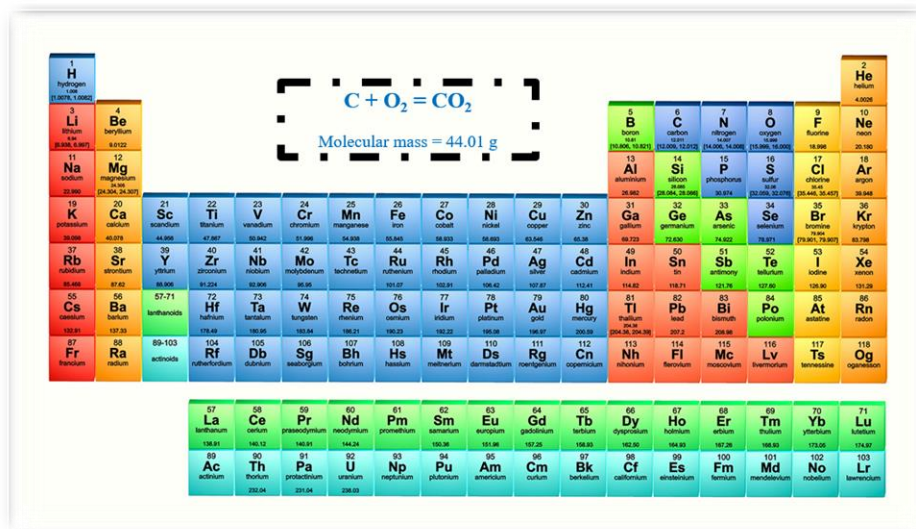


Figure 6: Periodic table showing the composition of Carbon dioxide

CO₂ in its supercritical state is a promising fluid for a wide range of applications. In fact, the higher operating pressure does offer certain advantages such as a high fluid density throughout the cycle as a result of the elevated pressure which permits the miniaturization of cooling systems for use in mobile applications, such as in cars and trucks. The use of super critical CO₂ in power cycles has been investigated and explored for decades while undergoing constant reinvention. Since the high density and the volumetric capacity of super critical CO₂ make it more energy dense when compared to other working fluids, the size of most of the system components within the power cycles can be considerably reduced leading to a smaller plant footprint and lower capital costs.

Recent applications of super critical CO₂ can be seen in the areas of petroleum refining and petrochemistry [80], food processing [81, 82], separation processes [83], etc. which summarizes the advantages of carbon dioxide as a solvent. A more recent application of super critical CO₂ has been explored in solar collectors [84], or in carbon capture and storage [85, 86]. In addition to the aforementioned properties, CO₂ possess liquid-like density and gas-like viscosity in its super

critical state, therefore, when combined with other thermal properties and cooling geometries, one can achieve larger transfer of heat with relatively small pressure drops within a micro domain. As such, it is a good candidate for working fluid in compact systems like printed heat exchangers and micro domains

1.3.1. Supercritical Carbon Dioxide (sCO₂)

1.3.1.1. Thermophysical Properties of sCO₂

As shown in Fig 7, the thermophysical properties of CO₂ vary dramatically with the temperature and pressure in super critical state [87-89]. For a specified pressure, properties such as the dynamic viscosity, thermal conductivity and the density are significantly diminished with an increase in the fluid's temperature. The specific heat capacity assumes a maximum value at the critical point and pseudocritical temperature which further declines as the pressure increases similar to that of the phase change processes of mixtures utilized in thermal energy storage [90]. Although the drastic drop in the density limits the potential use of super critical CO₂ as a storage media, the thermophysical variations of the fluid at this state makes its heat transfer characteristics and performance different from available conventional fluids. The heat transfer performance of super critical CO₂ can be classified into three heat-transfer regimes: normal, improved and deteriorated. The deteriorated regime is accompanied by higher heat fluxes and lower mass fluxes which can be greatly reduced by increasing the turbulence level of the flowing fluid. In a nutshell, the variations observed in the heat transfer performance are as a result of the dramatic changes in

the thermophysical properties in the radial direction leading to both pseudo-boiling and pseudo-film boiling phenomena.

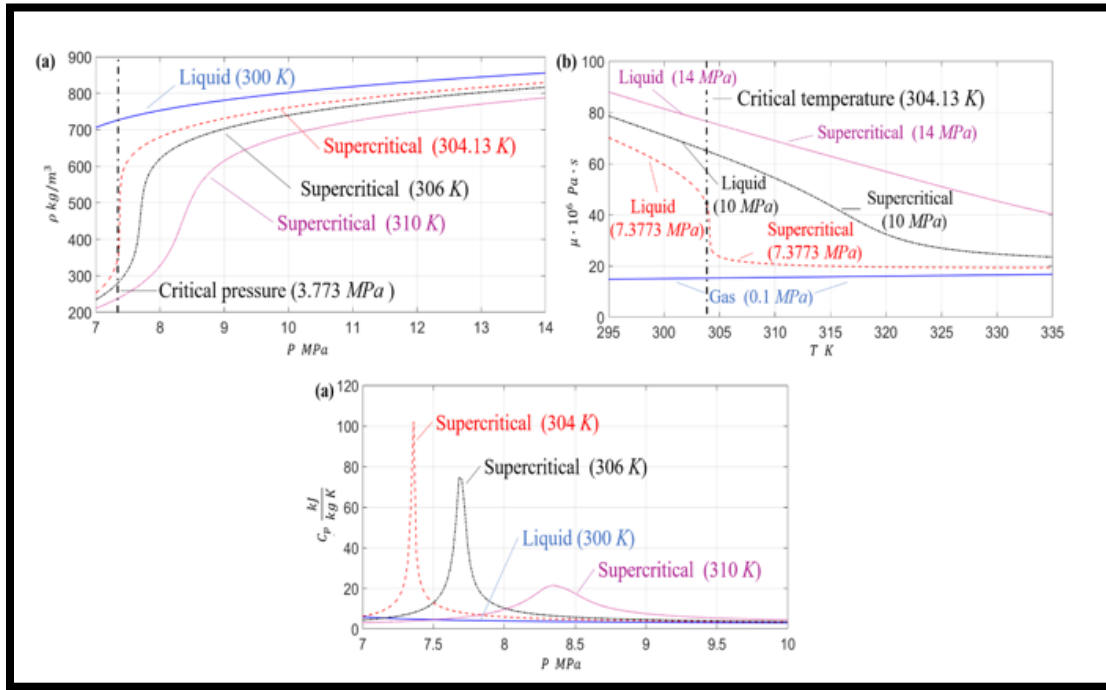


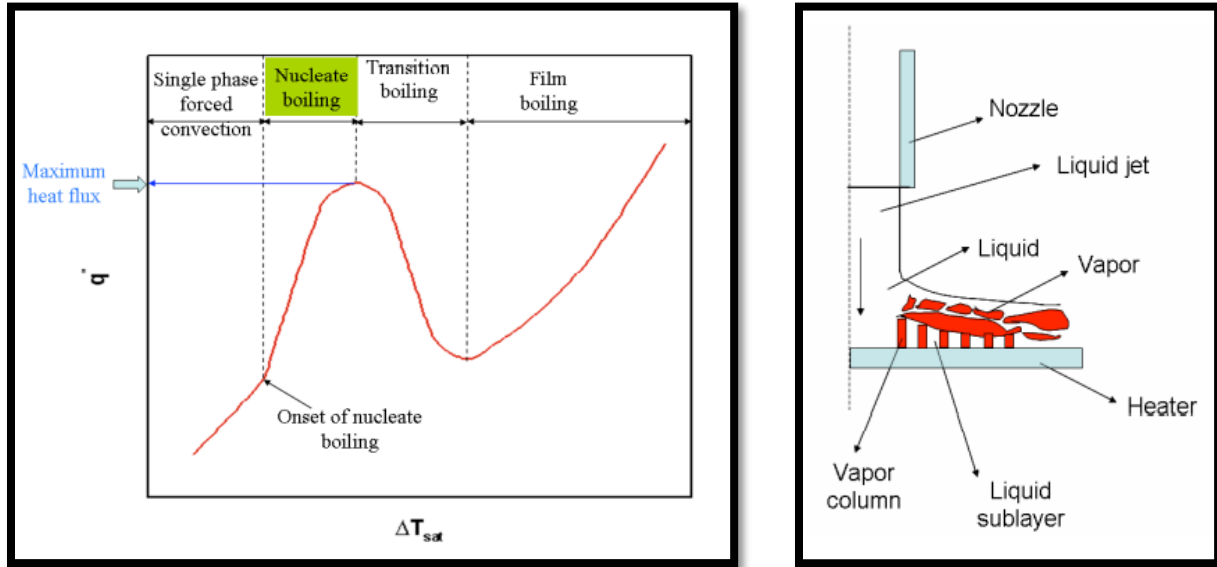
Figure 7: Thermophysical properties of Carbon dioxide

1.4. Flow Boiling

Flow boiling, a process that leverages liquid to vapor phase change to enhance heat transfer has been extensively studied in horizontal channels [91] and also in jet impingement [45, 48, 92-94]. This process offers very high heat transfer coefficient making them attractive for electronic cooling applications. In most cases the nucleate boiling regime as seen in Fig 8(a). is the most attractive as this region is characterized by a small increase in the wall superheat with a large increase in the heat flux. Flow boiling is a very complex phenomenon with quite a number of varying parameters interplaying to dictate the overall heat transfer ability. Focusing on this

fundamental and with the higher heat transfer coefficients associated with the nucleate boiling regime, its combination with micro jet impingement could significantly enhance the heat transfer performance while being suitable for electronic cooling. Although this combination could result in a more complex phenomenon as both the flow boiling process and jet impingement possess strong interplay of various parameters, meticulous study of important parameters and their contribution to the heat transfer performance can be analyzed. Typically, the increase in the heat transfer coefficient in the nucleate boiling regime is governed by the intense development of bubble motion and mixing [45, 95]. Studies have revealed the importance of various effects on jet impinging flow boiling. For instance, Wolf et al. [45] observed that the jet diameter, jet orientation and number of jets for multiple jet configurations and other jet configurations did not have a significant effect on heat transfer in nucleate flow boiling. On the other hand, Qui and Lui [96] suggested that the conditions of the heat transfer surface are an important variable. Studies also examined the critical heat flux (CHF) conditions [97-99], and a number of CHF correlations were proposed taking into account a range of parameters, such as the jet velocity, vapor and liquid densities, and heater size. This CHF condition is characterized by a drastic increase in the wall surface temperature as a result of the dry out conditions as a result of little to no fluid contact with the heated surface to sustain boiling. As depicted in Fig. 8(b), the liquid sublayer extracted from the liquid jet issuing from the nozzle sustains boiling until a condition where the issuing jet cannot

be supplied to this sublayer leading to a dry out, indicating a CHF condition.



(a)

(b)

Figure 8: (a) Boiling curve (b) Schematic of flow boiling in jet impingement

1.5. Objectives

By scrutinizing the results of the research in the literature, it was observed that the enhancement of heat transfer rate can be attained by shrinking the nozzle exit diameter from the macro to a micro scale. Likewise, the varying thermophysical properties of carbon dioxide in its super critical state and its flow boiling properties can lead to higher heat transfer coefficient, removing heat from miniaturized electronic devices that dissipate very high heat fluxes as a result of the implementation of increasing processors and transistors in its integrated circuit for a better and faster operating system. Therefore, by combining the advantageous properties of the micro jet domain with carbon dioxide in its single-phase or two-phase condition, a more effective and

efficient cooling method can be achieved for these ever-growing integrated circuits. Since limited studies have been dedicated to this study, this thesis aims to tackle the following scheme.

- Evaluate the feasibility, applicability and effectiveness of micro impinging jets and high-pressured fluid in a micro domain
- Precisely obtain the spatial and temporal temperature measurements in the micro domain to infer the local and area-averaged heat transfer coefficient, inception of nucleate boiling and critical heat flux
- Investigate the optimum cooling process/flow by varying important parameters such as the heat flux, mass flux, temperatures, and pressures.
- Investigate the convective heat transfer characteristics at the pseudocritical region for the single-phase flow and nucleate boiling regime for the two-phase flow.
- Evaluate CO₂ as a potential coolant, compare its heat transfer properties with available correlations and develop new correlations if required

1.6. Dissertation Overview

As mentioned above, jet impingement is very complex phenomenon more importantly in the micro scale, and a well detailed understanding of the physical phenomenon is crucial for a flow and heat transfer characterization alongside the working fluid. With key attention on CO₂ as the working fluid in both single-phase and two-phase conditions, meticulous experimental investigation is needed to qualify and quantify its behavior with micro jet impingement to fully understand its flow and heat transfer properties as well as its susceptible governing factors for next generation cooling. Therefore, using precise spatial and temporal temperature measurements, more

insights into the complex thermo-hydrodynamic phenomenon is to be obtained. In addition, the work includes the development of new correlations, mathematical equations to further improve the accuracy of available heat transfer predictions.

This thesis is organized below:

Chapter 1: The introductory chapter begins with the advances in micro fabrication that brought about conflicting trend between the thermal management of these electronic devices and customer desire, the available thermal remedy as well as their issues and challenges. The chapter further describes the innovation in jet impingement cooling, the shift to micro scale cooling and the utilization of CO₂ as a promising thermal fluid to alleviate concerning industrial thermal problems as well as setup a future cooling framework to meet up with ever-growing transistor counts in dense integrated circuits. Finally, the scope and objectives are described. This chapter also introduces historical review of jet impingement and CO₂ in both single-phase and two-phase conditions, along with the physical fundamentals and hydrodynamics of jet impingement together with available correlations to predict the heat transfer behavior.

Chapter 2: This chapter constitutes the experimental apparatus and set up utilized in this investigation. Here the steps employed in the development of the test specimen (micro fluidic device), its housing and the experimental setup are well detailed

Chapter 3: This chapter introduces the experimental investigation of super critical CO₂ in a single impinging jet. The observed heat transfer behavior as well as the optimum working condition is reported. Quantitative assessment of the heat transfer enhancement due to the

susceptible heat-transfer governance such as the radial position, heat flux, mass flux and inlet temperature is well documented in this section. Finally, a new correlation for future research and industrial use is reported.

Chapter 4: Further hypothesized enhancement in single jet impingement with flow boiling of CO₂ is explained in this chapter. The flow and heat transfer behavior are reported together with a comparison between super critical and subcritical pressures. Quantitative assessment of the of the heat transfer enhancement due to the susceptible heat-transfer governance such as the radial position, heat flux, mass flux and pressure is well documented together with a new critical heat flux correlation for future and industrial research.

Chapter 5: This chapter further introduces the heat transfer and flow behavior utilizing an array of micro jet together with CO₂ in its super critical state. The comparison between the single and multiple jet(s) is also well documented.

Chapter 6: Concluding remarks from this study are reported in this chapter

CHAPTER TWO: METHODOLOGY

The contents of this chapter have been published in:

Adeoye, S., A. Parahovnik, and Y. Peles, A micro impinging jet with supercritical carbon dioxide. International Journal of Heat and Mass Transfer, 2021. 170: p. 121028. [100]

Adeoye, S. and Y. Peles, Flow boiling of carbon dioxide with a micro impinging jet. International Journal of Heat and Mass Transfer, 2022. 187: p. 122495. [101]

This section explicitly described an overview of the experimental apparatus, their design, and mechanical considerations to meet up the proposed system.

The experimental apparatus consisted of four main systems;

- a) The microfluidic device to provide heating and temperature change measurement as a consequence of the jet's cooling ability
- b) Device housing to support the micro fluidic device mechanically and electrically
- c) Experimental loop to channel the fluid onto/from the micro fluidic device at specific operating conditions.
- d) Data acquisition and processing units to simultaneously collect, record and digitally process data for analysis.

2.1. Microfluidic Device

As highlighted above, a micro scaled test device with operations similar to traditional circuit layout was utilized as the main device to be cooled. This device consisted of a heater and three resistance temperature detectors (RTDs) mechanically supported on a $30.5 \times 1.9 \text{ mm}^2$ fused silica substrate to respectively supply heat and measure the local surface temperatures. The requirements for the substrate were the need to have a low thermal conductivity, reducing the heat lost by conduction, and for it to withstand the required operational pressure of up to 10 MPa. Silicon is the most suitable and common material for variety of micro fabrication processes; however, Silicon possesses a high thermal conductivity restricting the usage in this research. Other materials such as sapphire, borosilicate glass and fused silica present alternative approach for micro fabrication process due to their low thermal conductivity and mechanical strength. However, due to the scarcity and cost of purchase, fused silica remained the most prospective candidate to be used as the structural material for the microfluidic device.

2.1.1. Heat generation and temperature measurement

The heater comprised of a serpentine-shaped wire made of Titanium and Platinum with the former used to promote adhesion to the substrate, wound around in a circular form - This configuration was as a result of the targeted heater resistance of ~ 50 ohms confined in a 2 mm micro space, and a need for a circular heater to ensure a more uniform temperature distribution according to

$$R = \frac{\rho L}{A_c}$$

where ρ is the resistivity as a function of the temperature, L is the length and A_c is the cross-sectional area of the wire. Right at the center of the heater, three RTDs were radially sputtered in a concentric manner to measure the radial temperature distribution on the surface of the heater during the experiment. The targeted resistances for the RTDs were 150 ~ 300 ohms, with compensations made to the width, length, and shape of the RTDs for uniform resistance measurement at constant temperatures.

2.1.2. Device design and layout

Three designs were attempted – 1st to 3rd generations, with selection criteria based on the cost of production, complexity, material consumption, no of RTDs and the stress concentration. The 1st generation device consisted of highest number of RTDs supported on thick substrate. When analyzed for stress concentration and higher number of temperature sensors, the 1st generation design would have been more appropriate, however, subject to the cost of production and complexity, the 3rd generation device offered the most suitable design with three RTDs, a thinner and a cost-effective substrate.

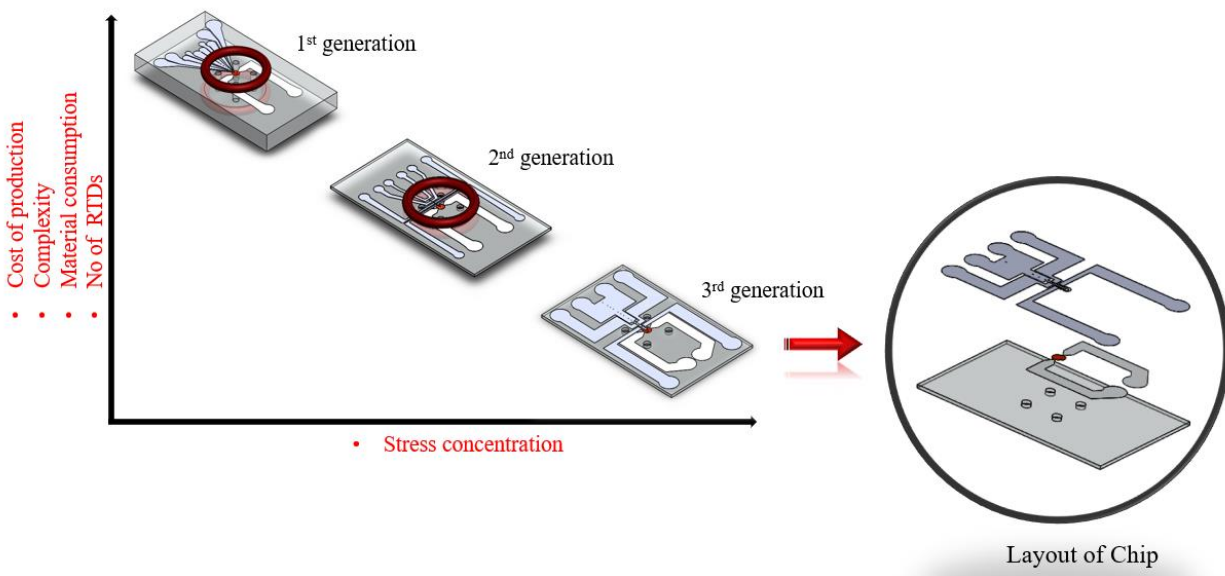


Figure 9: Microfluidic device consideration

2.1.3. Mask Layout and Configuration

Photomask is an opaque plate with holes or transparencies that allow light to shine through in a defined pattern. These masks are commonly used in photolithography operation. The masks are placed in direct contact with the photoresist coated surface and the wafer is exposed to ultraviolet radiation. The absorber pattern on the mask is opaque to UV light, whereas glass or quartz is transparent. This allows a 1:1 image of the masks to be transferred to the wafer where necessary etching operations are followed. For this microfabrication process, six photomasks as seen in Fig 10, were designed for each specific photolithography operation in order to pattern the heater, RTDs, their leads and the dicing grids.

The microfluidic device was compromised of two layers; the heater (lower layer) and RTDs (upper layer). These layers were separated by a layer of Sodium dioxide (SiO_2) (1.1 μm thick) to electrically insulate the heater from the RTDs. Two masks were used in the design of the heater

and its leads, another set of two masks were used for the design of the RTDs and their leads and the last two masks were used in exposing the heater and RTDs' leads for electrical connection. Each mask consisted of two alignment patterns (coarse and fine) used to align the masks during photolithograph process. These alignment patterns were used to ensure the masks were placed on the wafer evenly to disallow any form of deviation on the device.

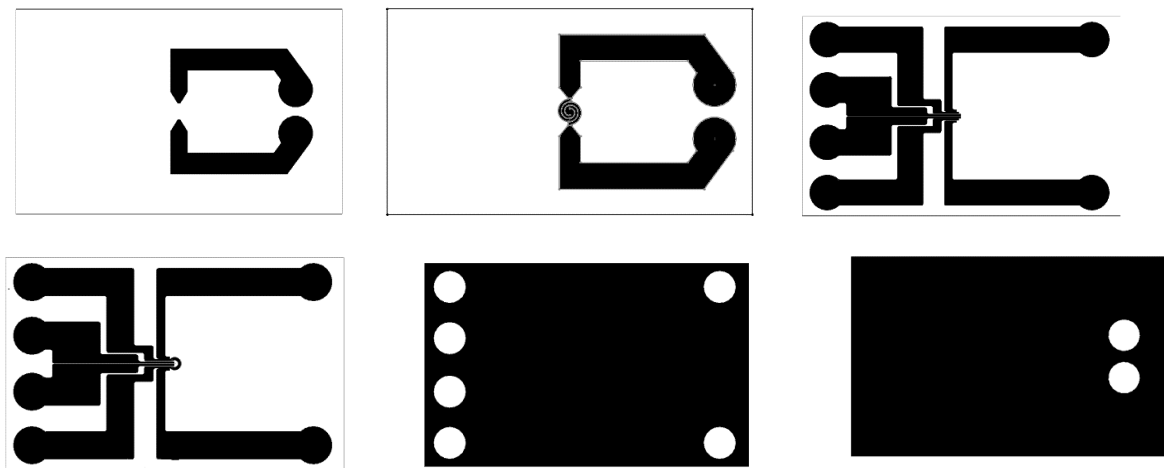


Figure 10: Photomasks' patterns used for photolithography operation

The configuration and the purpose of each photomask is summarized below;

Mask 1 (Heater leads)

The first step in photolithography was to etch the heater vias. This was done after which Aluminum, Platinum and Titanium have been sputtered on the wafer. The purpose of the leads was to supply heat the heater though affixed contact probes.

Mask 2 (Heater)

After the vias have been etched, the heater was shaped using this mask. The mask consisted of a pattern wound around in a circular manner to compensate for the small diameter (1.5 mm) of the heater.

Mask 3 (RTD leads)

The third mask shaped the RTD leads. This mask consisted of patterns of varying dimensions extending to both sides of the wafer (left and right). It also consisted of the dice borders, used in dicing the wafer after the micro fabrication steps had been completed.

Mask 4 (RTD)

The RTD mask shaped the RTDs as desired shown in Fig 11. The design consisted of three RTDs sputtered on top of the heater in a concentric manner. These RTDs were of varying radii to measure the average radial temperature distribution. RTD1 had the smallest diameter, in this case the pattern was wound around a 100 μm diameter template. The width measured 3 μm and had an approximate length of 0.8 mm. RTDs 2 and 3 had similar pattern but with different radius and width, they measured 600 μm , 1200 μm radii, and 5.5 μm , 11 μm width respectively.

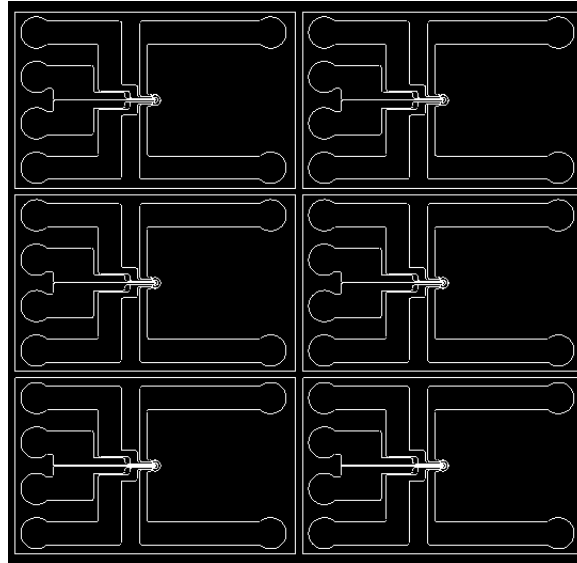


Figure 11: Mask 4

Mask 5 (RTD Contact Pads)

This mask exposed the contact pads of the RTDs. A layer of SiO_2 was deposited after the RTDs have been etched to prepare the device for CMP polishing. Due to this reason, there is need to etch that layer of SiO_2 in order to allow for electrical contact. The contact pads were in form of a circle measuring 3 mm in diameter.

Mask 6 (Heater Contact Pads)

Finally, the contact pads for the heater leads were needed to be exposed for the same reason as the RTD leads. These were also in form of circles measuring 3 mm in diameter similar to that of the RTDs.

Mask Alignment

Since all dimensions were in micro scale, the slightest deviation ($<1 \mu\text{m}$) could be detrimental to the microfabrication of the device. Thus, there is need to place each mask evenly and carefully on the wafer to ensure they were accurately positioned. Two types of alignments were used for this cause: coarse and fine alignments.

Coarse alignment

These alignment markers were located at each side of the mask; the resolution of these features were $10\text{-}50 \mu\text{m}$ as shown in the Fig 12. These markers were present in all the photomasks and were used as a coarse positioning indicator during the photolithography process.

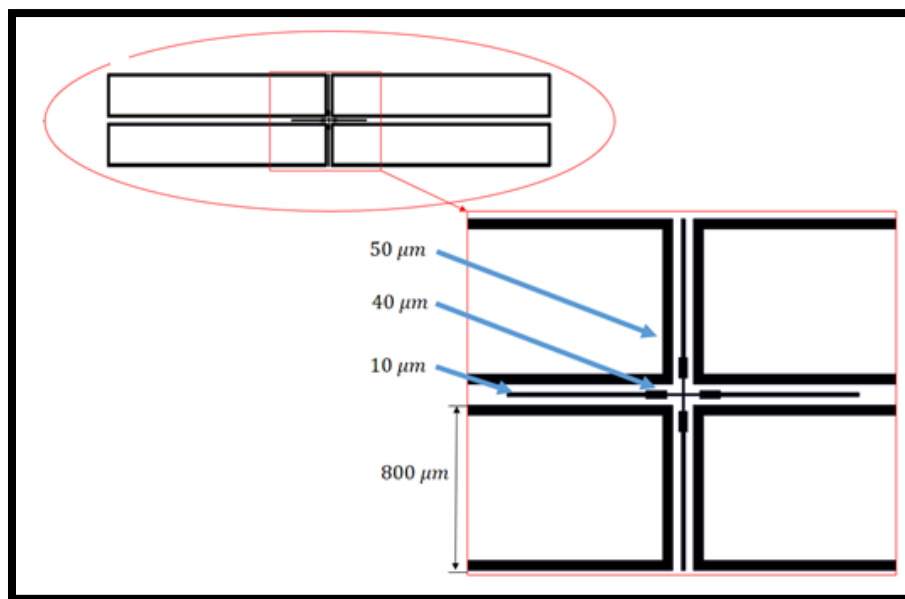


Figure 12: Coarse alignment markers

Fine alignment

These markers were located beside the coarse alignment patterns. They consisted of a vertical and horizontal comb like pattern which aligned the mask in both horizontal and vertical positions. The purpose of this was to ensure each comb fingers aligned horizontally and vertically with the previous mask with minimum deviation. Mask 1 relied only on the coarse alignment method as it was the first mask being used, generating the fine alignment patterns, in which other masks used as a point of reference.

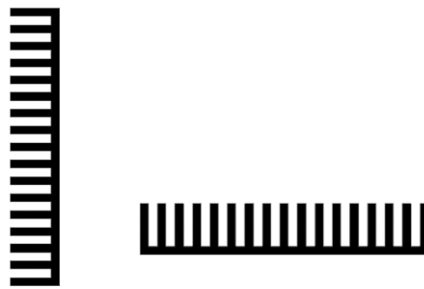
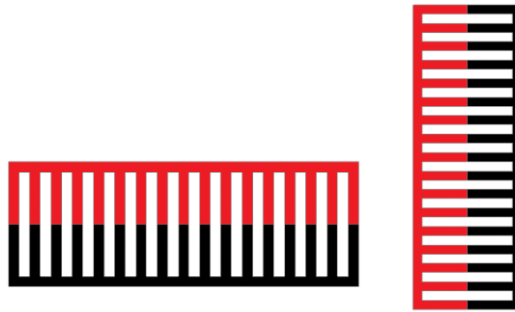
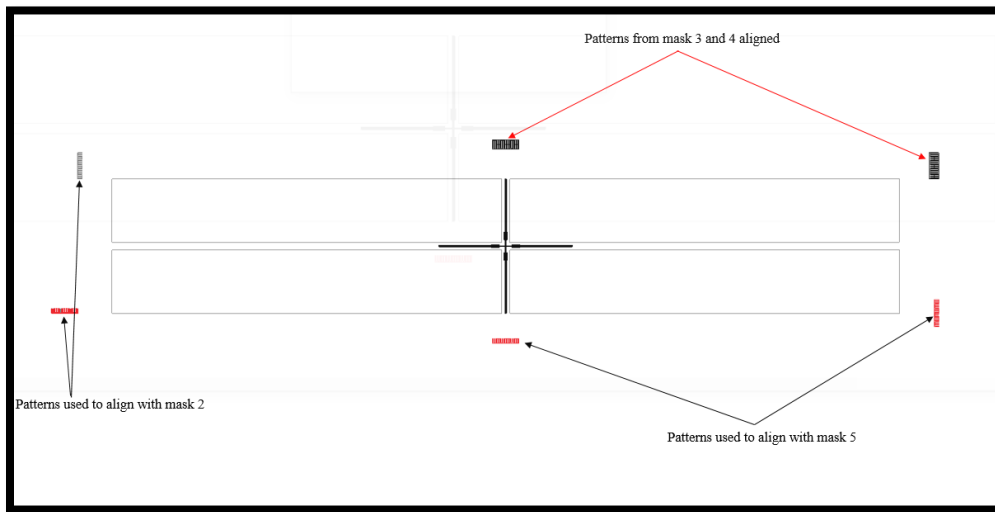


Figure 13: Vertical and horizontal fine alignment patterns

An illustration of the fine alignment method between masks 3 and 4 is shown below. The fingers of mask 3 (red) aligned with the fingers of mask 4 (black), vertically and horizontally. Each mask created a fine alignment pattern for the next mask to be used, to ensure even placement of the mask on the wafer. As seen in the figure 14, mask 3 contained the fine alignment patterns used to align with mask 2, likewise the patterns used to align with mask 4. The same goes for mask 4, which contained the patterns needed to align with mask 3 and 5.



(a)



(b)

Figure 14: Alignment methods (a) Horizontal and vertical placement of the fine alignment methods (b) Mask 3 and 4 placement using alignment markers

2.1.4. Microfabrication

This section details the microfabrication process employed to achieve the test device. The was micro fabricated leveraging a combination of conventional manufacturing tools and standard microelectromechanical systems techniques.

The microfabrication process is explicitly discussed below with the tools and operations highlighted in each section,

Wafer cleaning

The microfabrication commenced with wafer cleaning process to remove contaminants on the substrate. This process employed the Hametch Hot Prihana tool with a wafer clean short operation for about 10 minutes. The tool consisted of a chuck that firmly held the wafer in place during loading, cleaning and unloading operations.



(a)



(b)

Figure 15: Wafer cleaning process (a) Wafer pre-cleaning (b) Hametch Hot Prihana tool

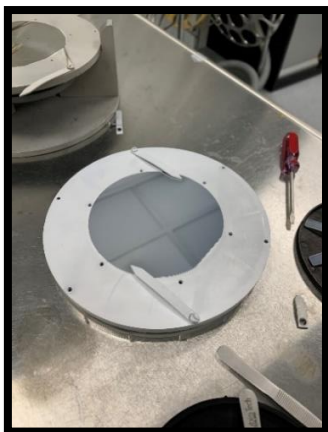
Thin film Deposition

After the cleaning process, the wafers were set for the thin film deposition (metal deposition) to orderly sputter layers of 7 nm thick Titanium, 100 nm thick Platinum and 1 μm thick Aluminum. To do this, the AJA sputtering machine was utilized, with two variable parameters:

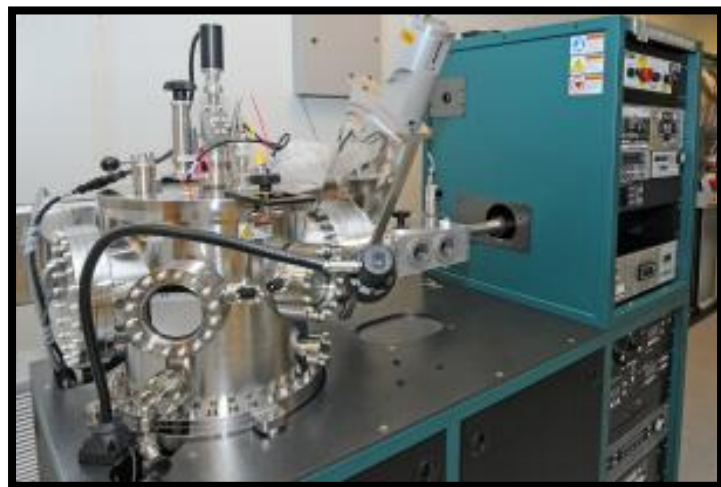
the pressure (mTorr) and duration (sec) – Table 1. These parameters were used to control the targeted thickness of each metal as a result of different deposition rate due to the metal’s chemical and physical compositions.

Table 1: Deposition rate for Titanium, Platinum and Aluminum

Metal & Rate	Pressure (mTorr)	Time (sec)
Titanium (1.67A/sec)	3	4975
Platinum (4.69A/sec)	3	42
Aluminum (2.01A/sec)	3	213



(a)



(b)

Figure 16: Final product of metal deposition on wafer (b) AJA sputtering tool

Photolithography

Following the metal deposition, a photolithography process was employed which comprised of the following steps

- a) vapor priming: a process to promote adhesion of the photoresist to the metal by dehydrating the wafer with HMDS vapor.
- b) photoresist coating: in which a S18181 photoresist was spun at a speed of 3000 rpm for 45 seconds over the wafer to protect important patterns after etching.
- c) soft baking to adhere the photoresist more to the wafer, by placing the wafer on an oven for 90 seconds at 115 °C.
- d) photoresist bead removing process to scrap out the excess buildup of photoresist at the edges of the wafer after spinning.
- e) exposing the wafers to UV light using a MA6 contact aligner and specified mask at gap of 30 μm for 4.5 seconds.
- f) post-baking to bring the reactions to a halt by heating it up at a temperature of 115 °C for 90 seconds.
- g) wet development process (spray-on) to transform the latent resist image formed during exposure into a relief image.
- h) hard baking at 115 °C for 90 seconds to remove residual developing solvents and to ensure finer patterns on the wafer.

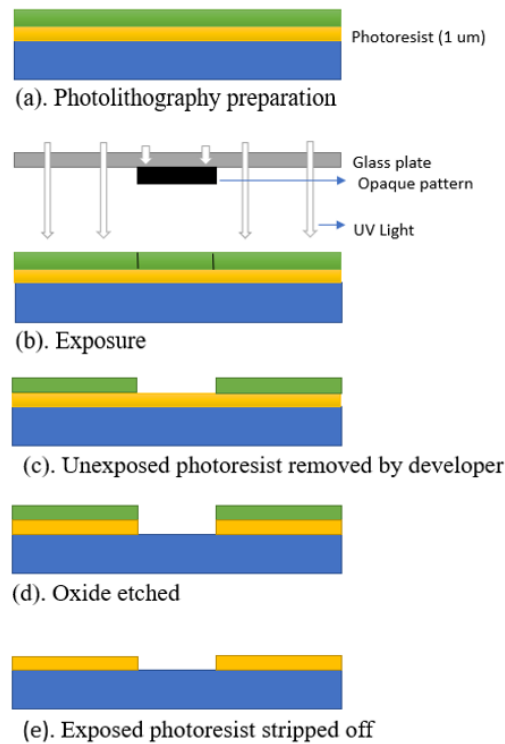


Figure 17: Highlighted photolithography steps

Etching

After the patterns have been protected by the photoresist the unprotected metals were etched by a combination of both wet and dry etching. The former was used to remove the unprotected Aluminum layer using Al etchant at room temperature for about 30 minutes and then thoroughly rinsed in deionized water while the latter removed unprotected Platinum and Titanium layer using the AJA ion mill at a 45-degree angle and a milling time of ~ 25 minutes. This was followed by the photoresist stripping by soaking the wafer in a solution of 1165 resist stripper in an ultra-sonic bath for about 30 minutes.



(a)



(b)

Figure 18: Etching (a) Wet etching with Aluminum etchant (b) Dry etching with AJA ion mill

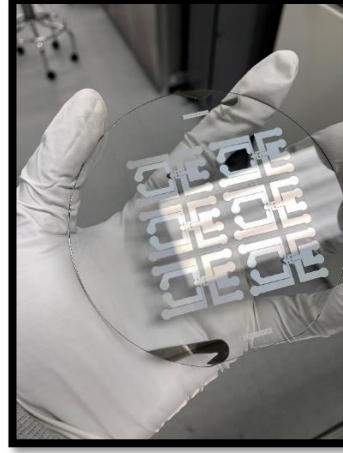
Upon the development of the first metal pattern which made up the heater leads, similar processes were followed to shape the heater, however in this case the Aluminum layer was etched in order to increase the electrical resistance of the heater as compared to its leads.

SiO₂ deposition

After the development of the heater and its leads, a 1 μm layer of SiO₂ was deposited to electrically insulate the heater from the RTDs. This was done using an OXFORD PEVCD operated at a deposition rate of 295 nm/min. The replica of the metal deposition order and rate, photolithography process and etching were carried out on the SiO₂ layer with specific masks to form the RTDs and their corresponding leads. This was followed by another SiO₂ deposition measuring $\sim 3 \mu\text{m}$ to electrically insulate the RTDs and protect the micro device.



(a)



(b)

Figure 19: SiO₂ deposition (a) To electrically insulate the heater from the RTDs (b) To electrically protect and insulate the micro device from the environment

SiO₂ etching

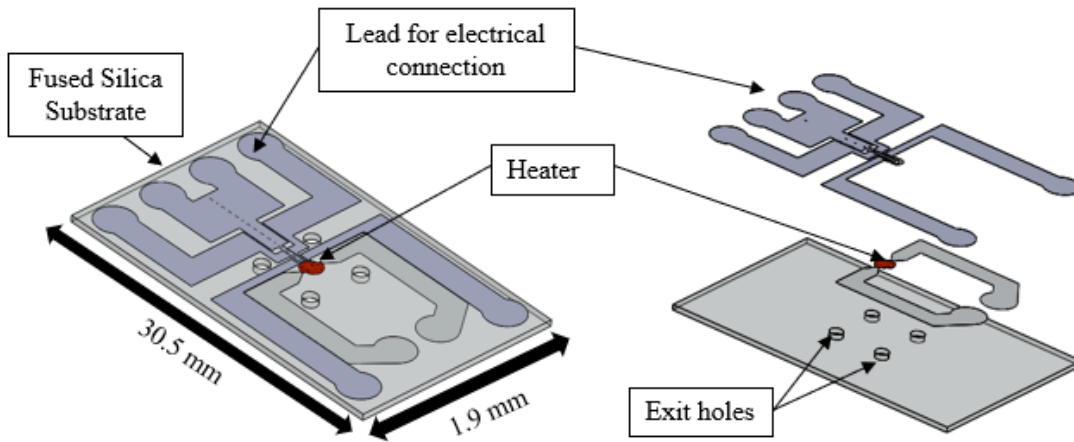
A final photolithography step was carried out to etch the SiO₂ layer exposing the RTD, and heater leads for electrical connections. This was done by an OXFORD 82 dry etch at an etching rate of 34.4 nm/min.

Dicing and micro drilling

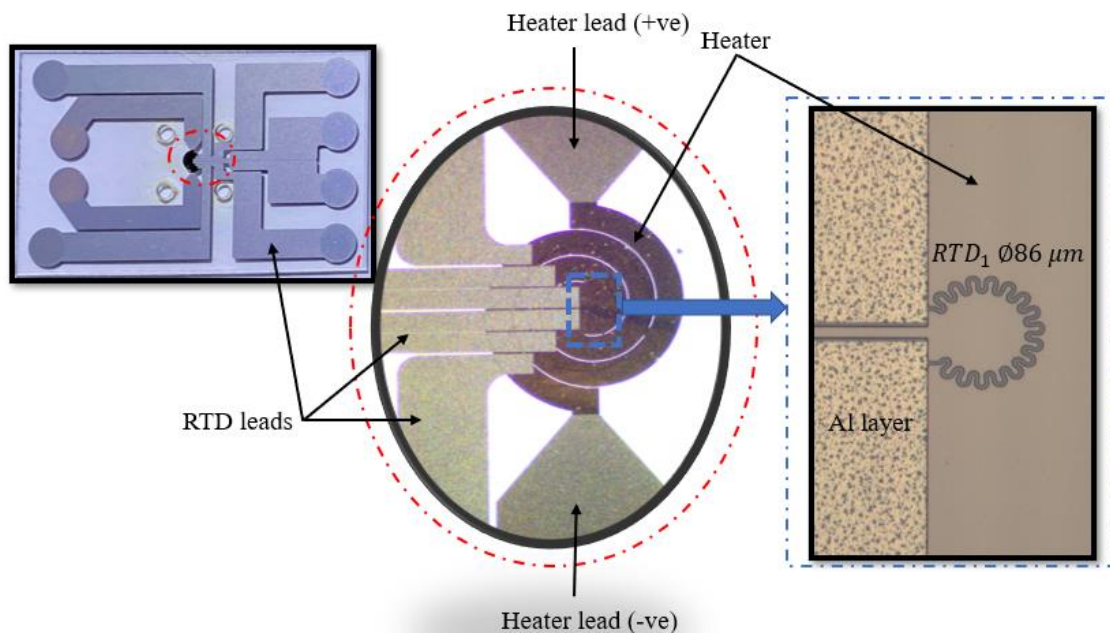
The wafer was diced to produce individual micro devices and finally micro drilled to allow the passage of spent fluid during the experiment. The dicing machine diced the wafer horizontally and vertically by carefully positioning the dicing blade on the dicing grip features printed on the wafer during the photolithography process.

2.1.5. Conclusion

We were able to micro fabricate a microfluidic device with heating and measuring properties similar to a heat dissipating device. The device comprised of a fused silica substrate with a hardness of 5.5 and a thermal conductivity of 1.38 W/m.K, a serpentine heater with a surface area of $4.88 \times 10^{-5} \text{ mm}^2$, three RTDs with RTD_1 being the stagnation zone and four holes drilled into the substrate to allow for passage of pent fluid – Fig 20.



(a)

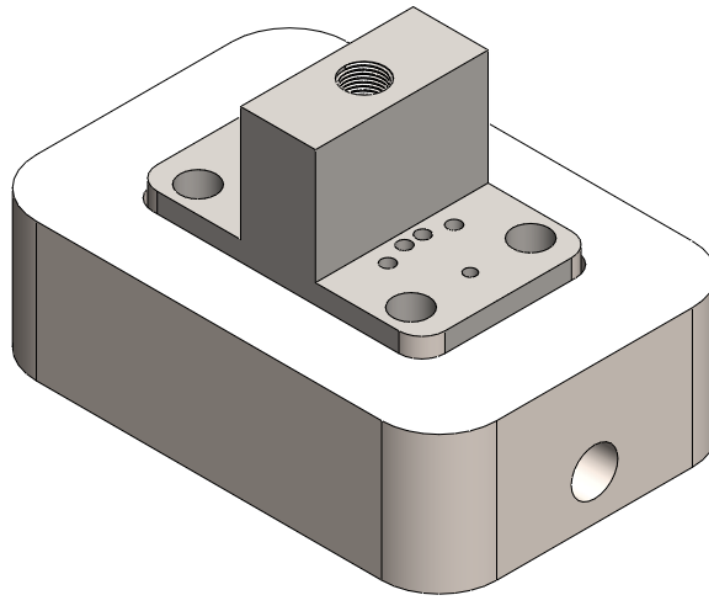


(b)

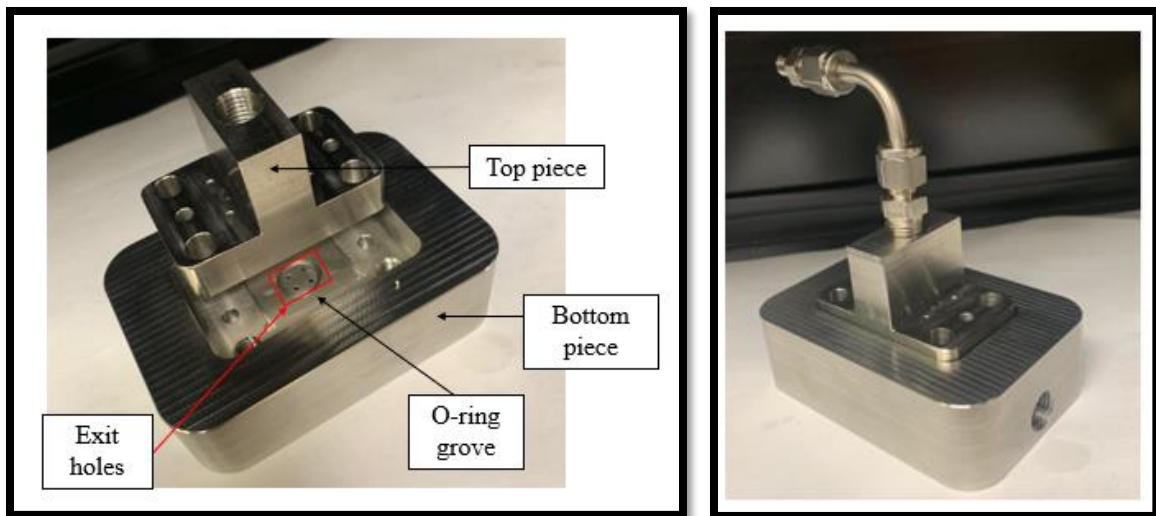
Figure 20: Final micro device images (a) CAD model showing layout (b) Real-life image with microscopic images of the device

2.2. Micro Device Housing

The device was housed between two metal pieces made of type 304 stainless steel — the bottom piece, which accommodated the device, and the top piece where the nozzle exit was placed (Fig. 21). The material was selected to withstand a pressure of about 10 MPa and because of its low thermal conductivity limiting heat loss by conduction. Within the bottom piece were two pockets to accommodate the micro device and the top piece, four exit holes, collectively linked to a single exit channel, one O-ring groove to accommodate an O-ring to ensure appropriate seal and prevent fluid leakages, two pin slots for top piece alignment, and four screw holes to fasten the top and bottom pieces together. The pockets were machined with precise dimensions and tolerances to accommodate the device and the top piece. The top piece was composed of the jet orifice, the fluid inlet, eight holes for contact pads access, two pins for top-bottom alignment, one O-ring groove with dimensions similar to that in the bottom piece, and four screw holes. Four 5/16 socket head bolts and nuts are used to tighten the pieces together. The bolts were screwed with a torque wrench at a specified torque to avoid cracking the device. The nozzle configurations were machined in the top piece for both single and multi-jets configurations. with a nozzle exit of $\varnothing 206 \mu\text{m}$. The pieces are chamfered at the edges for aesthetic reasons and most importantly to reduce the possibilities of sharp edges, which could be hazardous during operation. Two NPT pipes were fitted in the inlet and exit holes channeling the fluid from the entry, through the nozzle, and finally to the atmosphere.



(a)



(b)

Figure 21: Micro device package (a) CAD model showing the top piece and bottom piece (b) Real-life image of package after manufacture

The device was clamped between two O-rings to ensure appropriate seal and to prevent leakages during experiment. The package presented a confined jet configuration with the jet bounded by the top piece and the micro device.

Single jet

As aforementioned the jet configurations were machined in the top piece while the bottom piece supported the device. A single round hole was drilled in the top piece at the center with a depth of 1500 μm . Upon drilling, the hole measured about $\varnothing 206 \mu\text{m}$ at the exit representing the single jet.

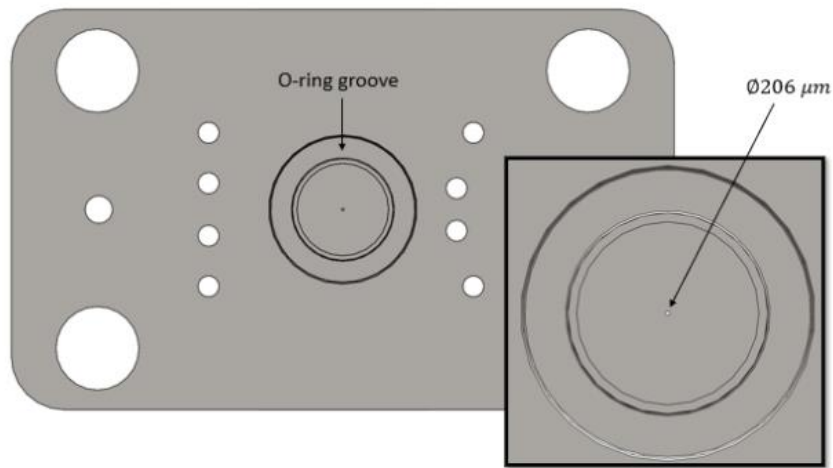


Figure 22: CAD model of single jet configuration

Multi-jet

Similar to the single jet, the nozzles were machined into the top piece with configurations shown in Figs. 4(a), 4(b) and Table 1. The jets' configuration consisted of a concentric distribution of the jets with an interjet spacing (S/d) of ~ 1.5 to allow for a uniform distribution of the jets over the RTDs. Upon drilling, the holes averagely measured $\varnothing 206 \mu\text{m}$ at a depth of 1500 μm each.

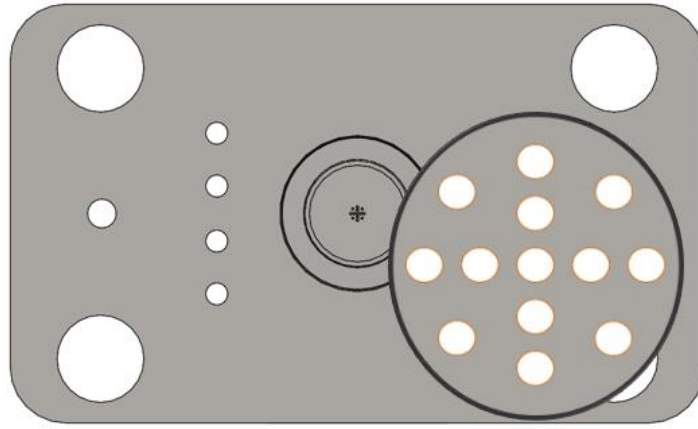


Figure 23: CAD model of multi jet configuration

2.2.1. Fluid Flow Direction

The fluid flow direction is shown in Figs. 24 and 25 classified into three states (Fig. 25(b) to 3(d)) – pre-impingement, impingement and post-impingement states. The pre-impingement state is characterized as the fluid flow immediately after it exited the nozzle exit. Here the jet centerline velocity was assumed to be the same as the exit velocity. The impingement state is characterized as the fluid flow upon impingement on the heater. Here the jet velocity was reduced as a result of entrainment of the ambient fluid within the micro domain, with the jet spreading radially outward towards the wall jet region (exit holes). The final state “post-impingement” constituted of the radial flow of the jet after impingement into the exit holes, collected in a single exit channel as seen in Fig 3(c).

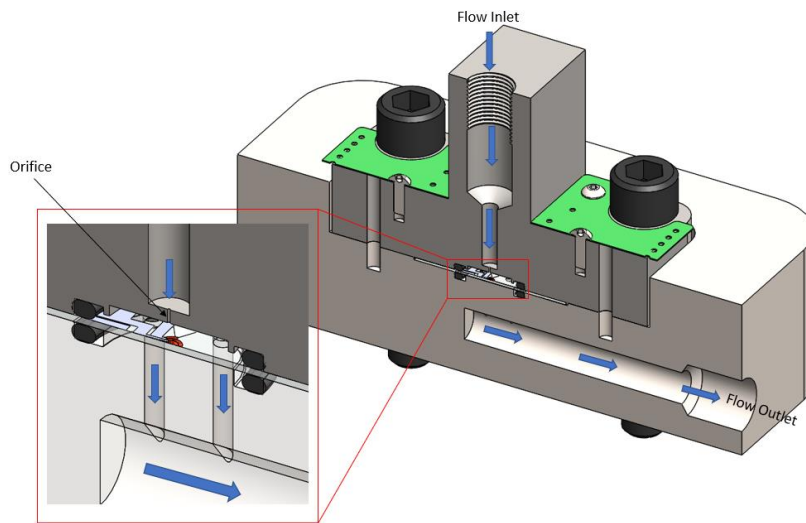
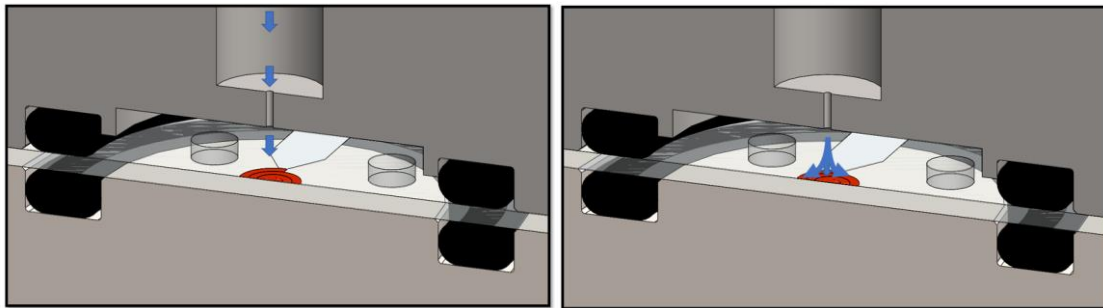
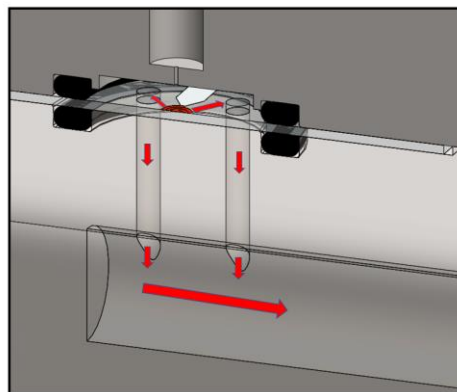


Figure 24: Sectional view of micro device package showing flow direction



(a)

(b)

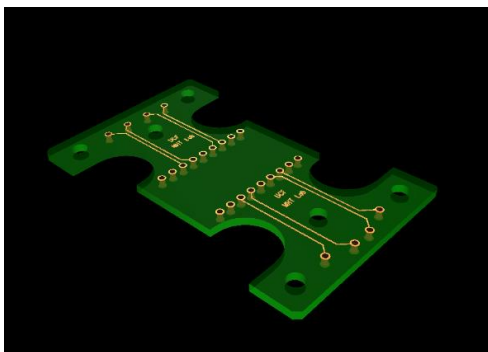


(c)

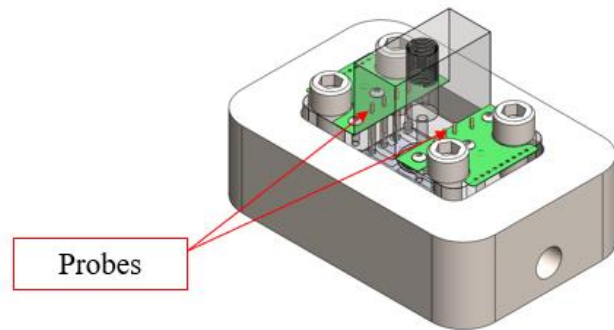
Figure 25: Fluid direction state (a) pre-impingement (b) impingement (c) post-impingement

2.2.2. Electrical connection

A printed circuit board (PCB) was designed using PCB123 software as seen in Fig 26. and manufactured to mechanically support and electrically connect the leads to a data acquisition system. The PCB boards consisted of a 0.062" thick board with pad width of 0.066" and hole diameter of 0.05" which were evenly divided upon manufacture. Power was supplied to the heater through two S-1 SERIES contact probes while data were taken from six other S-1 SERIES contact probes fixed into the top piece in contact with the RTD leads.



(a)



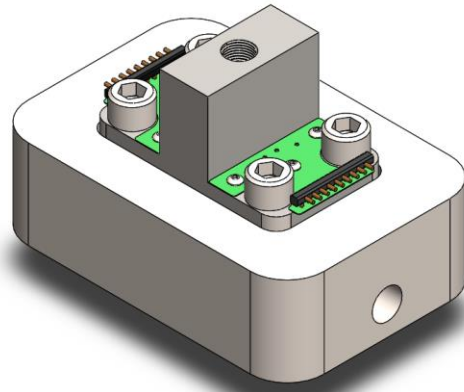
(b)

Figure 26: Electrical connection (a) Designed PCB (b) Contact probe arrangement

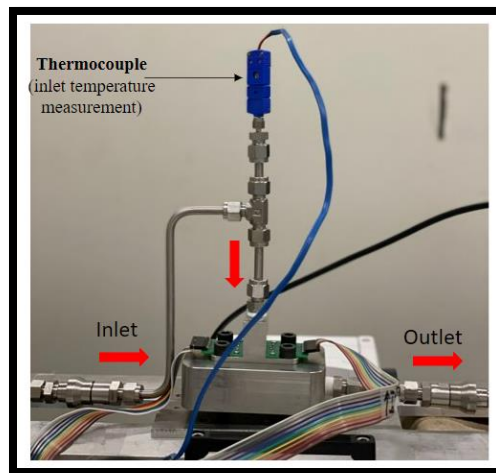
2.2.3. Conclusion

A micro device was designed and manufactured to mechanically and electrically support the micro device. The package was analyzed for both structural and static analysis to validate the experimental objective. The package was designed on SolidWorks and manufactured using computer numerical controlled machines. The jets were micro drilled with at the center of the top piece allowing the flow of the jet onto the device. Four exit holes were machined in the bottom

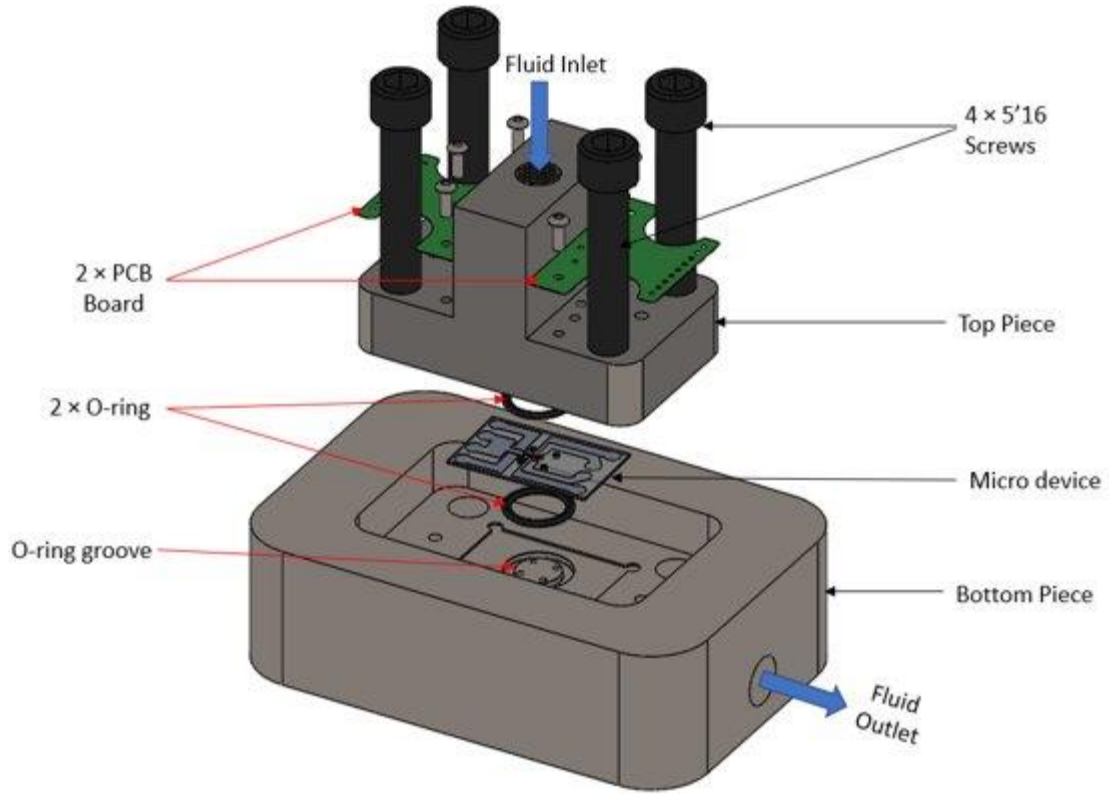
piece collectively linked to one single channel for the passage of the spent fluid out of the micro domain. The layout of the package is shown in Fig 27.



(a)



(b)



(c)

Figure 27: (a) CAD model of final package assembly (b) Real-life image of package installation in the fluid line (c) Exploded view of device package

2.3. Experimental Loop

The experimental open loop, shown in Fig. X, comprised of two tanks each containing CO₂ gas and N₂ gas, pressure regulators, a high-pressure vessel tank containing a separating vessel, three ball valves, one three-way valve, two PX309-5KG5V Omega pressure transducers, two preheaters and a MC-Gas Alicat scientific flow meter. The experimental aim was to achieve a pressure about 4.8 to 15 MPa, an inlet fluid temperature of 295 to 350 K and a mass flow rate up

to 1 g/sec. Before the selection of this configuration, both open and closed loop configurations were considered, however due to the cost value of purchasing a pump to circulate low flow rate, the open loop system was adopted. This selection was also strengthened by the CO₂ low toxicity property making it nonhazardous to the environment. Upon the start of each experiment, the high-pressure tank was emptied and then filled with CO₂ regulated by a pressure regulator and a three-way valve, compressing the separating vessel against the inlet of the N₂ gas. The separating vessel was composed of a TOC11-40 high-pressure tubular reactor (double ended pressure vessel) containing a piston separator and an O-ring enclosure with a 7000-psi pressure rating. The piston together with the O-ring enclosure separated the CO₂ from the N₂ gas and allowed for compression within the cylinder of up to 7000 psi. This flow was then discontinued after which the N₂ gas was allowed entry into the high-pressure tank compressing the separating vessel against the initially occupied CO₂. The operating pressure was regulated by the pressure regulator attached to the N₂ gas tank, and after the system was stabilized, the three-way valve was switched, allowing the high-pressured CO₂ entry into/out of the microfluidic device through connecting loops. This high-pressured CO₂ was channeled into the package at the desired inlet pressure conditions, by controlling the three-way valve and the ball valve right before the first preheater and by controlling the pressure regulator of the N₂ tank. Two preheaters were located before the fluid entered and exited the package. These preheaters were made of BriskHeat's RKP heating tapes wound around the pipe with ends connected to a digital temperature controller where the heat supplied to the tapes was controlled. These preheaters were used to respectively control the inlet temperatures of the fluid and to avoid the Joule-Thompson effect at the exit as a result of a drastic pressure drop just when the fluid exited the package. Likewise, two PX309-5KG5V Omega pressure transducers

were positioned immediately upstream and downstream the package to record the inlet and exit pressures. These together with the needle valve, and a constant atmospheric pressure of 0.101325 MPa at the loop exit were used to control the experimental steady state conditions. A thermocouple was affixed in the jet's inlet just before it struck the heater to record the fluid's inlet temperature. Away from the second preheater a MC-Gas Alicat scientific flow meter was installed for the purpose of recording the mass flow of the CO₂ through the package.

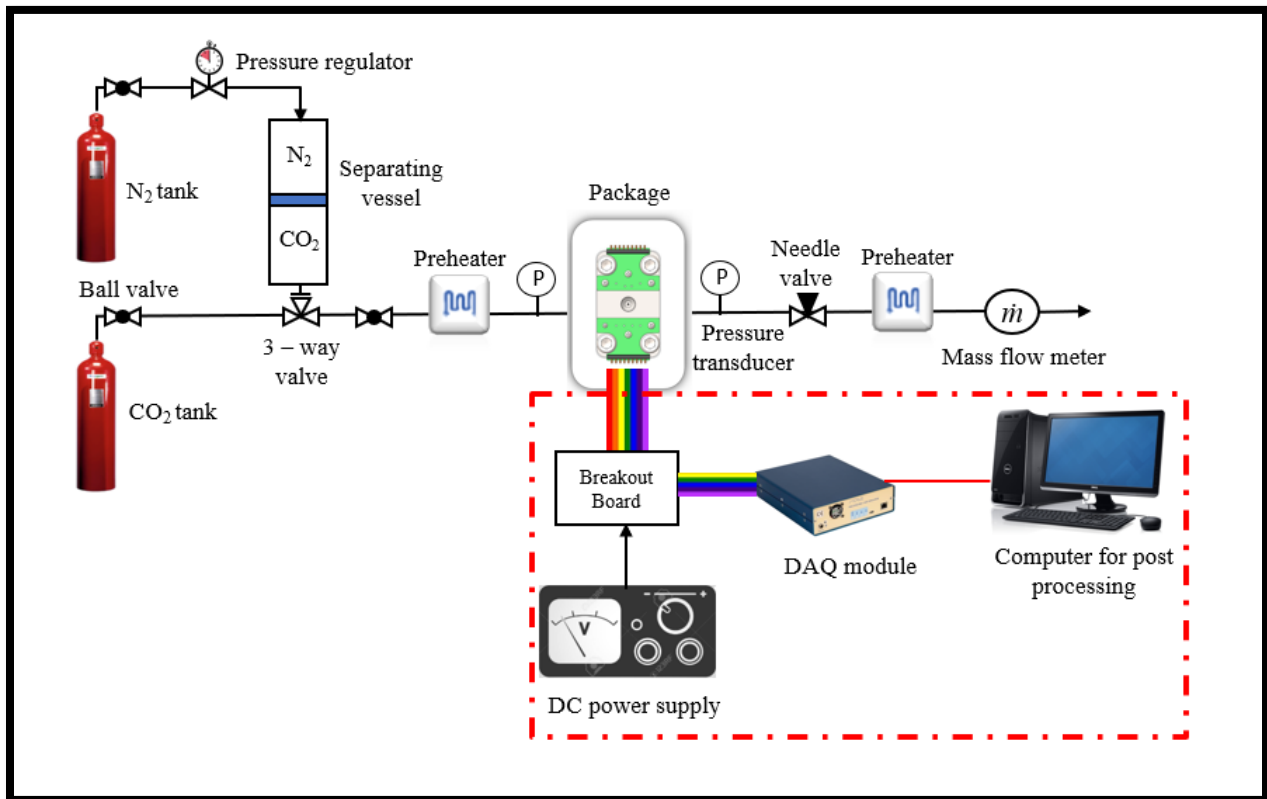


Figure 28: Schematic image of experimental loop

2.4. Data Acquisition and Processing

The sampling setup consisted of the power supply unit, multi meters, breakout board and sampling hardware. The temperature measurements were obtained from a temperature-resistance

curve fit generated for each RTDs and interpreted on a LabView software for data processing. The pressure transducers ranged from 0.1 to 34 MPa with an uncertainty of ± 0.017 MPa, likewise, there were two separate compatible mass flow meters: low mass flux range (0 to 20 slpm) and high mass flux range (0 to 100 slpm) to record the mass flow rate into the device. These flow meters had uncertainties of ± 0.1 slpm and ± 0.5 slpm respectively.

The local surface temperatures over the heater were measured by the radial distribution of the RTDs, however before collection of the data, the RTDs were calibrated to generate a linear temperature-resistance curve to be incorporated in the data acquisition and processing unit. To do this, prior to the start of the experiments, the device was placed in another package made of copper ($k = 407$ W/m K) to ensure a more efficient and uniform heat spread over the heater. The temperatures of the device in this exercise were recorded by placing the package in a temperature-controlled oven (Quincy lab, 30AFE Mechanical Convection Oven) with controls to regulate the interior temperature. Inside the oven were two thin wired thermocouples - affixed to the device within the package (right at the heater area) and in the oven space very close to the package. The thermocouples simultaneously recorded the temperatures of the oven and that of the heater at a specific time. The RTD leads were connected to a cDAQ and SCXI 1102 made by National Instruments™ through six contact probes soldered to two PCBs, and the oven was sealed tight to avoid entrainment from the outside environment. The device was calibrated from 21 °C to 90 °C by gradually increasing the oven's temperature with steps of 5 °C and recording the measured RTDs' resistances when the two thermocouples achieved uniform temperatures and at steady state which took approximately 40 minutes per temperature step. The data were then collected and

processed on a Python programming language software to generate the temperature-resistance curves of each RTD, and their preceding correlation as seen in Fig 29.

The measured resistance-temperature relations were curve fitted, has shown in Fig. 29 and expressed in Table 2.

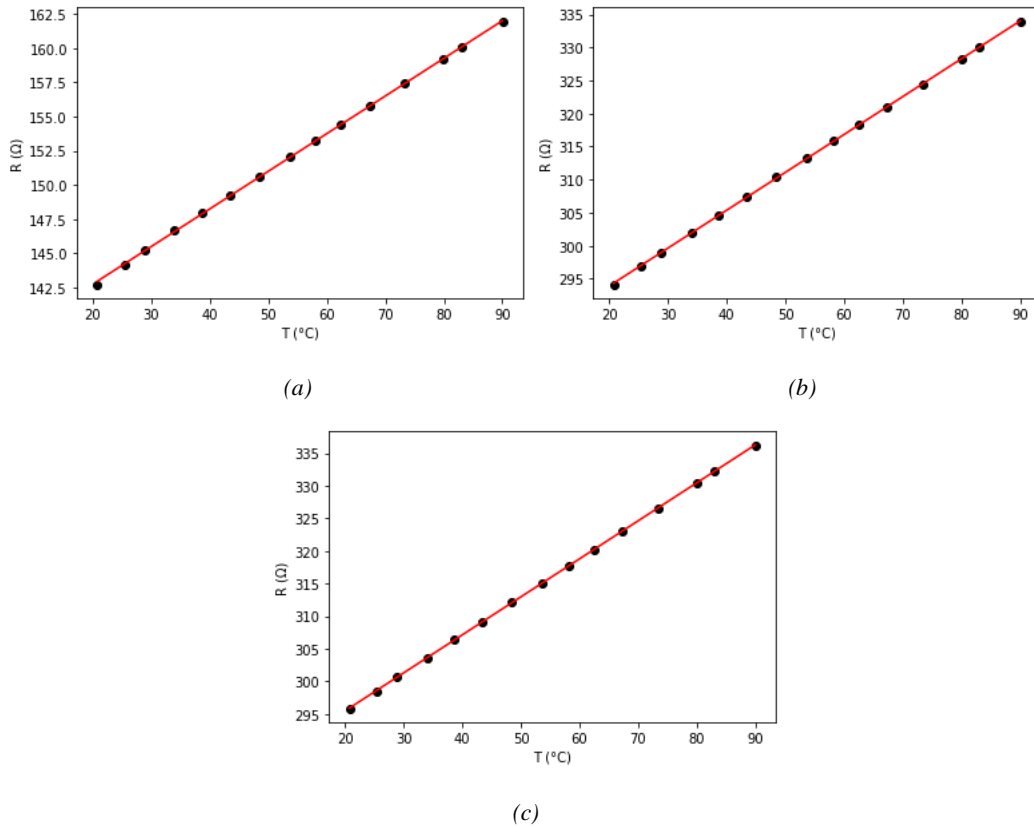


Figure 29: Temperature -resistance curve (a)RTD₁ (b) RTD₂ (c) RTD₃

Table 2: Temperature-resistance correlation for each RTD

RTD _L	Equation	R ²
RTD ₁	$T = \frac{R-137.251}{0.275} \text{ } ^\circ\text{C}$	1.0
RTD ₂	$T = \frac{R-282.417}{0.574} \text{ } ^\circ\text{C}$	1.0
RTD ₃	$T = \frac{R-283.805}{0.583} \text{ } ^\circ\text{C}$	1.0

2.5. Data Reduction

The local *HTCs* as measured by the RTDs were calculated as:

$$h = \frac{q''}{T_{s,i} - T_{sat}} \quad (1)$$

where q'' is the net heat flux from the heater, $T_{s,i}$ is the locally measured surface temperature by the RTDs during the experiment, and T_{sat} is the fluid saturation temperature. The heat flux was calculated according to:

$$q'' = \frac{P}{A_H} - q''_{loss} \quad (2)$$

where A_H is the area of the heater, q''_{loss} is the average heat flux lost to the environment, and P is the power supplied.

The average *HTC* was calculated as

$$h_{avg} = \frac{q''}{T_{s,i} - T_\infty} \quad (3)$$

$$\overline{T_{s,l}} - \overline{T_{sat}} = m_i r_{avg} + b_i \quad (4)$$

$$r_{avg} = \frac{\int_0^{r_{max}} 2\pi r^2 dr}{\int_0^{r_{max}} 2\pi r dr} = \frac{2r_{max}}{3} \quad (5)$$

where $\overline{T_{s,l}} - \overline{T_{\infty}}$ is the average superheat temperature change inferred at the mean radius (r_{avg}) where r_{max} is the maximum heater radius. The average surface temperatures, $\overline{T_{s,l}}$, at each RTD location and heat flux were measured and used to estimate the slope (m_i) and intercept (b_i). Then, the averaged saturation temperature over the experiment was subtracted from this temperature ($\overline{T_{s,l}}$) to determine $\overline{T_{s,l}} - \overline{T_{\infty}}$.

In the single-phase experiment (sCO₂), T_{∞} was noted as T_0 recorded from the RTDs with no heat flux from the heater. This gave a more approximate measurement of the fluid temperature. While in the flow boiling experiment, T_{∞} was noted as T_{sat} by averaging the recorded inlet fluid temperature as measured by the inlet thermocouple together with those measured by the RTDs with no heat flux from the heater.

The inlet Reynolds number was estimated as

$$Re = \frac{\rho u d}{\mu} \quad (6)$$

where ρ is the inlet fluid density, u is the average velocity at the inlet, d is the nozzle exit diameter, and μ is the dynamic viscosity of the fluid at the inlet.

The average jet velocity was estimated as

$$u = \frac{\dot{m}}{\rho A_d} \quad (7)$$

where A_d is the nozzle exit area.

The local and average Nusselt number were calculated as

$$Nu = \frac{hd}{k_f} \quad (8)$$

$$Nu_{avg} = \frac{h_{avg}d}{k_f} \quad (9)$$

where d is the nozzle diameter and k_f is the fluid's thermal conductivity at the inlet.

The inlet vapor quality was calculated according to:

$$x_{in} = \frac{h_{in} - h_{f,in}}{h_{fg,in}} \quad (10)$$

where $h_{f,in}$ is the enthalpy of saturated liquid, $h_{fg,in}$ is the latent heat of vaporization, and h_{in} is the enthalpy of the fluid at the nozzle inlet. These values were extracted from NIST REFPROP based on the inlet temperature and pressure.

The radial mass quality was calculated as

$$x_r = \frac{h_r - h_{f,r}}{h_{fg,r}} \quad (11)$$

where $h_{f,r}$ and $h_{fg,r}$ are, respectively, the enthalpies of saturated liquid and latent heat of vaporization of the fluid based on the radial temperature of the fluid measured by the RTDs. h_r is the enthalpy of the local fluid at the RTD position calculated as

$$h_r = \frac{\dot{q}}{\dot{m}} + h_{in} \quad (12)$$

where \dot{q} is the power dissipated to the fluid, which accounts for the heat lost by conduction, and \dot{m} is the mass flow rate. The average radial mass quality was calculated like the average surface temperature as

$$\bar{x}_r = m_i r_{avg} + b_i \quad (13)$$

where the slope, m_i , and b_i were calculated from the line connecting the radial mass quality at each heat flux.

The superheat temperature (ΔT_{sat}) of the heat transfer surface was calculated as

$$\Delta T_{sat} = (\overline{T_{s,i}} - T_{sat}) \quad (14)$$

The mean absolute error (MAE) was estimated as

$$MAE = \frac{1}{N} \sum_1^N \frac{prediction - experiment}{experiment} \times 100\% \quad (15)$$

2.6. Heat Loss Estimation

Since there exists a fraction of heat lost by conduction from the device's substrate, the heat lost for the experiment was experimentally analyzed. To do this the device was first evacuated, and power was supplied to the heater with no fluid flow ($G = 0$) at small increments. At zero mass flux, all heat dissipated by the heater consisted of the heat loss, which was a function of the surface temperature. Heat flux-local surface temperature curves were generated for all *RTDs* depicted in Fig. 30. The slope that corresponded to the resistance by conduction was estimated at each *RTD* as:

$$R_{cond} = \frac{\Delta T_{s,i}}{\Delta q''} \quad (16)$$

$$\Delta q'' = q''_{loss} \quad (17)$$

where $\Delta q''$ is the heat flux lost to the environment.

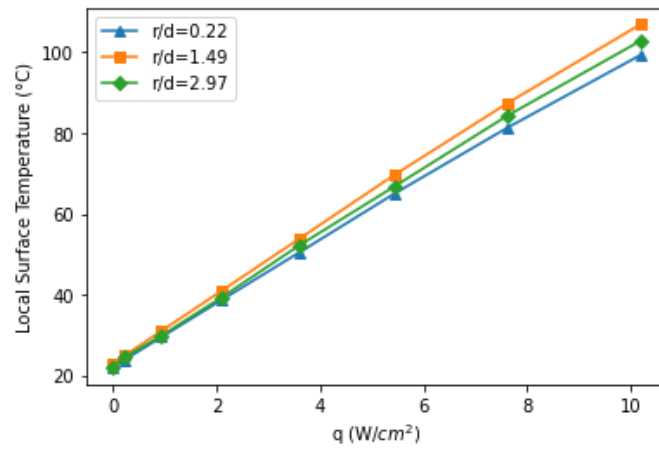


Figure 30: Heat loss estimation

CHAPTER THREE: SINGLE MICRO IMPINGING JET WITH SCO₂

The contents of this chapter have been published in:

Adeoye, S., A. Parahovnik, and Y. Peles, A micro impinging jet with supercritical carbon dioxide. International Journal of Heat and Mass Transfer, 2021. 170: p. 121028 [100]

3.1. Introduction

A growing number of studies explored impinging jet cooling at the micro scale [102-104] and reported a significant heat transfer enhancement compared to results at the conventional scale. Shen and Gau [103] experimentally investigated micro-scaled impingement cooling on a thermal chip with arrays of sensors and heaters and noted that both the heat transfer process and the impinging jet flow structure are notably different from that at the macro scale. Patil and Narayanan [104] conducted an experimental study about impinging circular microscale jet (125 μm) for a range of Reynolds numbers (690-1770) at three standoffs ($2d$, $4d$, and $6d$). The average Nusselt numbers were compared to the study of Martin [39], which were about 40% lower for lower Reynolds numbers (< 1000) and about 25% higher at higher Reynolds numbers (> 1700). An experimental study by Glynn and Murray [32] reported 20% to 70% increase in the stagnation zone HTC when the jet diameter was reduced from 1.5 mm to 1 mm. Anand and Jubran [29] numerically showed a 37.3 % increase in the HTC when the nozzle diameter was reduced from 0.5 mm to 0.25 mm.

A more recent study [105] has shown that an array of single-phase micro jets with water can attain a heat transfer coefficient of up to 414,000 $\text{W/m}^2 \text{K}$ at a Reynolds of 3290, a corresponding Nusselt

number of 76 and a heat flux of up to 1110 W/cm^2 . Although this bespeaks the high performance of water for cooling, its compatibility with electronics is a concern. For this reason, several refrigerants, such as R134a and R113, were studied [106], but because of low thermal conductivity, their heat transfer capabilities are inferior to water. To alleviate this issue, jet boiling was also a topic that has been carefully examined. For instance, Browne et al. [41], and Zhou and Ma [49] investigated flow boiling of R134a and R113, respectively, and demonstrated a significant heat transfer enhancement. However, the microelectronics industry has been reluctant to adopt flow boiling heat transfer methods for thermal management systems because of reliability issues.

With the recent reemergence of carbon dioxide (CO_2) as a viable coolant around the critical state (304.13 K and 7.3 MPa), its cooling applicability has been a topic of interest as discussed above. This is partially because of the thermophysical property variations of CO_2 and its high specific heat and thermal conductivity near the pseudocritical condition, a condition corresponding to a significant change in the thermophysical properties of the fluid at or slightly above the critical condition (chapter 1). Above all, its ability to adopt properties midway that of liquid and gas and its low toxicity and environmental impact serve as a trademark in hypothesizing that it could be a better replacement for traditional cooling fluids while still achieving high HTC . As part of this new development, Chen et al [107] performed experiments with supercritical CO_2 ($s\text{CO}_2$) with a 20 mm nozzle diameter, and reported a maximum average HTC of $5000 \text{ W/m}^2 \text{ K}$ at a mass flow rate of 8.34 kg/h . The maximum local HTC also occurred at the stagnation zone and decreased radially. Joo-Kyun and Toshio [108] conducted numerical analysis on axisymmetric laminar jet impingement cooling of an isothermal flat surface with $s\text{CO}_2$ and reported that the heat transfer was better when the inlet temperature was close to the pseudocritical condition. Chen et al. [109]

conducted a numerical study of heat transfer characteristics of confined round jet impingement on a flat silicon plate at constant heat flux with sCO_2 and reported a high average HTC due to the high specific heat of the fluid in its supercritical state.

While jet impinging cooling has been extensively studied at the macro scale, and more recently at the micro scale, the heat transfer characteristics of micro jets impinging with a fluid that is experiencing significant property changes, such as CO_2 , around the critical condition, has been rarely studied. Thus, this chapter reports on an experimental study about fluid flow and heat transfer of micro jet impingement with sCO_2 near the critical condition.

3.2. Results And Discussion

Susceptible heat transfer governance such as the radial position, heat flux, mass flux and inlet temperatures were experimentally studied to understand their influences of the heat transfer rate of sCO_2 . The range of operations is illustrated in Table 3 with the results discussed in the preceding section.

Table 3: Experimental Inlet conditions

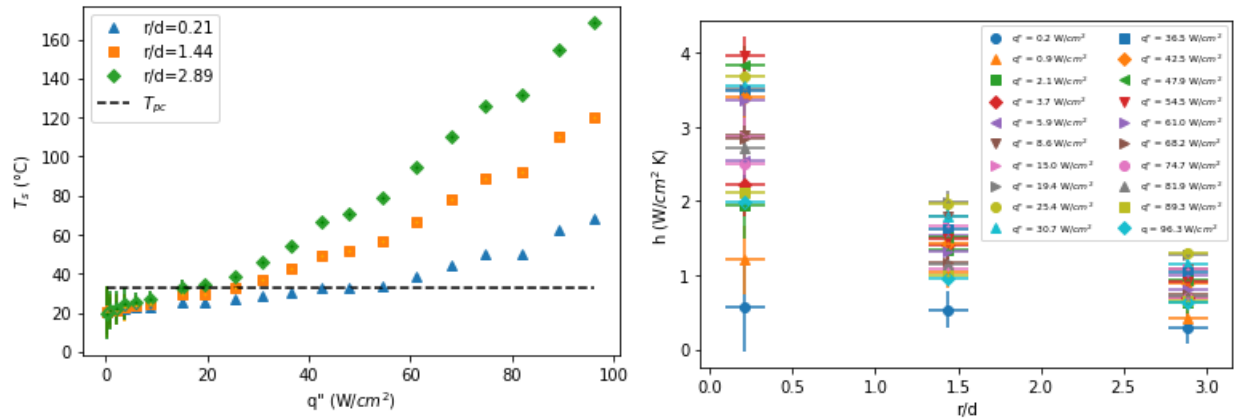
Parameter	Range
Radial position (r/d)	0.21, 1.44, and 2.89
Heat flux ($W/cm^2 K$)	0 ~ 100
Mass flux ($kg/cm^2 s$)	0.53 ~ 1.5
Inlet temperature ($^{\circ}C$)	22.1 ~ 38.6

3.2.1. Heat Flux and Radial Position Effect

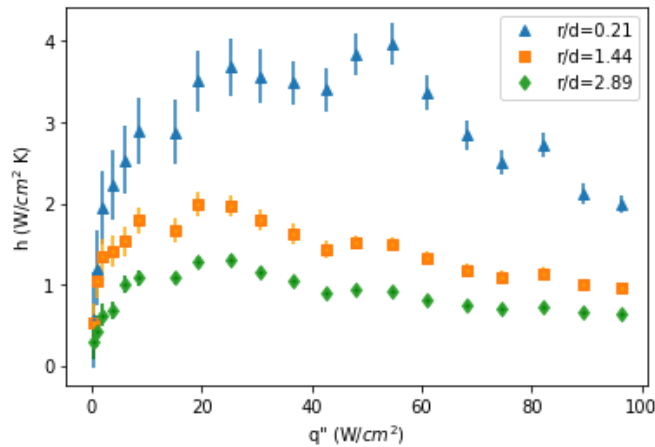
The heat flux varied from 0 to $\sim 100 \text{ W/cm}^2$ at a pressure of 7.45 MPa, a mass flux of 0.53 $\text{kg/cm}^2\text{s}$ (corresponding to a Reynolds number of $\sim 15,500$), and an inlet temperature of 21 °C. The locally measured surface temperatures by each RTD are depicted in Figure 31(a) as a function of heat flux, and Fig. 31(b) depicts the corresponding local *HTCs*. As expected, the local *HTC* decreased radially away from the stagnation zone for all heat fluxes. This is attributed to the jet hydrodynamics and radial position effect as explained in chapter 1. As the *sCO*₂ exited the nozzle, it assumed a uniform velocity profile as a result of little or no interaction with the stagnant fluid in the micro domain. Based on the operating conditions and according to Draksler et al. [25] the potential core length was estimated to be $\sim 1.2d$, such that the potential core region extended 247.2 μm into the micro domain. Right after the development of the potential core, the velocity degraded, building up static pressure in the stagnation zone. There the flow decelerated in the axial direction before impinging on the heater and then accelerated in the radial direction after impingement. This velocity characteristics and the high momentum caused the high *HTC* observed around the stagnation region. As the flow continued radially towards the exits, the influence of the impingement diminished, resulting in a velocity decline and ultimately a gradual diminishing of the *HTC* seen in the radial positions away from the stagnation zone.

Figure 31(c) depicts the local *HTC* as a function of heat flux. The *HTC* at $r/d = 0.21$ first increased with heat flux, then decreased, and finally increased to a peak before decreasing drastically. Away from the stagnation zone (i.e., $r/d = 1.44$ and 2.89), the *HTC* increased to a peak before decreasing with heat flux. Peak local *HTCs* of about 40,000 $\text{W/m}^2 \text{ K}$, 20,000 $\text{W/m}^2 \text{ K}$, and 10,000 $\text{W/m}^2 \text{ K}$ at

$r/d = 0.21, 1.44$ and 2.89 were recorded at heat fluxes of $54.5 \text{ W/cm}^2, 19.4 \text{ W/cm}^2$ and 25.4 W/cm^2 , respectively.



(b)



(c)

Figure 31: Radial position and heat flux effect (a) Local surface temperature as a function of heat flux; (b) Local heat transfer coefficient as a function of radial position for a range of heat fluxes; (c) Local heat transfer coefficient as a function of heat flux. Conditions: $p = 7.45 \text{ MPa}$, $T_{in} = 21.1^\circ\text{C}$, $G = 0.53 \text{ kg/cm}^2\text{s}$ W/cm^2

Figures 32(a)-32(c) show the local HTC and its corresponding surface temperature at $r/d = 0.21$, $r/d = 1.44$, and $r/d = 2.89$, respectively. The peak local HTC observed at the three radial positions

was achieved when the local surface temperature was around the pseudocritical temperature (T_{pc}), corresponding to a fluid flow experiencing rapid variation in the thermophysical properties that modified the heat transfer process. Similarly, the area-average HTC with the corresponding average surface temperature, shown in Fig. 32(d), also peaked when the average surface temperature was slightly above the pseudocritical temperature.

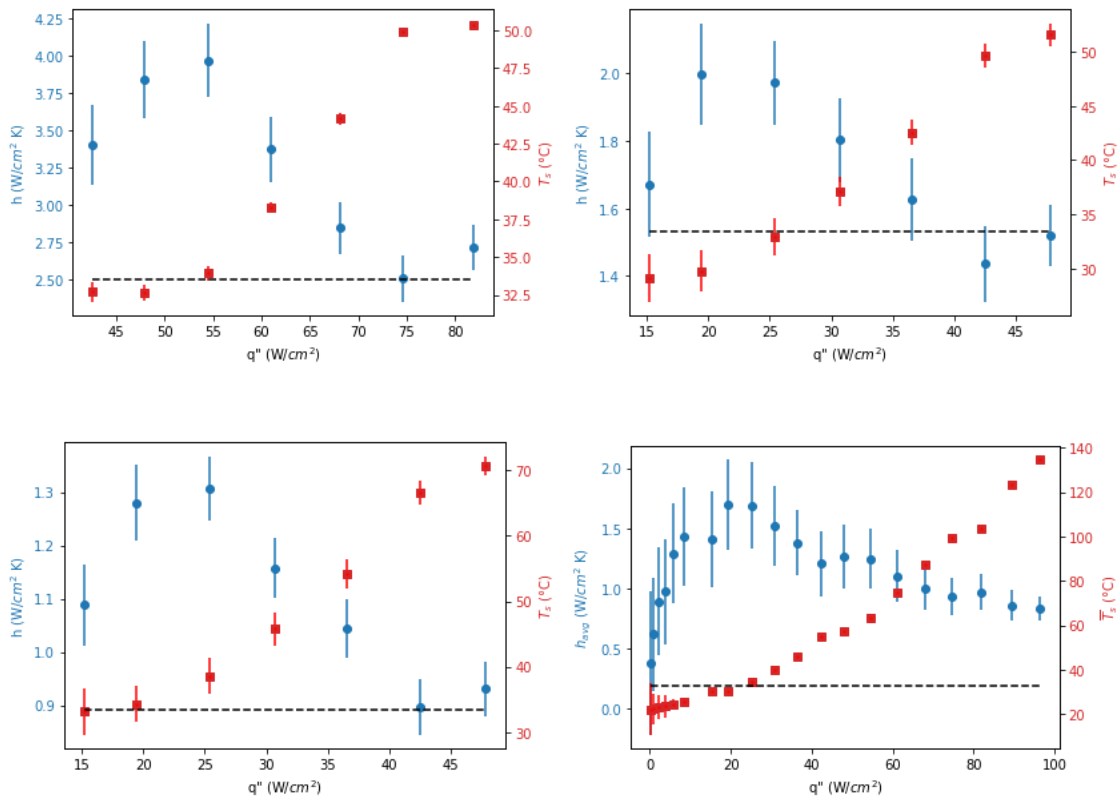


Figure 32: Local heat transfer coefficient and surface temperature as a function of heat flux. (a) RTD1, (b) RTD2, (c) RTD3, (d) Average heat transfer coefficient and average surface temperature as a function of heat transfer rate. The dashed horizontal line in (d) represents the pseudocritical temperature

While the HTC is generally not a function of heat flux for single-phase flows with approximately constant thermophysical properties, it is for sCO_2 near the critical conditions. As the fluid temperature was modified by the heat flux, so were the properties of sCO_2 . Specifically, when the

fluid temperature experienced a transition across the pseudocritical conditions, its specific heat and thermal conductivity increased rapidly and then decreased. This was accompanied by sharp decreases in the dynamic viscosity and density. The large increase in the specific heat acted somewhat like that of latent heat, such that the fluid temperature near the pseudocritical condition hardly increased with heat addition — a favorable process that tends to increase *HTC*. Likewise, the sharp increase in the thermal conductivity was associated with enhanced conduction, which also led to higher *HTC*. In addition, the decrease in the dynamic viscosity increased the local Reynold number (enhanced turbulence), and thus, increased advection heat transfer. On the other hand, the sharp decrease in the density accelerated the flow, which could have adversely affected the *HTC* as discussed by [110]. This was because the accelerated flow lowered the static pressure and generated favorable pressure gradients, which led to a phenomenon known as relaminarization — an increase in the thickness of the viscous sub-layer and a decrease in the thickness of the turbulent boundary layer. This in turn, increased the thermal resistance from the wall to the fluid, and thus, decreased the *HTC*. The favorable effects that tended to enhance the *HTC* dominated the one potential adverse effect (i.e., flow acceleration) such that the overall result yielded an increase in the *HTC* when the flow gradually crossed the pseudocritical conditions. It should be noted that flow acceleration in jet impingement has usually been ascribed to the presence of secondary peaks in the *HTC* in certain radial positions ($r/d \approx 1.5$ to 2) as discussed in chapter 1 (standoff effects). These peaks have also been attributed to a secondary recirculation zone as a result of the confining top surface. However, the presence of secondary peaks was not observed in this study as the *HTC* declined radially in all cases studied. This might be due to the radial positions selected for *RTD*₂

and RTD_3 or for a fully developed flow towards these temperature sensors and/or the dimensionless standoff ($L/d = 7.3$).

To quantify the contribution of the specific heat on the increased HTC , a specific heat analysis was conducted. For this the increase in the mean fluid temperature was calculated and compared to the experimentally obtained average surface temperature change, $(\overline{T_{s,l}} - \overline{T_0})$. The mean fluid temperature in the micro domain at each heat flux ($T_{m,i}$) was estimated as

$$T_{m,i} = \frac{T_{s,avg} + T_{0,avg}}{2} \text{ } ^\circ\text{C} \quad (18)$$

$$\overline{T_0} = \frac{T_{0,RTD1} + T_{0,RTD2} + T_{0,RTD3}}{3} \text{ } ^\circ\text{C} \quad (19)$$

The average initial mean temperature ($T_{0,avg}$) was constant as it was obtained at $q'' = 0$. With the known mean fluid temperature at each heat flux, the corresponding specific heats were extracted from the NIST REFPROP database at a constant pressure of 7.45 MPa. (It should be noted that the maximum pressure drop recorded during the experiment was less than 0.1 MPa, and thus, a constant pressure of 7.45 MPa was used for all experiments). These specific heats were then used to compute the mean fluid temperature increase according to:

$$(\overline{T_{m,l}} - \overline{T_0})_e = \frac{q}{\dot{m}c_{p,f}} \quad (20)$$

$$(\overline{T_{m,i}})_e = \frac{q}{\dot{m}c_{p,f}} - \overline{T_0} \quad (21)$$

where q is the heat transfer rate in W, \dot{m} is the mass flow rate in kg/s, $c_{p,f}$ is the specific heat of the fluid, and $T_{m,i}$ is the average fluid temperature. To validate the mean fluid temperature an iterative procedure was utilized (Eq. 21), which took the values of the previously extracted specific

heats up until the value of $T_{m,i}$ marginally changed. The estimated average fluid temperature increase was compared to $(\overline{T_{s,l}} - T_0)$, as shown in Fig 13. As seen, the difference between the estimated average temperature change as a function of the fluid specific heat accounted for approximately $62 \pm 5\%$ of the experimental average temperature change at each specific heat indicating a higher dependency of temperature change profile on the specific heat, which in turn dictated the *HTC* trend. Likewise, the peak estimated specific heat corresponded to the peak area-averaged *HTC* as earlier shown in the experimental data. The residual $\sim 38\%$ ($T_{s,i} - T_m$) depicted in Fig. 33 could be attributed to the increased thermal conductivity around the pseudocritical conditions and/or other factors resulting in a new temperature change profile.

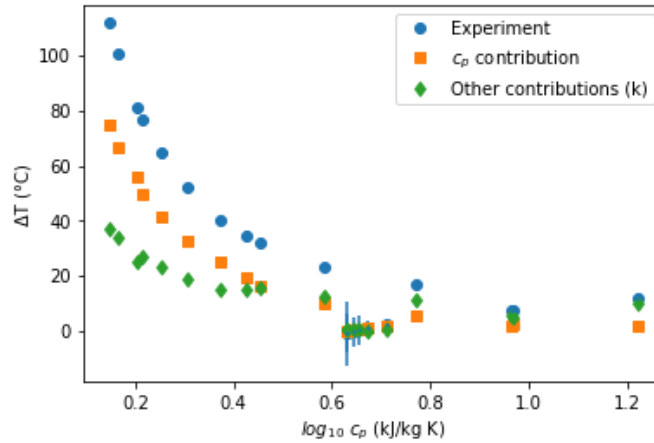
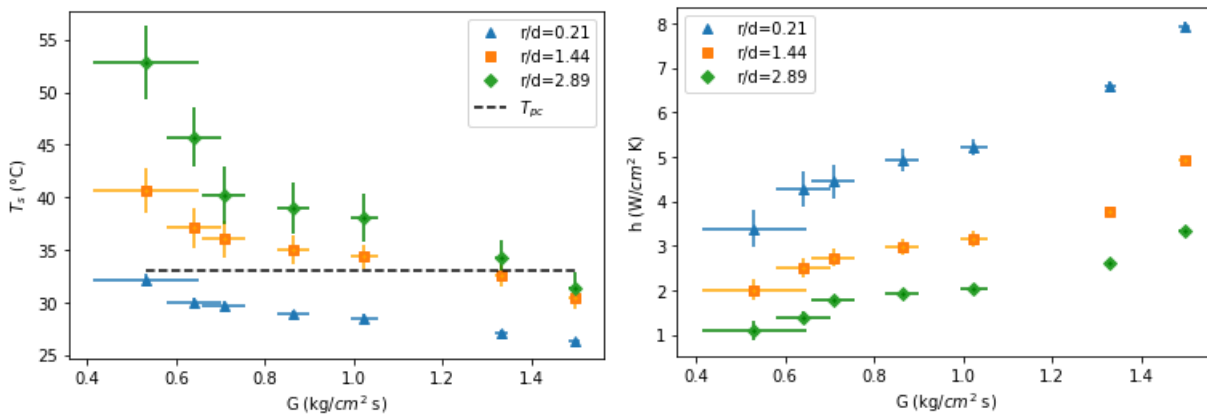


Figure 33: Specific heat effect on the heat transfer rate

3.2.2. Mass Flux Effect

The effect of mass flux was studied at an inlet pressure of 7.45 MPa, an inlet temperature of 21 °C, and a heat flux of 34.5 W/cm². The mass flux varied from 0.53 kg/cm²s to 1.5 kg/cm²s, corresponding to inlet Reynold numbers of approximately 15,500 to 44,000. Figure 34(a) shows

the local measured surface temperature and the associate HTC as a function of mass flux at the three radial positions. As expected, an increase in mass flux was accompanied by a decrease in the surface temperature and an increase in the HTC at all radial positions. In most cases, at the nozzle exit, the sCO_2 jet was turbulent as a result of high Reynolds numbers. As the sCO_2 impinged on the heater, a thin layer of hydrodynamic and thermal boundary was developed just beneath the jet due to the jet deceleration and the resulting increase of the static pressure, after which the flow accelerated in a direction parallel to the heater towards the micro device exit holes, greatly influenced by the mass flux. A higher velocity corresponded to an enhanced turbulent flow, and upon impingement on the heater, a greater velocity fluctuation was achieved enhancing the HTC . The radial position farther from the stagnation region ($r/d = 2.89$) attained a local HTC of approximately $33,000 \text{ W/m}^2 \text{ K}$ at a mass flux of $1.5 \text{ kg/cm}^2\text{s}$, similar to the one attained at the radial position at the stagnation region ($r/d = 0.21$) at a lower mass flux of $0.53 \text{ kg/cm}^2\text{s}$.



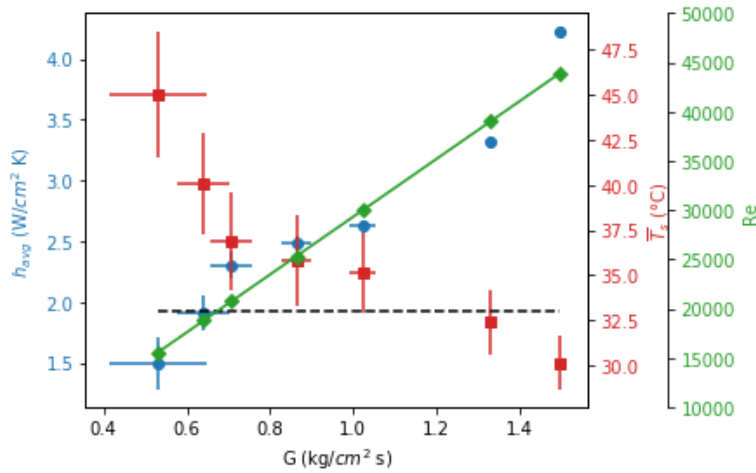


Figure 34: Mass flux effect (a) Local surface temperature as a function of mass flux; (b) Local heat transfer coefficient as a function of mass flux; (c) Area-averaged heat transfer coefficient and surface temperature as a function of mass flux. Conditions: $p = 7.45 \text{ MPa}$, $T_{in} = 21.1^{\circ}\text{C}$, $q'' = 34.5 \text{ W}/\text{cm}^2$

As shown in Fig. 34(c) the area-averaged $HTCs$ continued to increase with mass flux regardless of if the surface temperature was above or below the pseudocritical condition, suggesting that HTC was more dependent on the mass flux than the proximity of the flow to the pseudocritical conditions. Local surface temperatures at RTD_1 ($r/d = 0.21$) were always lower than the pseudocritical temperature and continued to drop with mass flux. However, those for RTD_2 and RTD_3 were higher and eventually dropped below the pseudocritical temperature conditions at the higher mass fluxes. At a constant heat flux, the heat transfer was strongly influenced by the mass flux undermining the effects of the drastic change in the thermophysical properties of the flow around the pseudocritical conditions.

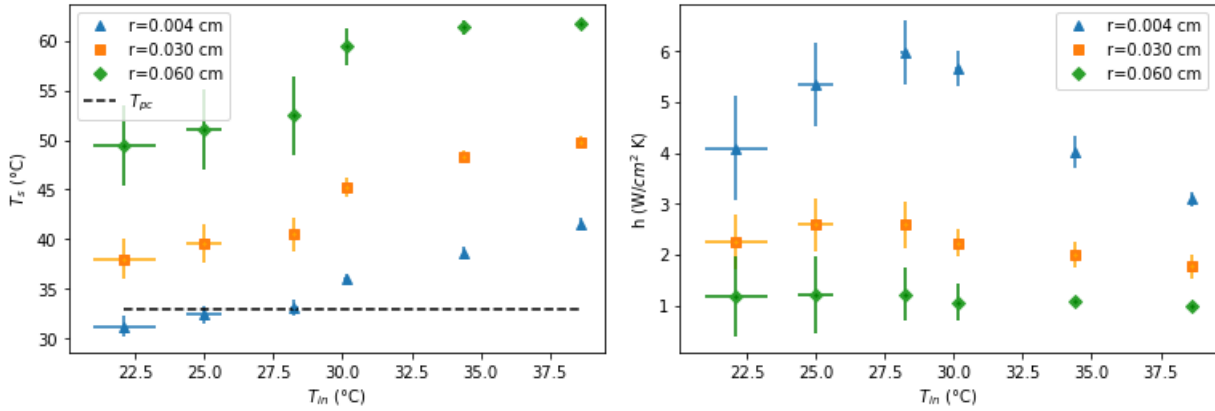
3.2.3. Inlet Temperature Effect

The effect of the inlet temperature was studied at an inlet pressure of 7.45 MPa, a mass flux of $0.53 \text{ kg}/\text{cm}^2 \text{ s}$, and a heat flux of $34.5 \text{ W}/\text{cm}^2$. The inlet temperature varied from 22.1°C to

38.6 °C. The local measured surface temperature distribution as a function of the inlet temperature at all radial positions is shown in Fig. 35(a). To evaluate the effect of the specific heat, similar analysis to that discussed in the heat flux effect was used. However, the average initially recorded temperature (\bar{T}_0), estimated as $\bar{T}_{0,avg}$, varied based on the inlet temperature. Upon iteration and comparison, the average surface temperature change as a function of the specific heat accounted for approximately $55\pm 5\%$ of the experimental average surface temperature change. Although the estimation suggest other contributions from varying factors, more than half of experimental values was governed by the specific heat of the fluid. Other parameters, such as the thermal conductivity, which influences the temperature profile can make up the other contribution to the surface temperature distribution. As shown in Fig. 35(b), the local *HTC* closest to the stagnation zone first increased with inlet temperature until peaking at an inlet temperature of 28.2 °C and then gradually declined. The *HTC* in the other two measured locations were not as significantly affected by the inlet temperature. The local *HTCs* range were approximately 30,000 W/m².K, 8,000 W/m².K and 2,000 W/m².K with increasing the radial positions.

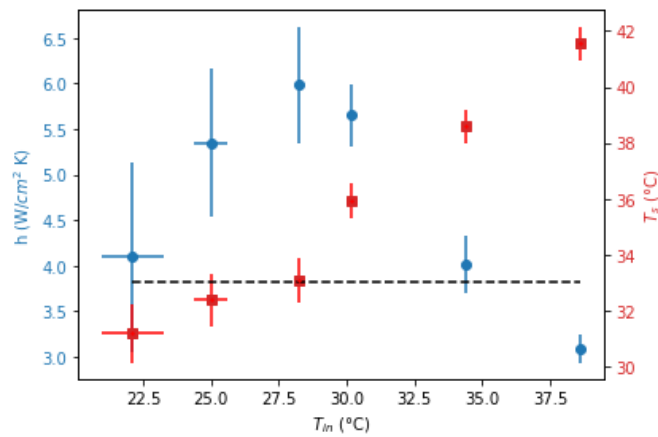
Figure 35(c) shows that the highest local *HTC* was recorded at the stagnation region at an inlet temperature of 28.2 °C, corresponding to a surface temperature slightly above the pseudocritical temperature. As discussed earlier, the thermophysical properties of sCO₂ affected the *HTC*, with a greater influence from the high specific heat attained around the pseudocritical region. Local *HTC* and surface temperature comparison for $r/d = 1.44$ and 2.89 were not shown as their local surface temperatures were always higher than the pseudocritical temperature at the inlet conditions used for this investigation. For this reason, the *HTC* were not greatly influenced by an increase in the inlet temperature. Chen et al [107] reported a higher *HTC* when the inlet

temperature was slightly lower than the pseudocritical temperature near the stagnation region for macro jet, and Joo-Kyun and Toshio [108] reported that the heat transfer was enhanced when the inlet temperature was close to the pseudocritical conditions for axisymmetric laminar jet.



(a)

(b)



(c)

Figure 35: (a) Local surface temperature as a function of inlet temperature, (b) Local heat transfer coefficient as a function of inlet temperature (c) Local heat transfer coefficient and surface temperature as a function of inlet temperature at RTD1. All sub-fig

3.2.4. Comparison To Available Correlations

A number of empirical correlations have been proposed and considerable work has been done to model the heat transfer characteristics under a single impinging jet. Several of these correlations were compared to the experimental results reported here as shown in Fig. 12 and Table 3. Although in the Martin's correlation [39], the r/d range falls above this used in the current study, comparison was still made as several studies reported a similar trend in micro and macro scale correlations [103]. Hoffmann [111] further extended Martin's [39] work for a range of micro and macro jets and proposed a local and area averaged Nusselt number correlations.

Predictions by Wen and Jang [112] and Tawfek [113] were much above the experimental values. The area average Nusselt number correlations of Martin and Hoffman overlapped with each other, as Hoffman's work was an extension of Martin's for a wider range of r/d . These correlations offered closest prediction to the experiment with that of Martin's much closer at higher Reynolds number. Goldstein and Behbahani [114] proposed an average Nusselt number correlation for a single round jet for two L/d . Although the L/d for the current study fell outside the range of the correlation, that for $L/d = 6$ was closer to the experiment at lower Reynolds number, but gradually deviated at higher Reynolds number. In sum, most correlations over predicted the experiments except for Goldstein and Behbahani [114] and Choo et al. [30] correlations.

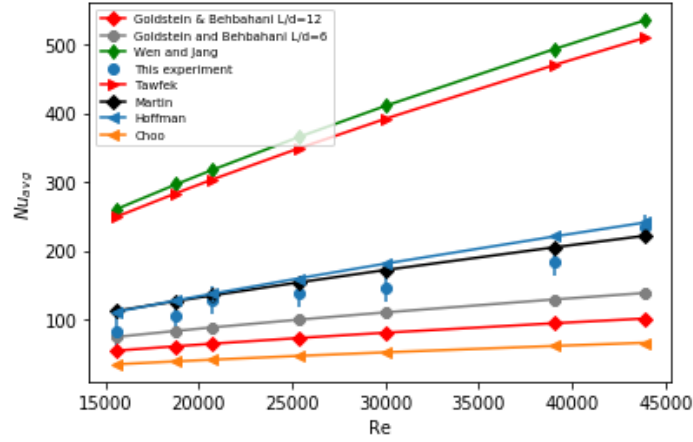


Figure 36: Comparison to available correlations

Table 4: Available Nusselt correlations for jet impingement

Source	Correlation	Range	MAE (%)
Martin [39]	$Nu_{avg} = Pr^{0.42} \frac{d}{r} \frac{1 - 1.1 d/r}{1 + 0.1(L/d - 6) d/r} F(Re)$ $F(Re) = 2Re^{0.5} \left(1 + \frac{Re^{0.55}}{200} \right)^{0.5}$	$2,000 \leq Re \leq 400,000$ $2.5 \leq r/d \leq 7.5$ $2 \leq L/d \leq 12$	19.19
Hoffman [111]	$Nu_{avg} = Pr^{0.42} [Re^3 + 10Re^2]^{0.25} \frac{1 - e^{-0.025(\frac{r}{d})^2}}{0.025(r/d)^2}$	$3,000 < Re < 210,000$ $0.5 < \frac{L}{d} < 40$ $0 < \frac{r}{d} < 70$	23.37

Goldstein and Behbahan i [114]	$\text{for } L/d = 6, Nu_{avg} = \frac{Re^{0.6}}{[3.329 + 0.273(r/d)^{1.3}]}$ $\text{for } L/d = 12, Nu_{avg} = \frac{Re^{0.6}}{[4.577 + 0.4357(r/d)^{1.14}]}$	$34,000 \leq Re \leq 121,300$ $0.5 < \frac{r}{d} < 32$	41.24 69.41
Tawfek [113]	$Nu_{avg} = 0.453Pr^{\frac{1}{3}}Re^{0.691} \left(\frac{L}{d}\right)^{-0.22} \left(\frac{r}{d}\right)^{-0.38}$	$3,400 < Re < 41,000$ $6 < \frac{L}{d} < 58$ $2 < \frac{r}{d} < 30$	220.4 4
Wen and Jang [112]	$Nu_{avg} = 0.442Pr^{1/3}Re^{0.696} \left(\frac{L}{d}\right)^{-0.20} \left(\frac{r}{d}\right)^{-0.41}$	$750 < Re < 27,000$ $3 < \frac{L}{d} < 16$ $0 < \frac{r}{d} < 7.14$	237.8 5
Choo et al [30]	$Nu_{avg} = 1.07 \times 10^{-5} Re^{m_2} (L/d)^{4.5}$ $m_2 = 2.015 - 0.294 \left(\frac{L}{d}\right) + 0.0142(L/d)^2$	$2500 < Re < 5000$ $\frac{L}{d} = 2, 3, 5 \text{ and } 10$	96.67

3.2.5. New Correlations

A number of correlations have been proposed following the experimental data to better quantify and predict important parameters while working with CO₂ either in its super critical state condition. Following the dependency of the HTC on the heat flux while operating with sCO₂ and

more importantly the heat flux magnitude where the maximum HTC is achieved, a pseudocritical heat flux (q''_{pc}) was defined as the heat flux needed to bring the surface temperature slightly above the pseudocritical temperature of the fluid. This heat flux took the form

$$q''_{pc} = 1.62T_{pc} - 23.39exp^{T_{pc}/80.04} \text{ W/cm}^2 \quad (22)$$

for an inlet pressure of 7.45 MPa, mass flux of 0.53 kg/cm²s, and inlet temperature of 21 °C. (Note that p is the pressure in bar). T_{pc} is the fluid's pseudocritical temperature. In dimensionless form:

$$\zeta = \frac{q''}{q''_{pc}} = \frac{1.62T_{s,avg} - 23.39exp^{T_{s,avg}/80.04}}{1.62T_{pc} - 23.39exp^{T_{pc}/80.04}} \quad (23)$$

$$0 \leq \zeta \leq 5.5$$

As shown in Fig. 37, the maximum *HTC* was expected when

$$1 < \zeta \leq 1.1$$

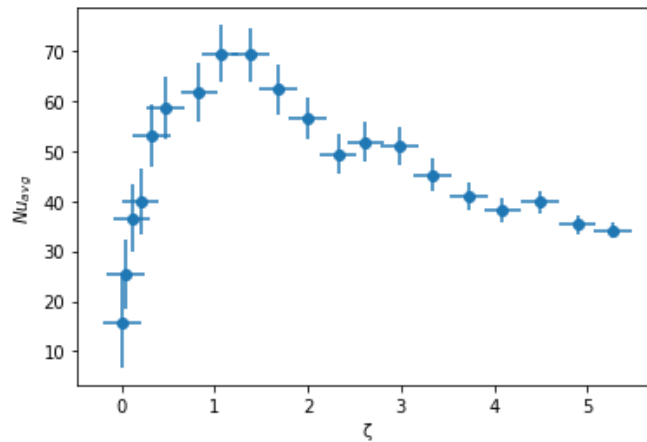


Figure 37: Area-averaged Nusselt vs dimensionless heat flux

Likewise, the power needed to bring the surface temperature slightly above the pseudocritical temperature termed the pseudocritical power was estimated as

$$P_{cp} = A_H \left(1.62T_{pc} - 23.39exp^{T_{pc}/80.04} - q''_{loss} \right) W. \quad (24)$$

for an inlet pressure of 7.45 MPa, a mass flux of 0.53 kg/cm² s, and inlet temperature of 21 °C. A_h is the area of the heater.

The available correlations detailed above appeared to predict the experimental results with a limited degree of success. In addition, the importance of the heat flux, or dimensionless heat flux (ζ), on the area-averaged HTC/Nu appeared to be significant in this study but is unaccounted in available correlations. Thus, a new correlation was proposed for the area averaged Nusselt number. The proposed area averaged Nusselt number introduced the dimensionless heat flux. The standoff dependency ($Nu \propto L/d$) was not accounted for as it was constant in this study. The dependency on the dimensionless heat flux ($Nu_{avg} \propto \zeta$) was fitted with a fourth-degree polynomial as shown in Fig. 38(a) yielding an MAE of approximately 3.08%. Likewise, its dependency on the Reynolds number was also fitted with a curve as shown in Fig. 38(b) with a MAE of approximately 11.10%. A Prandtl number dependency of $Nu \propto Pr^{0.42}$ was used following the recommendation by Shi et al [115]. The new resulting Nusselt number correlation proposed takes the form

$$Nu_{avg} = 0.02Pr^{0.42}(r/d)^{-1.59}Re^{0.61}(-1.2\zeta^4 + 14.98\zeta^3 - 63.53\zeta^2 + 95.56\zeta + 22.25)^{0.94} \quad (25)$$

valid for:

$$15,500 \leq Re \leq 44,000$$

$$0.21 \leq r/d \leq 2.89$$

$$0 \leq \zeta \leq 5.5$$

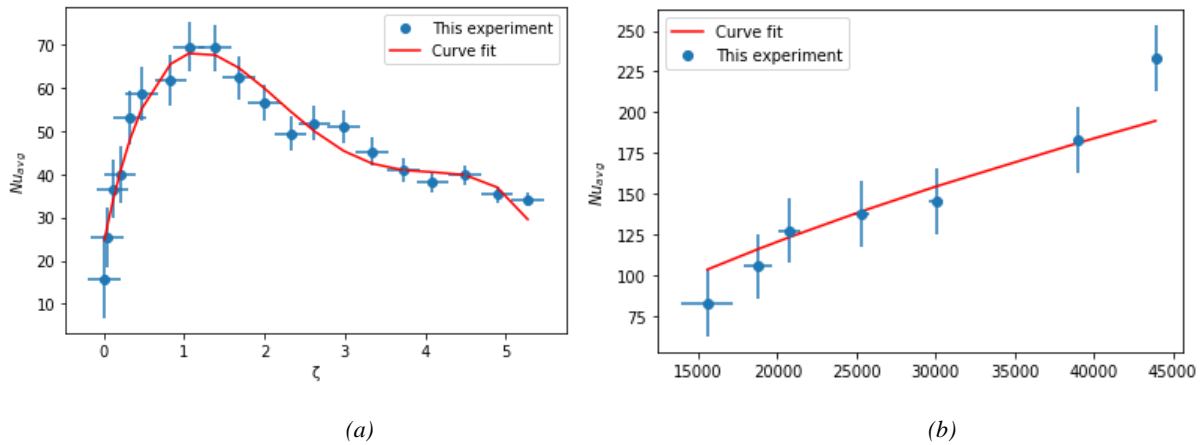


Figure 38: Curve fitting (a) varying dimensionless heat flux (b) Varying Reynolds number

3.3. Conclusion

Major results from this investigation are summarized below:

- The local HTC increased until reaching a peak and then decreased drastically with increasing heat flux. The maximum local HTC were recorded when the corresponding local surface temperature was around the pseudocritical temperature.
- The peaks in both local and area averaged HTC were quantified in respect to the effect of the specific heat of sCO_2 at the pseudocritical region.
- Increasing the mass flux, increased the local and averaged HTC .
- The effect of mass flux undermined the specific heat effect as the HTC increased regardless of the surface temperature distribution below or above the pseudocritical region.

- The local HTC at the stagnation region first increased and then decreased with increasing inlet temperature, while those farther from the stagnation region showed no significant change with increasing inlet temperature. The maximum local *HTC* at the stagnation region (*RTD₁*) was recorded when the inlet temperature was slightly lower than the pseudocritical temperature, which corresponded to a local surface temperature slightly higher than the pseudocritical temperature. Insignificant variations were observed in *RTD₂* and *RTD₃* as their local surface temperatures were already above the pseudocritical temperature.

- The local surface temperature distribution over the heater were sensitive to the inlet temperature at all *RTDs*.

- Available correlations did not take into account the effect of heat flux, which is a significant parameter controlling the Nusselt number. Likewise, most of the correlations over predicted the area-averaged Nusselt number, thus, a new correlation was proposed.

Conclusively, we were able to experimentally investigate the heat transfer properties of *sCO₂* in a microjet impingement with optimum working condition around the pseudocritical temperature or the maximum design flow rate.

CHAPTER FOUR: FLOW BOILING OF CARBON DIOXIDE IN A SINGLE JET IMPINGEMENT

The contents of this chapter have been published in:

Adeoye, S. and Y. Peles, Flow boiling of carbon dioxide with a micro impinging jet. International Journal of Heat and Mass Transfer, 2022. 187: p. 122495. [101]

4.1. Introduction

As stated above, the utilization of jet impingement at the micro scale has attracted considerable interest and has been proven to be an effective cooling method, mostly as a result of the enhanced disturbance generated within the cooling medium when compared to its traditional counterpart. In addition, the transition from single-phase to two-phase cooling offers additional heat transfer enhancement owing to varying factors, such as nucleate boiling, bubble generation and collapse that control the flow distribution of the fluid within the cooling medium. Likewise, CO₂ can serve as a good replacement for convective working fluids owing to its properties in its two-phase conditions, and other associated two-phase flow phenomena. Many other studies have proven a notable enhancement in the heat transfer capabilities of flow boiling over single-phase conditions for varying working fluids such as water [116, 117], R134a and HFE-7000 [118], however, a few papers have been dedicated to the utilization of CO₂. More importantly, the need to replace or improve on present conventional cooling methods to meet the ever-growing transistor counts in a dense integrated circuit according to Moore's law [1] sets up a trademark, suggesting

that the utilization CO₂ in its two-phase condition in a micro-scaled impinging jet can significantly enhance the heat transfer abilities, ultimately offering a more effective and efficient cooling approach. Thus, this chapter discussed the experimental investigation of the heat transfer and flow characteristics of CO₂ in its two-phase condition within a single micro impinging jet geometry, by varying susceptible heat-transfer-governance, such as the radial position, heat flux, mass flux and pressure. Finally, the heat transfer behavior was compared with available correlations and a new critical heat flux correlation was proposed.

4.2. Results And Discussion

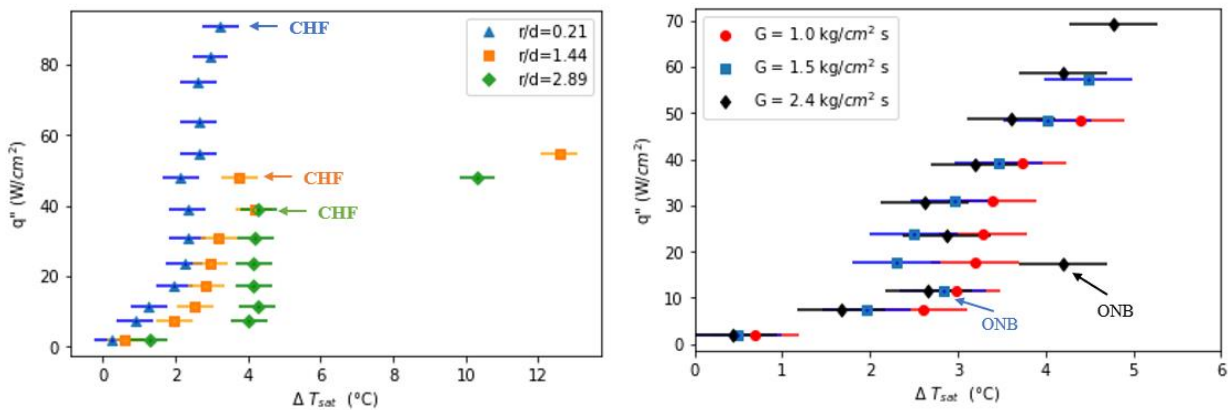
Susceptible heat transfer governance such as the radial position, heat flux, mass flux and inlet temperatures were experimentally studied to understand their influences of the heat transfer rate of sCO₂. The range of operations is illustrated in Table 5 with the results discussed in the preceding section.

Table 5: Experimental Inlet conditions

Parameter	Range
Radial position (r/d)	0.21, 1.44, and 2.89
Heat flux ($W/cm^2 K$)	0 ~ 140
Mass flux ($kg/cm^2 s$)	0.7 ~ 2.4
Pressure (MPa)	5.3, 5.9, and 6.7
Mass quality	0 ~ 1

4.2.1. Boiling Curve

The boiling curves for most of the experiments performed in this study are depicted in Fig. 5. Although no clear indication of the flow visualization is shown in this study, the *ONB* observed through the boiling curves suggests that flow boiling of the CO_2 occurred close to the inlet after a small heat flux ($< 7.4 \text{ W/cm}^2 \text{ K}$) was generated from the heater as a result of the fluid's inlet thermodynamic properties corresponding approximately to its saturation condition. The slope, which is directly related to the heat transfer coefficient, and the critical heat flux depended on the radial position, heat flux (for the *HTC*), mass flux, and saturation temperature. (Note that Figs. 5(b) and 5(c) were inferred from the area-averaged ΔT_{sat}). For low mass fluxes, such as for $G = 1.0 \text{ kg/cm}^2\text{s}$, *ONB* was assumed to have started rapidly at the inlet due to the presence of a thicker boundary layer leading to a warmer fluid near the wall, and thus, necessitating less heat to initiate boiling. Some temperature overshoot was observed at the higher two mass fluxes ($G = 1.5 \text{ kg/cm}^2\text{s}$ and $2.4 \text{ kg/cm}^2\text{s}$) before *ONB*.



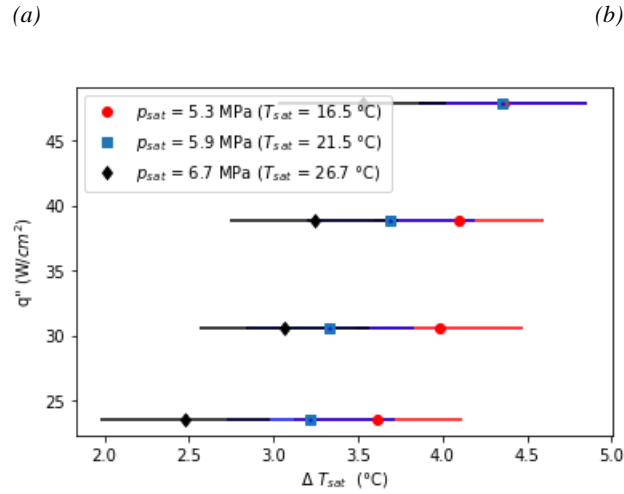


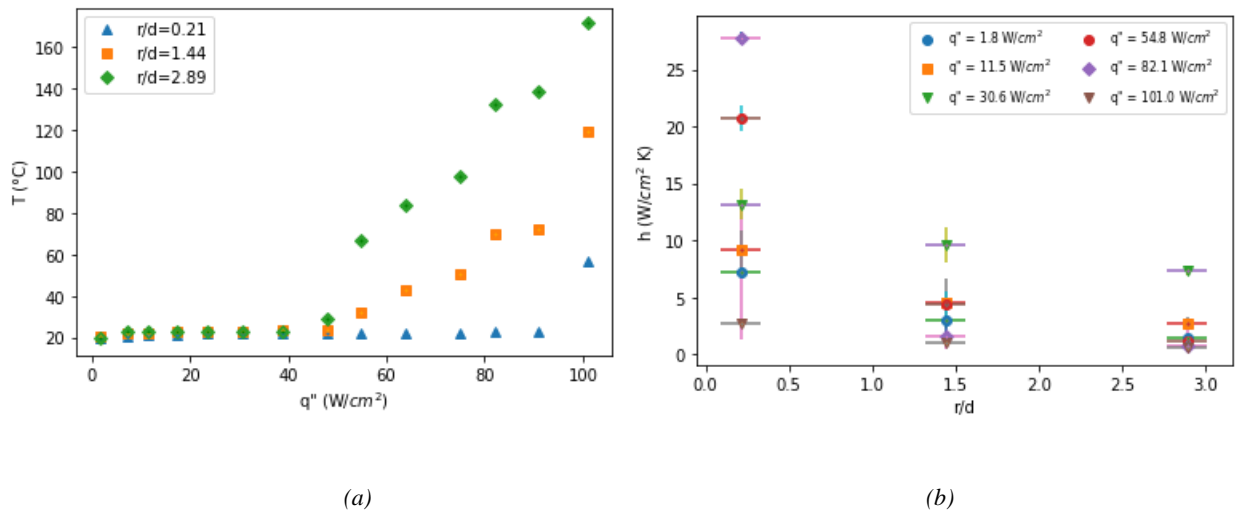
Figure 39: Boiling curves – (a) radial position effect ($T_{in}=21.2\text{ }^{\circ}\text{C}$, $T_{sat} = 21.5\text{ }^{\circ}\text{C}$, $G= 1.0\text{ kg/cm}^2\text{s}$); (b) mass flux effect ($T_{in}=21.2\text{ }^{\circ}\text{C}$, $T_{sat} = 21.5\text{ }^{\circ}\text{C}$, $r_{avg} = 0.4$); (c) pressure effect ($G= 1.0\text{ kg/cm}^2\text{s}$, $r_{avg} = 0.4$)

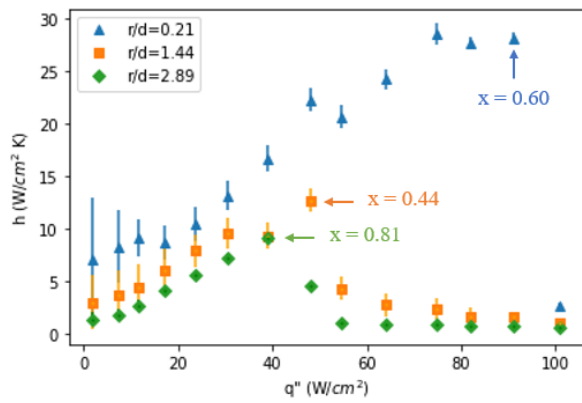
4.2.2. Heat Flux and Radial Position Effect

Here the heat flux varied from 0 ~ 100 W/cm² at an inlet temperature of 21.2 °C and a saturation temperature (T_{sat}) of 21.5 °C, corresponding to an inlet saturation pressure (P_{sat}) of ~5.9 MPa, and a mass flux of 1.0 kg/cm² s. Figure 40(a) depicts the surface temperature as a function of radial position and heat flux. The increase in the local surface temperature was incremental with increasing heat flux at all radial positions before abruptly increasing above heat fluxes of 74.8 W/cm², 47.4 W/cm², 38.9 W/cm² with respect to RTD₁, RTD₂ and RTD₃, respectively. The local HTC decreased radially at selected heat fluxes as seen in Fig 6(b). For single-phase flow, this is associated with the influence of the jet hydrodynamics for which a more pronounced impingement effect at the stagnation region is present. For flow boiling an additional factor is triggered that is associated with the liquid-to-vapor phase change process pre- CHF that can be dominated by nucleate boiling or convective boiling. If the inlet enthalpy is insufficient for ONB at the stagnation

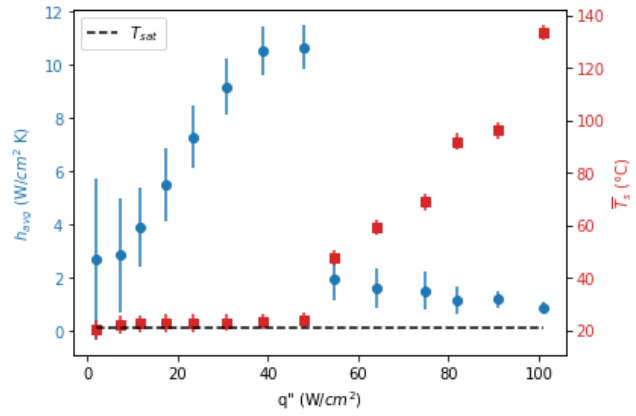
zone, but sufficiently high for boiling inception at the wall jet region, it is conceivable that the HTC will increase downstream. However, this was not observed in this study primarily because the hydrodynamic effect of the impingement jet overshadowed the liquid to vapor phase change effect leading to a decline in the local HTC with increasing radial position.

The local and area-averaged HTC as, respectively, depicted in Fig. 40(c) and 40(d) were significantly increased with heat flux to a peak before a drastic decline is observed. Such dependency has always been attributed to the dominance of nucleate boiling. However, the transition from nucleate boiling to convective is expected to occur at lower mass qualities than those observed here. Since in this study the increase in the heat flux was also associated with increase in mass quality, the transition from nucleate boiling to convective boiling probably occurred at lower mass quality than those observed in the peaks ($x = 0.44$ to 0.81) shown in Fig.40(c). Thus, the sharp drop in the HTC , which suggests the arrival of a CHF condition, occurred during convective boiling and is a result of dry-out.





(c)



(d)

Figure 40: Effect of radial position and heat flux at $x_{in}=0.002$. (a) local surface temperature distribution vs. heat flux. (b) local HTC vs. dimensionless radial position at selected heat fluxes. (c) local HTC vs. heat flux. (d) average local surface temperature

Chen et al. [30] reported similar results with flow visualization showing how the boiling area propagated from the wall jet to the stagnation region in their study of jet impingement boiling cooling with CO₂. Other studies [20, 37, 42, 43] also reported a similar trend in the HTC with the heat flux regardless of the working fluid and/or cooling geometry. The CHF are also dependent on the radial position as earlier depicted in Fig 5(a) and Fig. 6(c). The CHF is expected to start at the exit and gradually propagate upstream with increasing heat flux as a result of a higher mass quality downstream, thus, the CHF decrease with increasing radial position.

4.2.3. Mass Flux Effect

A heat flux of 47.93 W/cm^2 K was set constant while the mass flux varied from $0.7 \text{ kg/cm}^2\text{s}$ to $1.6 \text{ kg/cm}^2\text{s}$ at an inlet temperature of $21.2 \text{ }^\circ\text{C}$ and a pressure of $\sim 5.9 \text{ MPa}$. The superheat temperature decreased for all RTD locations with mass flux, as shown in Fig. 41(a), suggesting that convective boiling, together with nucleate boiling, was also an important mechanism controlling the heat transfer process. However, locations at or closer to the stagnation region were usually more influenced by the mass flux. For example, the differences between the maximum and minimum superheat temperatures were approximately $3.1 \text{ }^\circ\text{C}$, $2.0 \text{ }^\circ\text{C}$ and $1.0 \text{ }^\circ\text{C}$ with radial positions. In the position furthest away from the stagnation zone (i.e., at RTD_3) the HTC was only increased by approximately 24% from $G = 0.7 \text{ kg/cm}^2\text{s}$ to $G = 1.6 \text{ kg/cm}^2\text{s}$, as compared to an approximate 74 % and 169 % for RTD_2 and RTD_1 , respectively. The area-averaged HTC increased by 65.1 % between $G = 0.7 \text{ kg/cm}^2\text{s}$ and $G = 1.6 \text{ kg/cm}^2\text{s}$. The larger increase in the HTC near the stagnation zone suggests that in this region, although the mass quality was the lowest ($x_r=0.39$), convective boiling effects were significant. This is perhaps because the flow in all RTD locations already transitioned to convective boiling and the stagnation zone was more sensitive to mass flux. Nusselt number correlations for single-phase flow typically separate the stagnation region from the wall jet region [55, 119]. According to Womac et al. [55], the single-phase Nusselt number in the stagnation zone is typically a function of $Re^{0.5}$ while in the wall jet region it is slightly more dependent on the Reynolds number ($Re^{0.532}$), which seems to contradict the trend observed here. It is being reported from chapter 3 that there exist a significant sensitivity of the HTC to mass flux especially in the stagnation region with an estimated average Reynolds number dependency of

0.61; this could be attributed to the increase in the local *HTC* with mass flux at RTD_1 as observed in this experiment.

It should be noted that conflicting results pertinent to the effect of the mass flux on the boiling curves have been reported before. Zhou and Ma [49] reported little effect of jet velocity on submerged jet boiling heat transfer. Similarly, Cardenas and Narayanan [120] reported that jet velocity doesn't affect the boiling curve but influences the *CHF*. These reports have been attributed to fully developed region where the hydrodynamics of the fluid is not apparent and the major factor governing the heat transfer is the bubble ebullition process. Chen et al. [121] also reported that the mass flux effect on the heat transfer coefficient disappeared when the flow transitioned from single-phase to two-phase. However, other studies, such as [41, 44], reported a significant effect of the mass flux on both the boiling curve in fully developed region as well as a greater influence on the *CHF* and *ONB* in the nucleate boiling regimes — these studies reported an overall better heat transfer performance with increasing mass flux. Nonetheless, this study reports a significant effect of the mass flux on the *HTC*.

To identify the *CHF* conditions, the area-averaged *HTC* was examined while varying the heat flux to identify a notable drastic surface temperature increase at selected mass flux. Three mass fluxes of 1.0 kg/cm²s, 1.5 kg/cm²s and 2.4 kg/cm²s were examined over a heat flux from 0 up to 140 W/cm². As depicted in Fig. 41(d), while the *CHF* increased with mass flux, the area-averaged *HTC* only increased pre-*CHF* condition and the mass flux effect diminished after transition. Likewise, most of the increase in the area-averaged *HTC* might be due to the increased heat flux suggesting an overall reduced sensitivity of the *HTC* to the mass flux for flow boiling process.

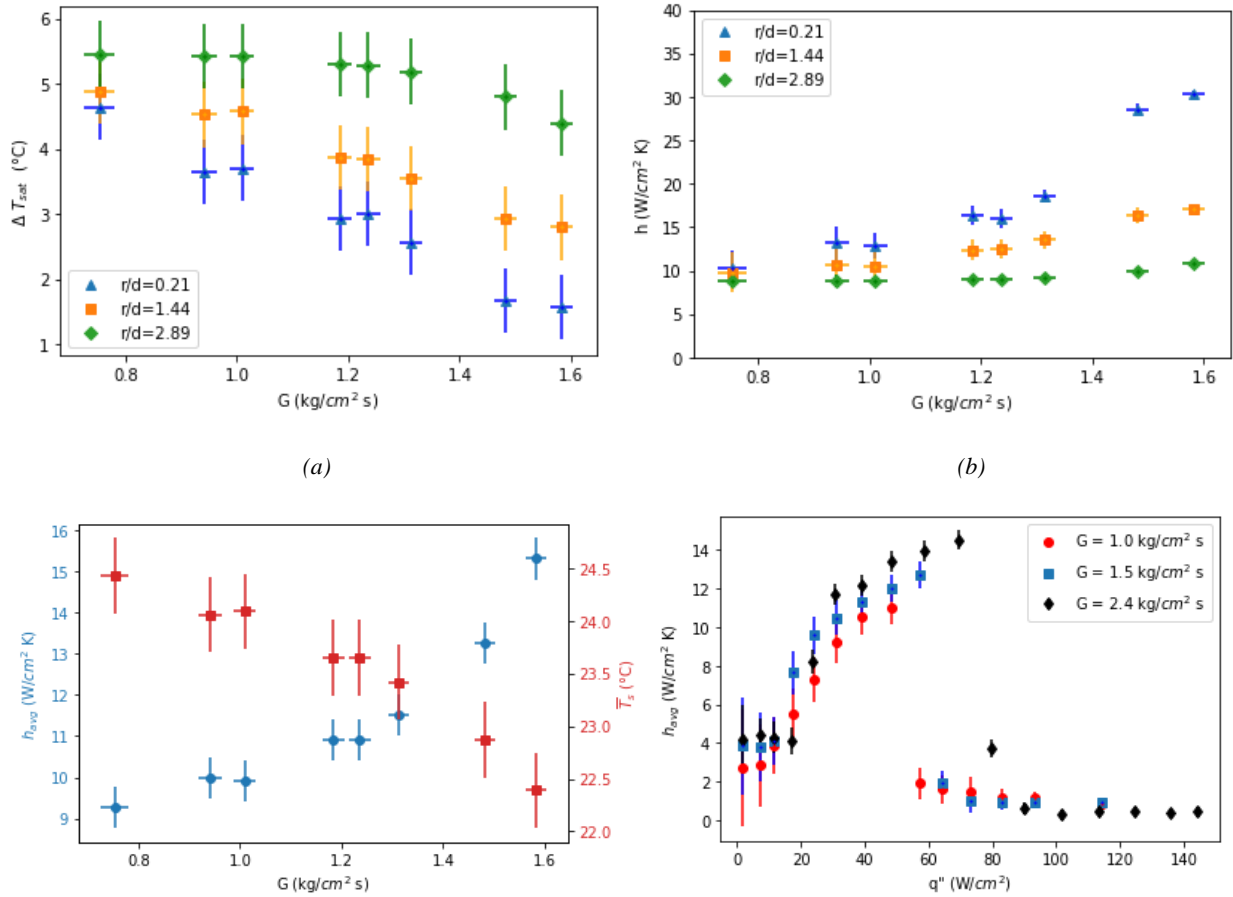


Figure 41: Mass flux effect on flow boiling of CO₂. (a) local superheat temperature vs. mass flux (b) local HTC vs. mass flux (c) area-averaged HTC vs. mass flux and surface temperature. ($T_{in} = 21.2$ °C, $p_{sat} = 5.9$ MPa, $q'' = 47.93$ W/cm²K) (d) Mass flux effect on HTC of flow boiling of CO₂ at varying heat fluxes

4.2.4. Pressure Effect

Pressure effect was examined for pressure ranging from 5.3 to 6.7 MPa, corresponding to saturation temperatures of 16.5 °C to 26.7 °C from a vapor quality of 0.3 ~ 1.0 over a heat flux of 7.4 ~ 100 W/cm² and a constant mass flux of 1.0 kg/cm²s (Fig 39(c)). A shift in the boiling curve to the left with pressure (i.e., saturation temperature) is notable, depicting a significant dependency

of the curve slope (i.e., the *HTC*) on the pressure. Figure 42 shows the area-averaged *HTC* as a function of the averaged exit vapor quality (\bar{x}_{out}) for the three pressures. The area-averaged *HTC* mostly increased with pressure at low qualities pre-CHF and post-CHF conditions. This increase at low mass qualities was a result of a more rigorous bubble ebullition process at the liquid sub-layer region with increasing pressure. In a cooling geometry different from a jet impingement, Choi et al. [122] observed similar trend in the *HTC* with pressure at low mass qualities, attributing it to an enhanced activation of nucleate boiling. Likewise, several other studies [93, 123] about the effect of reduced pressure on the *HTC* in nucleate boiling suggested a pressure-*HTC* correlation for CO₂ where the intensity of the nucleate boiling is highly dependent on the fluid pressure. The increase in the *HTC* with pressure could also be attributed to the liquid to vapor density ratio, which decreased as the saturation temperature (i.e., pressure) increased. As suggested by Yun [124], the increase in the *HTC* could also be attributed to a decrease in surface tension with saturation temperature supporting a more consistent and rigorous bubble ebullition process with the associate enhanced heat transfer.

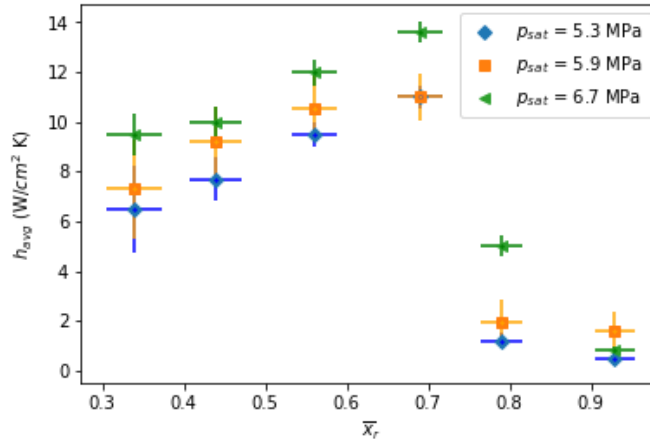


Figure 42: Area-averaged HTC for three pressures as a function of averaged exit vapor quality. ($q'' = 7.4 \sim 100 \text{ W/cm}^2$, $G = 1.0 \text{ kg/cm}^2 \text{ s}$)

4.2.5. Comparison To Available Correlations

Table 6 lists several CHF correlations for jet impingement boiling that considered the jet velocity (u), liquid density (ρ_f), vapor density (ρ_g), surface tension (σ), nozzle diameter (d), distance of the orifice from the heater (i.e., standoff), and/or the heater diameter (d_H). Most of these correlations were derived from experimental studies of water and refrigerants, such as R12 and R113. These correlations were compared to the experimental data, as depicted in Fig. 43, where the heater's length from [125, 126] was approximated as the heater diameter. Most of the correlations over-predicted the experimental data except for Katto and Ishii [126], which underpredicted the data with a MAE of -47.43%. These discrepancies could be because of the fluid thermal properties and/or the jet velocity range being used in developing the correlations. While the correlation by Katto and Ishii [126] underpredicted the experimental data, it also offered the closest MAE.

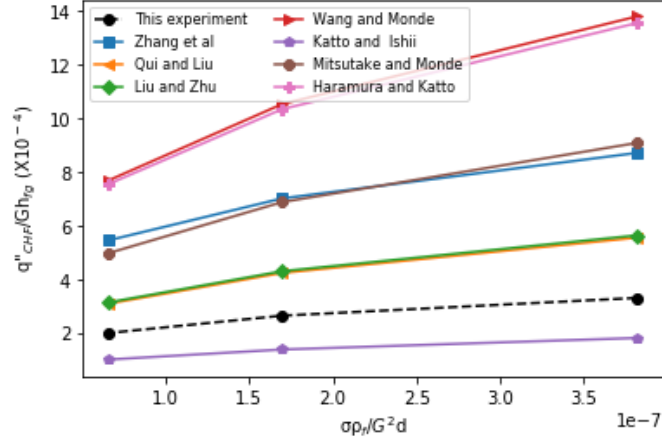


Figure 43: Comparison to available correlations

Table 6: Available CHF correlations

Source	Correlation	MAE (%)
Zhang et al [27]	$\frac{q''_{CHF}}{Gh_{fg}} = 0.16 \left(\frac{\rho_g}{\rho_f} \right)^{0.399} \left(\frac{2\sigma\rho_f}{G^2 d} \right)^{0.267} \left(1 + \frac{L}{d} \right)^{-0.44}$	167.23
Qui and Liu [47]	$\frac{q''_{CHF}}{Gh_{fg}} = 0.130 \left(1 + \frac{\rho_g}{\rho_f} \right)^{1/3} \left(\frac{\sigma\rho_f}{G^2 d} \right)^{1/3} \left(\frac{\rho_g}{\rho_f} \right)^{1.4/3}$	60.88
Liu and Zhu [99]	$\frac{q''_{CHF}}{Gh_{fg}} = 0.132 \left(1 + \frac{\rho_g}{\rho_f} \right)^{1/3} \left(\frac{\sigma\rho_f}{G^2 d} \right)^{1/3} \left(\frac{\rho_g}{\rho_f} \right)^{1.4/3}$	63.36
Haramura and Katto [127]	$\frac{q''_{CHF}}{Gh_{fg}} = 0.175 \left(\frac{\rho_f}{\rho_g} \right)^{0.533} \left(\frac{\sigma\rho_f}{G^2 d_H} \right)^{1/3} \left(1 + \frac{\rho_g}{\rho_f} \right)^{1/3}$	292.67

Wang and Monde [125]	$\frac{q''_{CHF}}{Gh_{fg}} = 0.193 \left(\frac{\rho_f}{\rho_g} \right)^{0.533} \left(\frac{\sigma \rho_f}{G^2 L} \right)^{1/3}$	299.92
Katto and Ishii [126]	$\frac{q''_{CHF}}{Gh_{fg}} = 0.0164 \left(\frac{\rho_f}{\rho_g} \right)^{0.867} \left(\frac{\sigma \rho_f}{G^2 L} \right)^{1/3}$	-47.43
Mitustake and Monde [128]	$\frac{q''_{CHF}}{Gh_{fg}} = 0.221 \left(1 + \frac{\rho_f}{\rho_g} \right)^{0.645} \left(\frac{2\sigma \rho_f}{G^2 (d_H - d)} \right)^{0.343} \left(1 + \frac{d_H}{d} \right)^{-0.364}$	161.09

4.2.6. New Correlations

Several boiling studies [45, 111] correlated the heat flux as:

$$q'' = C_1 \Delta T_{sat}^m \quad (26)$$

and the area-average *HTC* as:

$$h_{avg} = C_2 \Delta T_{sat}^n \quad (27)$$

where ΔT_{sat} is the average superheated surface temperature ($\overline{T_{s,l}} - T_{sat}$). The coefficients C_1 , C_2 , and m are predicted by curve fitting experimental data. This type of correlation was used in the current study up until the *CHF* condition and yielded the following relation:

$$q'' = 0.81 \Delta T_{sat}^{2.81} \quad (28)$$

where q'' is in W/cm^2 and ΔT_{sat} is in $^\circ\text{C}$ (or K). This correlation is valid for a ΔT_{sat} range of

$$2.5 \text{ } ^\circ\text{C} < \Delta T_{sat} < 4.5 \text{ } ^\circ\text{C}$$

In comparison, Wolf et al. [45] reported a C_1 of 0.00637 and an m of 2.95 within a surface superheat temperature of $23\text{ }^\circ\text{C} < \Delta T_{sat} < 51\text{ }^\circ\text{C}$. Figure 44 show the correlations up until the *CHF* condition along with the experimental data.

A correlation for the area-averaged *HTC* was also obtained by a least square fit according to:

$$h_{avg} = 0.75q''^{0.71} \quad (29)$$

where h_{avg} is in $\text{W}/\text{cm}^2\cdot\text{K}$ and q'' is in W/cm^2 . This equation is valid for

$$7.4\text{ W}/\text{cm}^2 \leq q'' \leq 48\text{ W}/\text{cm}^2$$

For comparison, Wolf et al. [45] also reported a value of 0.052 for C_2 and an n value of 0.87 for a heat flux range of $100 < q'' < 640\text{ W}/\text{cm}^2$.

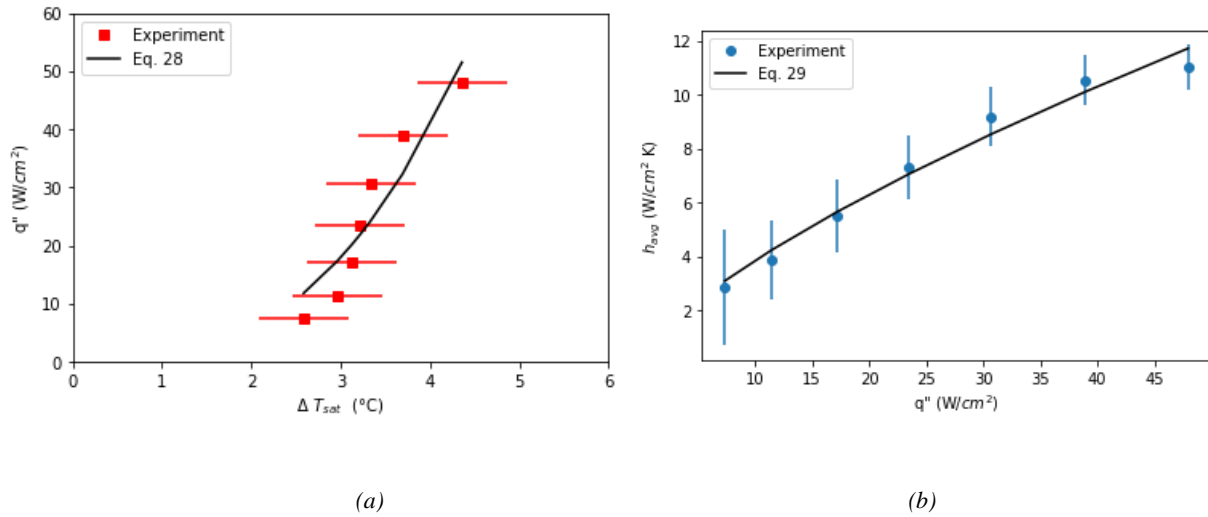


Figure 44: Correlation for nucleate boiling regime; (a) $q'' \propto \Delta T_{sat}$, (b) $h_{avg} \propto q''$ ($T_{sat} = 21.5\text{ }^\circ\text{C}$, $p_{sat} = 5.9\text{ MPa}$, $G = 1.0\text{ kg}/\text{cm}^2\text{ s}$, $ra_{vg} = 0.4$)

As a result of the discrepancies with available correlations, a new correlation for a dimensionless *CHF* for flow boiling of CO₂ in a micro jet impingement was developed. As suggested by [27, 50, 52, 53], this correlation took the following dimensionless form:

$$\frac{q''_{CHF}}{Gh_{fg}} = f\left(\left(\frac{\rho_f}{\rho_g}\right), \left(\frac{\sigma\rho_f}{G^2d}\right)\right) \quad (30)$$

Similar to [27,50-53], an exponent of 1/3 for the reciprocal of the Weber number ($\sigma\rho_f/G^2d$) was adopted to yield the following *CHF* correlation:

$$\frac{q''_{CHF}}{Gh_{fg}} = 0.22\left(\frac{\rho_f}{\rho_g}\right)^{0.57}\left(\frac{\sigma\rho_f}{G^2d}\right)^{1/3} \quad (31)$$

The coefficients 0.22 and 0.57 for the density ratio (ρ_f/ρ_g) were recorded from curve fitting with the experimental data. The dependency on the heater dimension was neglected as the values were fixed in this experiment. The new *CHF* equation correlates the experimental data with a MAE of $\pm 1.4\%$ as seen in Fig 45.

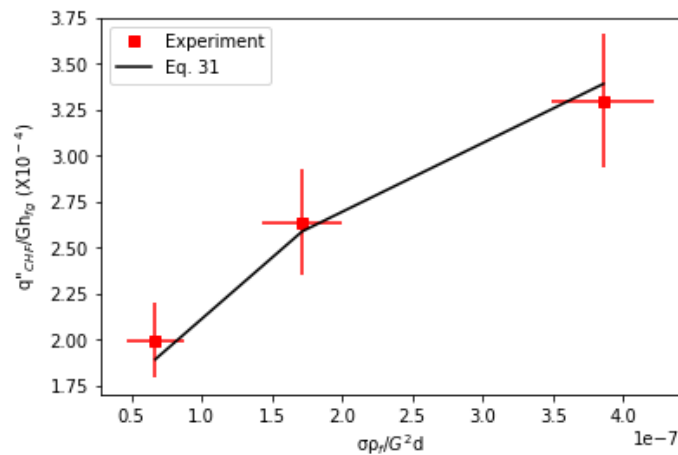


Figure 45: New *CHF* correlation vs experimental data

4.2.7. Comparison to single-phase

Fig 46 shows the the area-averaged HTC observed in a single phase (sCO₂) and two-phase (flow boiling) at a mass flux of 1.0 kg/cm² over a heat flux of 0 ~ 100 W/cm² and an inlet temperature of 21.2 °C. The aim of this investigation was to further support the flow boiling's enhacemnt on the heat transfer performace of CO₂. As observed, there is a singifacnt increase (~283 %) in the area-averaged HTC while operating in the two phase condition mostly at the nucleate boiling regime. The ONB began rapilly as a result of the inlet conditions almost simiar to the saturation conditions of the fluid at a pressure ~ 5.9 MPa. The increase in the area-averaged HTC with increasing heat flux is as a result of the activation of more nucleate boiling sites with increasing heat flux. Correspondingly, with increasing the heat flux, it is assumed that the rate at which the bubbles are generated are higher than the detachment rate causing the heavy bubbles to collapse, and upon settling, the colder fluid from the jet is prevented from cooling the heated surface. As a consequence, this non-heated cold fluid distorts the heat transfer causing a decline in the HTC. The point where this condition begins is marked at the CHF mark on the two-phase trend which depicts the departure from the nucleatae boiling characterized by a drastic decline in the area-averaged HTC. Although flow boiling is always a better cooling process, its is usually used as the last resort in engineering applications as a result of the physical complexity and its depedncy on quite a number of parameters.

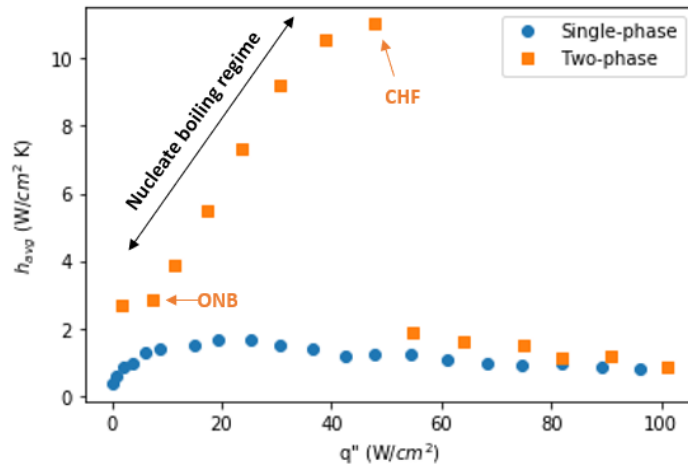


Figure 46: Comparison to single phase

4.3. Conclusion

- The boiling curves, *CHF*, and *HTC* were influenced by the radial position, heat flux, mass flux and saturation temperature;
- The local and area-averaged *HTC* increased with heat flux with ~300% increase from 0 W/m² K heat flux, up until the *CHF* was triggered due to dryout;
- The *CHF* decreased with increasing radial position as a result of an increase in the outlet mass quality;
- The *CHF* and *HTC* increased with increasing mass flux;
- The area-averaged *HTC* increased with increasing pressure mostly at low mass qualities as a result of a more rigorous bubble ebullition process;
- Flow boiling of CO₂ offered higher *HTC* of up to 283% before the *CHF* condition
- Most available correlations overpredicted the *CHF*, therefore, a new *CHF* correlation for flow boiling of CO₂ in a jet impingement with a MAE of ±1.4% was proposed.

Conclusively, we were able to experimentally investigate the heat transfer properties of CO₂ in its two-phase region in a microjet impingement with enhancement supporting the hypothesis. Likewise, a new CHF correlation was proposed for further research and industrial applications

CHAPTER FIVE: SINGLE-PHASE CO₂ IN MULTIPLE JET IMPINGEMENT

5.1. Introduction

The development of array of impinging jets resulted from the radial decrease in the heat transfer coefficient for as single jet has reported in prior chapters. In other to assume more consistent temperature distribution over the heater, the jet configuration can include a number of jets properly positioned over the heater, this configuration allows for an even spread of the jets over the heater, giving to a rise in a uniform and/or higher HTC. The advantage of this over the single jet is tied to the industrial adoption and utilization where one single jet is not enough based on the size of the heat dissipating element.

This chapter explicitly reported the experimental investigation of super critical carbon dioxide in an array of jet within a defined micro domain over varying parameters such as the heat flux, radial position, mass flux and inlet pressure. Specific comparisons were also made to the single jet counterpart (chapter 3)

5.2. Results And Discussion

Susceptible heat transfer governance such as the radial position, heat flux, mass flux and inlet pressures were experimentally studied to understand their influences of the heat transfer rate of sCO₂ in a jet array. The range of operations is illustrated in Table 8 with the results discussed in the preceding section.

Table 8: Experimental Inlet conditions

Parameter	Range
Radial position (r/d) with reference to the center jet	0.21, 1.44, and 2.89
Heat flux ($\text{W}/\text{cm}^2 \text{ K}$)	0 ~ 80
Mass flux ($\text{kg}/\text{cm}^2 \text{ s}$)	1.0 ~ 3.2
Pressure (MPa)	7.7, 8.8, and 10.3

5.2.1. Heat Flux and Radial Position Effect

The heat flux effect was investigated over a heat flux increment of 0 ~ 80 W/cm^2 , at a constant fluid pressure of 8.0 MPa – much higher than the supercritical pressure of CO_2 , an inlet temperature of 21.7 °C, and a constant mass flux of 1.1 kg/cm^2 corresponding to a Reynolds number of 40,600. Fig 47(a) depicts the surface temperature distribution as measured by the RTDs over the experimented heat flux range and the corresponding local HTC. There exists a consistent temperature distribution over the heater up until a heat flux of ~ 50 W/cm^2 . With further increase in the heat flux beyond this region, a notable deviation is observed with RTD_3 measuring the highest temperature. As shown in chapter 2, RTD_1 was totally covered by the center jet while although the spatial distribution of the other jets was concentrically positioned on RTD_2 and 3, there exists surface areas not fully covered the jets. These areas are assumed to behave like the wall jet region as observed in a single jet or represent the upwash region in a multi-jet hydrodynamics. The upwash effect is generated due to the colliding jets and the entrainment of ambient air into the flow [59]. This effect has been proven to be dependent on the interjet spacing (S/d) with its strength decreasing with an increase in the S/d . Therefore, with an interjet spacing of

1., the interactions between the neighboring jet were more pronounced degrading the convective heat transfer ability of the fluid with further increase in the heat flux.

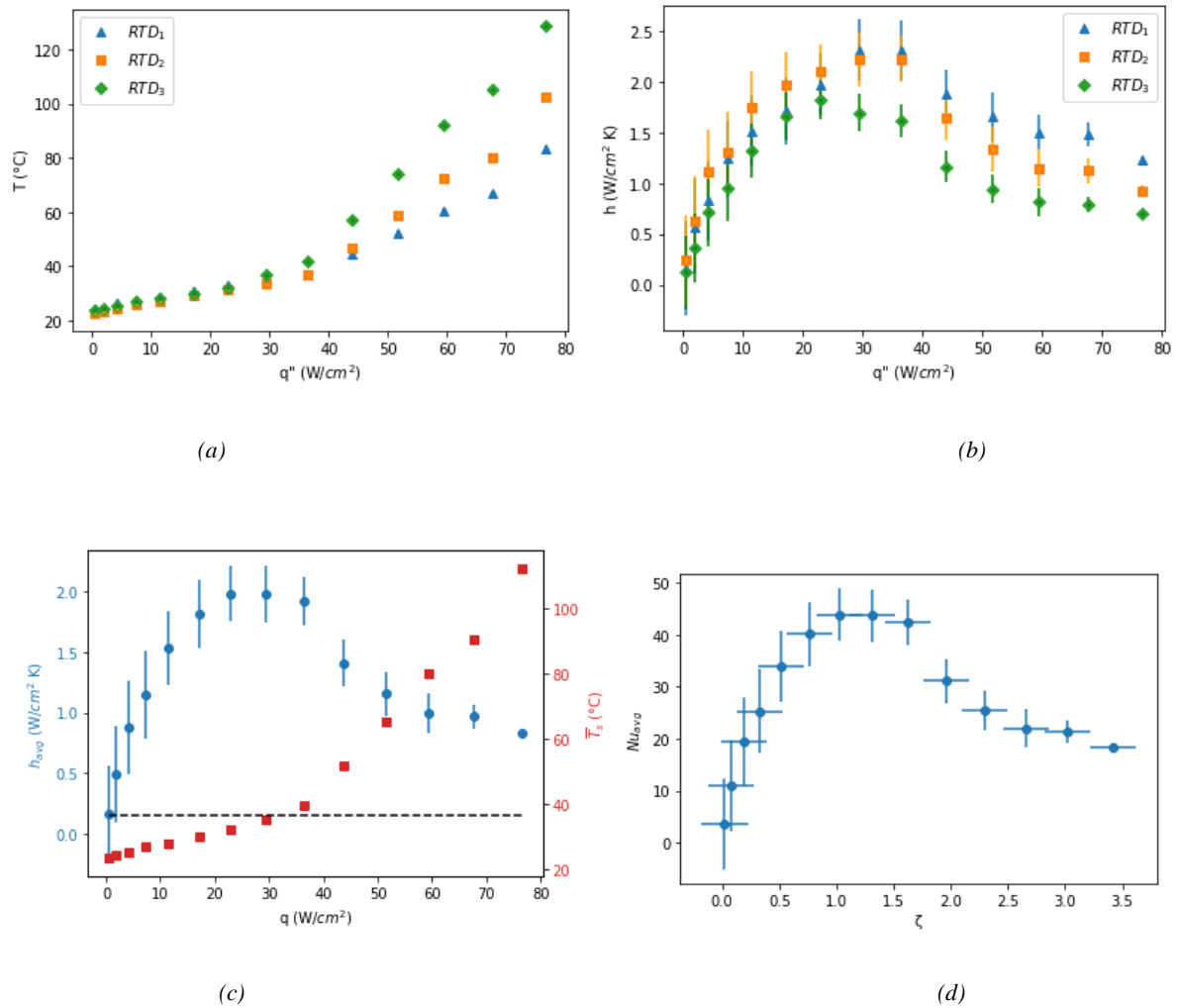


Figure 47: (a) Local surface temperature as a function of heat flux; (b) Local heat transfer coefficient as a function of heat flux. ($p = 8.0$ MPa, $T_{in} = 21.7^\circ\text{C}$, $G = 1.1$ kg/cm²s W/cm²). (c) Average heat transfer coefficient and average surface temperature as a function of heat flux.

Fig 47(b) correspondingly shows the calculated local HTC , depicting a local maxima of about 2.5 W/cm² K at RTDs 1 and 2. There exists an interplay between RTDs 1 and 2 in terms of the

maximum local HTC with RTD_2 superseding RTD_1 in the first quarter of the experiment attributed to the multi-jet effect. Contrary to a single jet where the local HTC has been proven to radially decrease with an increasing distance from the stagnation zone, multi-jets behave quite differently as the distribution of the jets incites a number of stagnation zones within the overall hydrodynamics. Similarly, as expected, the local $HTCs$ at all radial position increased until a peak before a gradual decline supported by recent research [100, 107]. Although a more uniform temperature distribution was recorded over the heater, the interject spacing, multi-jet hydrodynamics and jet arrangement were assumed to have played an important role in the heat transfer rate.

5.2.2. Mass Flux Effect

Quantitative assessment of the mass flux was conducted over a mass flux range of 1.0 to 3.3 $\text{kg}/\text{cm}^2 \text{ s}$ at an inlet pressure of 8.0MPa, an inlet temperature of 21.7 °C, and a constant heat flux of 28.35 W/cm^2 . Depicted in Fig 48(a) is the local surface temperatures over the heater as measured by the $RTDs$. As expected, the temperatures declined with increasing mass flux as a result of increased turbulence associated with increasing the Reynolds number. Similar to the observation in the heat flux effect, RTD_1 recorded the least temperatures due to its sensor fully covered by the center jet. Correspondingly, the effect of the multi jet is noticeable as the maximum temperature difference between $RTDs$ 1 and 3 was about $4 \pm 1^\circ\text{C}$. Fig 48(b) shows the area-averaged HTC with the corresponding averaged temperature over the investigated mass flux. A maximum area-averaged HTC of 3.3 $\text{W}/\text{cm}^2 \text{ k}$ was recorded at a Reynolds number of 90,000 with surface temperature farther from the pseudocritical temperature. This observation undermines the

heat flux effect on the HTC as the trend was significantly driven by the mass flux. As seen the area-averaged HTC continued to increase regardless of its proximity to the pseudocritical temperature line. Similar observation was observed in its single jet counterpart both in micro (chapter 3) and macro scale [107].

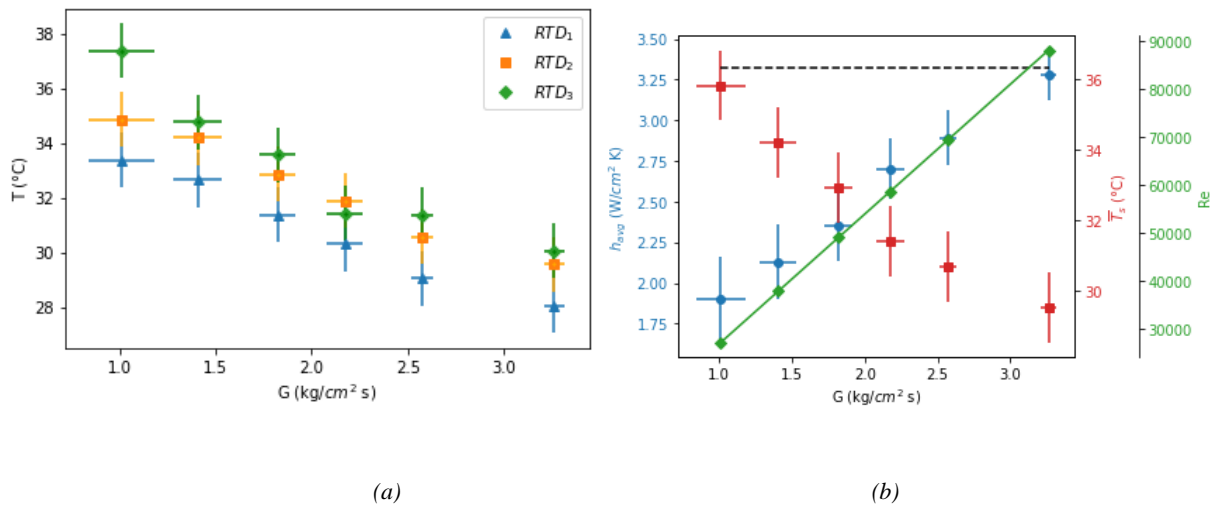


Figure 48: Mass flux effect (a) local surface temperature with increasing mass flux (b) Area-averaged HTC and temperature distribution with increasing heat flux ($p = 8.0$ MPa, $T_{in} = 21.7^\circ\text{C}$, $q'' = 28.35$ W/cm²)

5.2.3. Inlet Temperature Effect

The fluid inlet pressure was varied from 7.7 MPa to 10.3 MPa – much higher than the supercritical pressure of 7.37 MPa over a heat flux of up to 80 W/cm² at an inlet temperature of 21.7 °C, and a mass flux of 1.1 kg/cm² s. (Note that the maximum pressure drop recorded during the experiment was ~ 0.13 MPa). Fig 8(a) depicts the measured area-averaged HTC and surface temperature over the varied pressures with increasing the heat flux. Similar to the aforementioned curve in the heat flux investigation, the HTC at each isobaric line increased to a peak before a

decline with increasing heat flux. In addition, it is observed that the area-averaged HTC increased with increasing the inlet pressure with a peak HTC of $\sim 3 \text{ W/cm}^2 \text{ K}$ at 10.3 MPa pressure. This increase is attributed to the proximity to the pseudocritical temperature line where the specific heat is maximum. According to Adeoye et al [100], the pseudocritical temperature is defined according to;

$$T_{pc} = -120.9 + 6.124p - 0.1657p^2 + 0.01773p^{2.5} - 0.0005608p^3 \text{ } ^\circ\text{C} \quad (32)$$

Where p is the pressure in bar. Therefore, for a pressure of 7.7, 8.8 and 10.3 MPas, the resulting T_{pc} are respectively $34.4 \text{ } ^\circ\text{C}$, $40.66 \text{ } ^\circ\text{C}$ and $50.02 \text{ } ^\circ\text{C}$. Equation 22 states that the pseudocritical temperature increases with pressure, as a result, the pseudocritical heat flux (q''_{pc}) – defined as the heat flux needed to bring the surface temperature around the pseudocritical temperature, would increase with a pressure increase, setting a much higher threshold for the heat transfer to assume a peak according to $h \propto q''$ and the specific heat contribution.

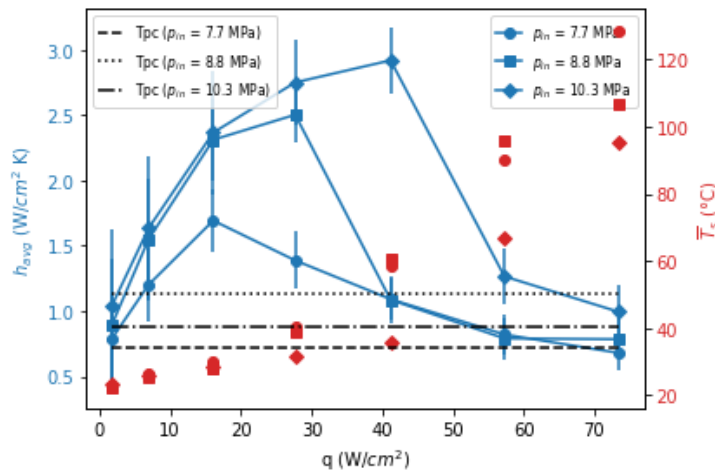


Figure 49: Pressure effect at varying heat flux

5.2.4. Comparison to Single Jet and New Correlation

To further analyze the heat transfer properties of the multi-jet, comparison was made with the single jet under similar conditions. The Nusselt number correlation as predicted in chapter 4, and Equation 25 was compared to that recorded in this chapter. As shown in Fig. 49 the exist a notable deviation at both constant Reynolds number Fig. 49(a) and dimensionless heat flux Fig. 49(b) with the single jet correlation over predicting the heat transfer rate. This observation is somewhat counterintuitive to the proposed hypothesis, as a multi-jet configuration incites a more uniform HTC over the heat dissipating devices leading to a higher area-averaged HTC. However there exist a number of driving potentials in the multi-jet hydrodynamics which significantly govern the heat transfer ability. Of these factors, is the interjet spacing which contributes to the upwash effect as detailed in Chapter 1. It is assumed that for an interjet spacing of 1.5 as recorded in this experiment, the influence of the neighboring jet is more dominant, degrading the overall heat transfer process. Although, the trend of the heat transfer is similar peaking at a $\zeta = 1$, This further validates the polynomial curve utilized in predicting the heat transfer process. Therefore, for multi jet configurations, there exists an added driving potential “S/d” in its prediction substituted for the standoff expression (r/d) as expressed in Equation 33 which fits the experimental result with a reduced MAE of 0.54. Likewise, there is a reduced dependency on the Reynolds number which is also attributed to the degradation n the overall heat transfer process brought about by the jet-to-jet interaction.

$$Nu_{avg} = 0.02Pr^{0.42}(S/d)^{-4.4}Re^{0.48}(-1.2\zeta^4 + 14.98\zeta^3 - 63.53\zeta^2 + 95.56\zeta + 22.25)^{0.94} \quad (33)$$

valid for:

$$30,000 \leq Re \leq 90,000$$

$$0 \leq \zeta \leq 5.5$$

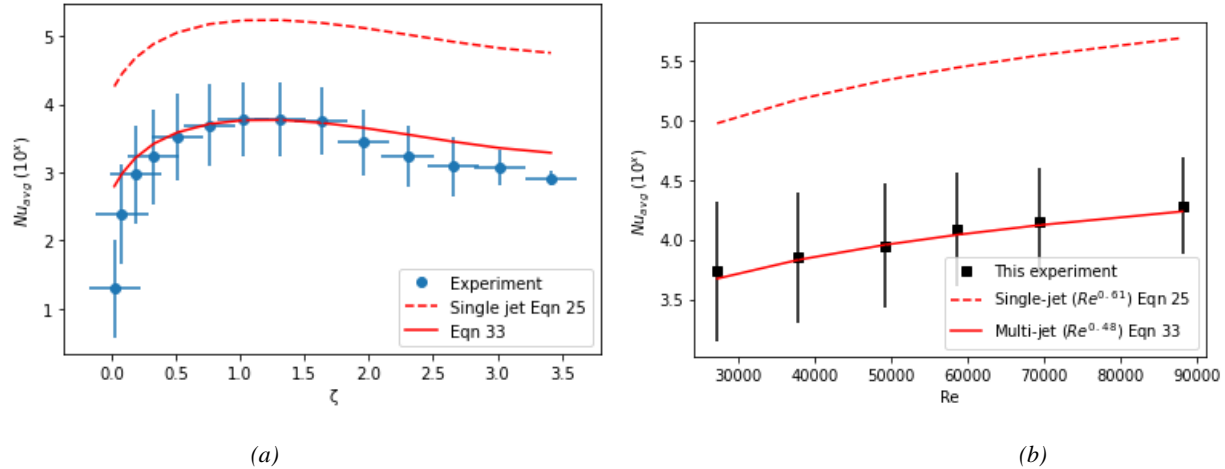


Figure 50: Comparison with single jet and proposal of new correlation (a) constant Reynolds Number (a) constant dimensionless heat flux

5.3. Conclusion

The conclusion from this experiment is highlighted below

- The multi jet behaved similar to the single jet with increasing both the heat flux and mass flux
- There exists a strong influence of the interjet spacing on the overall heat transfer rate as a smaller S/d limited the heat transfer ability when compared with the single jet
- An increase in the pressure further increased the heat transfer coefficient as a result of an increased pseudocritical temperature threshold where the maximum temperature is achieved
- The single jet correlation overpredicted the heat transfer ability which was further corrected by factoring in the interjet spacing effect.

CHAPTER SIX: FUTURE WORKS AND CONCLUSION

The heat transfer characteristics of carbon dioxide in both its single phase and two-phase conditions were experimentally studied in a micro single and multi-impinging jets. The heat transfer ability was estimated based on the temperature changes and power applied to the heat dissipating device. The heat dissipating device and temperature measurement sensors consisted of a serpentine heater and three Resistance Temperature Detectors to simultaneously supply heat and measure the temperature changes as a result of the impinging effect. The investigation was varied over a number of susceptible parameters such as the radial position, heat flux, mass flux, inlet temperature and pressure. The highlighted result from the experiments are summarized below

- For single phase cooling, there exist a strong dependence on the heat flux with the maximum heat transfer coefficient expected around the pseudocritical region – This region is characterized by a drastic jump in the specific heat which has been analyzed to contribute to more than half of the temperature distribution. Therefore, for optimum results, work must be done to raise the surface temperature with close proximity to the pseudocritical temperature of the fluid.
- With increasing the mass flux, a much higher heat transfer rate, CHF and ONB can be achieved in both single and two-phase conditions. In the single phase, the increase is as a result of an increased turbulence in the flow depicting a stronger hydrodynamic profile. While for the two-phase, other factors such as the rate of bubble generation and collapse together with the increased turbulence are suspected to have contributed to the heat transfer process

- Flow boiling can improve the heat transfer process due to its ability to maintain its temperature with increasing the heat flux up until the CHF where the effect is greatly degraded.
- The pseudocritical heat flux defined as the heat flux needed to bring the surface temperature around the pseudocritical condition is highly dependent on the inlet pressure which further increases the maximum HTC possible with a pressure increase
- There exists a strong contribution of the interjet spacing on the overall heat transfer rate due to colling jets – a consequence of jet-to-jet interaction.

Despite the promising enhancement in heat transfer brought about by these cooling technology, major issues regarding its adoption still exist. For example, the shoot up of temperature right after the CHF condition during flow boiling impacts its industrial adoption. Although many technologies have adopted phase change materials, boiling and condensation in its cooling systems, however with at very high heat fluxes, the devices could fail due to a dramatic increase in the temperature which could lead to a sudden and unexpected undermined performance. Other factors to reduce these possibilities should be further investigated. Likewise, in the line of the multi jet configuration, careful parametric study needs to examine specific contribution of the interjet spacing to the overall heat transfer process. This study can analytically dictate the optimum conditions with respect to the interjet spacing when working with multi jets. In addition, the turbulence generated with the cooling micro domain can be further improved by introducing several disturbances in the flow such as cavities, pores, pin fins, etc.

APPENDIX A: COPYRIGHT PERMISSION



Institution rights

Regardless of how the author chooses to publish with Elsevier, their institution has the right to use articles for classroom teaching and internal training. Articles can be used for these purposes throughout the author's institution, not just by the author:

Institution rights in Elsevier's proprietary journals (providing full acknowledgement of the original article is given)	All articles
Copies can be distributed electronically as well as in physical form for classroom teaching and internal training purposes	✓
Material can be included in coursework and courseware programs for use within the institution (but not in Massive Open Online Courses)	✓
Articles can be included in applications for grant funding	✓
Theses and dissertations which contain embedded final published articles as part of the formal submission can be posted publicly by the awarding institution with DOI links back to the formal publication on ScienceDirect	✓

APPENDIX B: COPYRIGHT PERMISSION

Author rights

The below table explains the rights that authors have when they publish with Elsevier, for authors who choose to publish either open access or subscription. These apply to the corresponding author and all co-authors.

Author rights in Elsevier's proprietary journals	Published open access	Published subscription
Retain patent and trademark rights	√	√
Retain the rights to use their research data freely without any restriction	√	√
Receive proper attribution and credit for their published work	√	√
Re-use their own material in new works without permission or payment (with full acknowledgement of the original article): 1. Extend an article to book length 2. Include an article in a subsequent compilation of their own work 3. Re-use portions, excerpts, and their own figures or tables in other works.	√	√
Use and share their works for scholarly purposes (with full acknowledgement of the original article): 1. In their own classroom teaching. Electronic and physical distribution of copies is permitted 2. If an author is speaking at a conference, they can present the article and distribute	√	√

LIST OF REFERENCES

1. Moore's law.
2. Lawes, R.A., *Manufacturing costs for microsystems/MEMS using high aspect ratio microfabrication techniques*. Microsystem Technologies, 2007. **13**(1): p. 85-95.
3. Teh, K.S., *Additive direct-write microfabrication for MEMS: A review*. Frontiers of Mechanical Engineering, 2017. **12**(4): p. 490-509.
4. Wagner, B., et al., *Microfabrication of complex surface topographies using grey-tone lithography*. Sensors and Actuators A: Physical, 1995. **46**(1): p. 89-94.
5. Abdoli, A., G. Jimenez, and G.S. Dulikravich, *Thermo-fluid analysis of micro pin-fin array cooling configurations for high heat fluxes with a hot spot*. International Journal of Thermal Sciences, 2015. **90**: p. 290-297.
6. Smakulski, P. and S. Pietrowicz, *A review of the capabilities of high heat flux removal by porous materials, microchannels and spray cooling techniques*. Applied Thermal Engineering, 2016. **104**: p. 636-646.
7. Bar-Cohen, A., P. Wang, and E. Rahim, *Thermal management of high heat flux nanoelectronic chips*. Microgravity Science and Technology, 2007. **19**(3): p. 48-52.
8. Usman, H., et al., *An experimental study of PCM based finned and un-finned heat sinks for passive cooling of electronics*. Heat and Mass Transfer, 2018. **54**(12): p. 3587-3598.
9. Fan, A., et al. *An innovative passive cooling method for high performance light-emitting diodes*. in *2012 28th Annual IEEE Semiconductor Thermal Measurement and Management Symposium (SEMI-THERM)*. 2012.

10. Kothari, R., et al., *Experimental Investigations on Thermal Performance of PCM Based Heat Sink for Passive Cooling of Electronic Components*, in *ASME 2018 16th International Conference on Nanochannels, Microchannels, and Minichannels*. 2018.
11. Wani, F., et al., *A Study on Passive Cooling in Subsea Power Electronics*. *IEEE Access*, 2018. **6**: p. 67543-67554.
12. Liang, K., et al., *Comparisons between heat pipe, thermoelectric system, and vapour compression refrigeration system for electronics cooling*. *Applied Thermal Engineering*, 2019. **146**: p. 260-267.
13. Vandaele, K., et al., *Wet-Chemical Synthesis of Enhanced-Thermopower $\text{Bi}_2\text{Te}_3/\text{Sb}_2\text{Te}_3$ Nanowire Composites for Solid-State Active Cooling of Electronics*. *Physical Review Applied*, 2018. **9**(2): p. 024020.
14. Jang, S.P. and S.U.S. Choi, *Cooling performance of a microchannel heat sink with nanofluids*. *Applied Thermal Engineering*, 2006. **26**(17): p. 2457-2463.
15. Sidik, N.A.C., et al., *An overview of passive techniques for heat transfer augmentation in microchannel heat sink*. *International Communications in Heat and Mass Transfer*, 2017. **88**: p. 74-83.
16. Husain, A., et al., *Thermal performance analysis of a hybrid micro-channel, -pillar and -jet impingement heat sink*. *Applied Thermal Engineering*, 2016. **102**: p. 989-1000.
17. Husain, A., S.-M. Kim, and K.-Y. Kim, *Performance analysis and design optimization of micro-jet impingement heat sink*. *Heat and Mass Transfer*, 2013. **49**(11): p. 1613-1624.
18. Shin, J.-H., et al., *Local heat transfer under an array of micro jet impingement using HFE-7000*. *Applied Thermal Engineering*, 2019. **158**: p. 113716.

19. Lu, X., et al., *Flow and heat transfer characteristics of micro pin-fins under jet impingement arrays*. International Journal of Heat and Mass Transfer, 2019. **143**: p. 118416.
20. Cheng, L., G. Ribatski, and J.R. Thome, *Analysis of supercritical CO₂ cooling in macro- and micro-channels*. International Journal of Refrigeration, 2008. **31**(8): p. 1301-1316.
21. Ndao, S., et al., *Heat transfer enhancement from micro pin fins subjected to an impinging jet*. International Journal of Heat and Mass Transfer, 2012. **55**(1): p. 413-421.
22. Zhang, Y., et al., *Confined Submerged Jet Impingement Boiling of Subcooled FC-72 over Micro-Pin-Finned Surfaces*. Heat Transfer Engineering, 2016. **37**(3-4): p. 269-278.
23. Kim, T., et al., *Highly nanotextured nickel-electroplated bismuth vanadate micropillars for hotspot removal via air- and spray-cooling*. International Journal of Heat and Mass Transfer, 2020. **156**: p. 119731.
24. Glynn, C., T. O'Donovan, and D. Murray, *Jet Impingement Cooling*. Proceedings of the 9th UK National Heat Transfer Conference, 2005.
25. Draksler, M. and B. Končar, *Analysis of heat transfer and flow characteristics in turbulent impinging jet*. Nuclear Engineering and Design, 2011. **241**(4): p. 1248-1254.
26. Li, Q., Y. Xuan, and F. Yu, *Experimental investigation of submerged single jet impingement using Cu–water nanofluid*. Applied Thermal Engineering, 2012. **36**: p. 426-433.
27. Zhang, P., et al., *Confined jet impingement of liquid nitrogen onto different heat transfer surfaces*. Cryogenics, 2011. **51**(6): p. 300-308.

28. Garimella, S.V., *Heat Transfer and Flow Fields in Confined Jet Impingement*. Annual Review of Heat Transfer, 2000. **11**: p. 413-494.
29. Anand, K. and B. Jubran, *Study of Single, Axisymmetric Micro Jet-Impingement Cooling*. 2010.
30. Choo, K.S., et al., *Heat transfer characteristics of a micro-scale impinging slot jet*. International Journal of Heat and Mass Transfer, 2009. **52**(13): p. 3169-3175.
31. Huang, X., et al., *Heat transfer enhancement on a microchannel heat sink with impinging jets and dimples*. International Journal of Heat and Mass Transfer, 2017. **112**: p. 113-124.
32. Glynn, C. and D.B. Murray. *Jet impingement cooling in microscale*. in *ECI International Conference on Heat Transfer and Fluid Flow in Microscale*. 2005.
33. Hatta, N., J.-i. Kokado, and K. Hanasaki, *Numerical Analysis of Cooling Characteristics for Water Bar*. Transactions of the Iron and Steel Institute of Japan, 1983. **23**(7): p. 555-564.
34. Ishida, R., et al., *Basic Characteristics of Pipe Nozzle Cooling with Retaining Water on Plate*. ISIJ International, 1989. **29**(4): p. 339-344.
35. Hatta, N. and H. Osakabe, *Numerical Modeling for Cooling Process of a Moving Hot Plate by a Laminar Water Curtain*. ISIJ International, 1989. **29**(11): p. 919-925.
36. Katti, V. and S. Prabhu, *Experimental study and theoretical analysis of local heat transfer distribution between smooth flat surface and impinging air jet from a circular straight pipe nozzle*. International Journal of Heat and Mass Transfer, 2008. **51**: p. 4480-4495.

37. Al-Sanea, S., *A numerical study of the flow and heattransfer characteristics of an impinging laminar slot-jet including crossflow effects*. International Journal of Heat and Mass Transfer, 1992. **35**(10): p. 2501-2513.
38. Ma, C.F., et al., *Analytical study on impingement heat transfer with single-phase free-surface circular liquid jets*. Journal of Thermal Science, 1996. **5**(4): p. 271-277.
39. Martin, H., *Heat and Mass Transfer between Impinging Gas Jets and Solid Surfaces*, in *Advances in Heat Transfer*, J.P. Hartnett and T.F. Irvine, Editors. 1977, Elsevier. p. 1-60.
40. Webb, B.W. and C.F. Ma, *Single-Phase Liquid Jet Impingement Heat Transfer*, in *Advances in Heat Transfer*, J.P. Hartnett and T.F. Irvine, Editors. 1995, Elsevier. p. 105-217.
41. Browne, E.A., et al., *Microjet array single-phase and flow boiling heat transfer with R134a*. International Journal of Heat and Mass Transfer, 2010. **53**(23): p. 5027-5034.
42. Sleiti, A.K. and J.S. Kapat, *An Experimental Investigation of Liquid Jet Impingement and Single-Phase Spray Cooling Using Polyalphaolefin*. Experimental Heat Transfer, 2006. **19**(2): p. 149-163.
43. Miyasaka, Y. and S. Inada, *THE EFFECT OF PURE FORCED CONVECTION ON THE BOILING HEAT TRANSFER BETWEEN A TWO-DIMENSIONAL SUBCOOLED WATER JET AND A HEATED SURFACE*. Journal of Chemical Engineering of Japan, 1980. **13**(1): p. 22-28.
44. Ndao, S., Y. Peles, and M.K. Jensen, *Experimental investigation of flow boiling heat transfer of jet impingement on smooth and micro structured surfaces*. International Journal of Heat and Mass Transfer, 2012. **55**(19): p. 5093-5101.

45. Wolf, D.H., F.P. Incropera, and R. Viskanta, *Jet Impingement Boiling*, in *Advances in Heat Transfer*, J.P. Hartnett and T.F. Irvine, Editors. 1993, Elsevier. p. 1-132.
46. Liu, Z.-H. and Q.-Z. Zhu, *Prediction of Critical Heat Flux for Convective Boiling of Saturated Water Jet Impinging on the Stagnation Zone*. *Journal of Heat Transfer*, 2002. **124**(6): p. 1125-1130.
47. Qiu, Y.-h. and Z.-h. Liu, *Critical heat flux of steady boiling for saturated liquids jet impinging on the stagnation zone*. *International Journal of Heat and Mass Transfer*, 2005. **48**(21): p. 4590-4597.
48. Zhao, Z., Y. Peles, and M.K. Jensen, *Water jet impingement boiling from structured-porous surfaces*. *International Journal of Heat and Mass Transfer*, 2013. **63**: p. 445-453.
49. Zhou, D.W. and C.F. Ma, *Local jet impingement boiling heat transfer with R113*. *Heat and Mass Transfer*, 2004. **40**(6): p. 539-549.
50. Ma, C.F., Q. Zheng, and S.Y. Ko, *Local heat transfer and recovery factor with impinging free-surface circular jets of transformer oil*. *International Journal of Heat and Mass Transfer*, 1997. **40**(18): p. 4295-4308.
51. Du, M., et al., *Experimental and numerical investigation on flow and heat transfer of impingement jet cooling of kerosene*. *International Communications in Heat and Mass Transfer*, 2020. **116**: p. 104644.
52. Tiggelaar, R.M., et al., *Fabrication, mechanical testing and application of high-pressure glass microreactor chips*. *Chemical Engineering Journal*, 2007. **131**(1): p. 163-170.

53. Marre, S., et al., *Design and Packaging of Microreactors for High Pressure and High Temperature Applications*. Industrial & Engineering Chemistry Research, 2010. **49**(22): p. 11310-11320.
54. Lerou, P.P.P.M., et al. *Progress in Micro Joule-Thomson Cooling at Twente University*. in *Cryocoolers 13*. 2005. Boston, MA: Springer US.
55. Womac, D.J., F.P. Incropera, and S. Ramadhyani, *Correlating Equations for Impingement Cooling of Small Heat Sources With Multiple Circular Liquid Jets*. Journal of Heat Transfer, 1994. **116**(2): p. 482-486.
56. Incropera, F., et al., *Fundamentals of Heat and Mass Transfer*. 2007.
57. Hollworth, B.R. and S.I. Wilson, *Entrainment Effects on Impingement Heat Transfer: Part I—Measurements of Heated Jet Velocity and Temperature Distributions and Recovery Temperatures on Target Surface*. Journal of Heat Transfer, 1984. **106**(4): p. 797-803.
58. Gardon, R. and J.C. Akfirat, *The role of turbulence in determining the heat-transfer characteristics of impinging jets*. International Journal of Heat and Mass Transfer, 1965. **8**(10): p. 1261-1272.
59. Saripalli, K.R., *Visualization of multijet impingement flow*. AIAA Journal, 1983. **21**(4): p. 483-484.
60. San, J.-Y. and J.-J. Chen, *Effects of jet-to-jet spacing and jet height on heat transfer characteristics of an impinging jet array*. International Journal of Heat and Mass Transfer, 2014. **71**: p. 8-17.

61. Obot, N.T. and T.A. Trabold, *Impingement Heat Transfer Within Arrays of Circular Jets: Part 1—Effects of Minimum, Intermediate, and Complete Crossflow for Small and Large Spacings*. Journal of Heat Transfer, 1987. **109**(4): p. 872-879.
62. Pachpute, S. and B. Premachandran, *Turbulent multi-jet impingement cooling of a heated circular cylinder*. International Journal of Thermal Sciences, 2020. **148**: p. 106167.
63. Xing, Y., S. Spring, and B. Weigand, *Experimental and Numerical Investigation of Heat Transfer Characteristics of Inline and Staggered Arrays of Impinging Jets*. Journal of Heat Transfer, 2010. **132**(9).
64. Van Treuren, K.W., et al., *Comparison and Prediction of Local and Average Heat Transfer Coefficients Under an Array of Inline and Staggered Impinging Jets*, in *ASME 1996 International Gas Turbine and Aeroengine Congress and Exhibition*. 1996.
65. Jackson, D. and B. Launder, *Osborne Reynolds and the Publication of His Papers on Turbulent Flow*. Annual Review of Fluid Mechanics, 2006. **39**(1): p. 19-35.
66. Garimella, S.V. and R.A. Rice, *Confined and Submerged Liquid Jet Impingement Heat Transfer*. Journal of Heat Transfer, 1995. **117**(4): p. 871-877.
67. Garimella, S.V. and V.P. Schroeder, *Local Heat Transfer Distributions in Confined Multiple Air Jet Impingement*. Journal of Electronic Packaging, 2000. **123**(3): p. 165-172.
68. Florschuetz, L.W., C.R. Truman, and D.E. Metzger, *Streamwise Flow and Heat Transfer Distributions for Jet Array Impingement With Crossflow*, in *ASME 1981 International Gas Turbine Conference and Products Show*. 1981.

69. Kercher, D.M. and W. Tabakoff, *Heat Transfer by a Square Array of Round Air Jets Impinging Perpendicular to a Flat Surface Including the Effect of Spent Air*. Journal of Engineering for Power, 1970. **92**(1): p. 73-82.
70. Robinson, A.J. and E. Schnitzler, *An experimental investigation of free and submerged miniature liquid jet array impingement heat transfer*. Experimental Thermal and Fluid Science, 2007. **32**(1): p. 1-13.
71. Zumbrennen, D.A. and M. Aziz, *Convective Heat Transfer Enhancement Due to Intermittency in an Impinging Jet*. Journal of Heat Transfer, 1993. **115**(1): p. 91-98.
72. Baughn, J.W. and S. Shimizu, *Heat transfer measurements from a surface with uniform heat flux and an impinging jet*. 1989. **111**:4.
73. Lee, J.L.S.-J., *STAGNATION REGION HEAT TRANSFER OF A TURBULENT AXISYMMETRIC JET IMPINGEMENT*. Experimental Heat Transfer, 1999. **12**(2): p. 137-156.
74. Stevens, J. and B.W. Webb, *The effect of inclination on local heat transfer under an axisymmetric, free liquid jet*. International Journal of Heat and Mass Transfer, 1991. **34**: p. 1227-1236.
75. Lytle, D. and B.W. Webb, *Air jet impingement heat transfer at low nozzle-plate spacings*. International Journal of Heat and Mass Transfer, 1994. **37**(12): p. 1687-1697.
76. Choo, K., et al., *The influence of nozzle-to-plate spacing on heat transfer and fluid flow of submerged jet impingement*. International Journal of Heat and Mass Transfer, 2016. **97**: p. 66-69.

77. Brechet, Y. and Z. Néda, *On the circular hydraulic jump*. American Journal of Physics, 1999. **67**(8): p. 723-731.
78. Kuraan, A.M., S.I. Moldovan, and K. Choo, *Heat transfer and hydrodynamics of free water jet impingement at low nozzle-to-plate spacings*. International Journal of Heat and Mass Transfer, 2017. **108**: p. 2211-2216.
79. Pearson, A., *Carbon dioxide—new uses for an old refrigerant*. International Journal of Refrigeration, 2005. **28**(8): p. 1140-1148.
80. Dadashev, M.N. and G.V. Stepanov, *Supercritical extraction in petroleum refining and petrochemistry*. Chemistry and Technology of Fuels and Oils, 2000. **36**(1): p. 8-13.
81. Raventós, M., S. Duarte, and R. Alarcón, *Application and Possibilities of Supercritical CO₂ Extraction in Food Processing Industry: An Overview*. Food Science and Technology International, 2002. **8**(5): p. 269-284.
82. Sahena, F., et al., *Application of supercritical CO₂ in lipid extraction – A review*. Journal of Food Engineering, 2009. **95**(2): p. 240-253.
83. Sarrade, S., C. Guizard, and G.M. Rios, *New applications of supercritical fluids and supercritical fluids processes in separation*. Separation and Purification Technology, 2003. **32**(1): p. 57-63.
84. Yamaguchi, H., et al., *Preliminary Study on a Solar Water Heater Using Supercritical Carbon Dioxide as Working Fluid*. Journal of Solar Energy Engineering, 2010. **132**(1).
85. Hsieh, J.C., et al., *The Heat Extraction Investigation of Supercritical Carbon Dioxide Flow in Heated Porous Media*. Energy Procedia, 2014. **61**: p. 262-265.

86. Zhang, L., et al., *Heat Transfer and Fluid Transport of Supercritical CO₂ in Enhanced Geothermal System with Local Thermal Non-equilibrium Model*. Energy Procedia, 2014. **63**: p. 7644-7650.
87. Gupta, S., et al., *Developing empirical heat-transfer correlations for supercritical CO₂ flowing in vertical bare tubes*. Nuclear Engineering and Design, 2013. **261**: p. 116-131.
88. Cavallini, A., D. Del Col, and L. Rossetto, *Heat transfer and pressure drop of natural refrigerants in minichannels (low charge equipment)*. International Journal of Refrigeration, 2013. **36**(2): p. 287-300.
89. Machida, H., M. Takesue, and R.L. Smith, *Green chemical processes with supercritical fluids: Properties, materials, separations and energy*. The Journal of Supercritical Fluids, 2011. **60**: p. 2-15.
90. Zalba, B., et al., *Review on thermal energy storage with phase change: materials, heat transfer analysis and applications*. Applied Thermal Engineering, 2003. **23**(3): p. 251-283.
91. Oh, H.-K. and C.-H. Son, *Flow boiling heat transfer and pressure drop characteristics of CO₂ in horizontal tube of 4.57-mm inner diameter*. Applied Thermal Engineering, 2011. **31**(2): p. 163-172.
92. Monde, M. and Y. Katto, *Burnout in a high heat-flux boiling system with an impinging jet*. International Journal of Heat and Mass Transfer, 1978. **21**(3): p. 295-305.
93. Cooper, M.G., *Heat Flow Rates in Saturated Nucleate Pool Boiling-A Wide-Ranging Examination Using Reduced Properties*, in *Advances in Heat Transfer*, J.P. Hartnett and T.F. Irvine, Editors. 1984, Elsevier. p. 157-239.

94. Zhang, Y. and W. Chen, *Experimental Study on Jet Impingement Boiling Heat Transfer in Brass Beads Packed Porous Layer*. Journal of Thermal Science, 2020. **29**(3): p. 718-729.
95. Wolf, D.H., F.P. Incropera, and R. Viskanta, *Local jet impingement boiling heat transfer*. International Journal of Heat and Mass Transfer, 1996. **39**(7): p. 1395-1406.
96. Qiu, Y.-h. and Z.-h. Liu, *Nucleate boiling on the superhydrophilic surface with a small water impingement jet*. International Journal of Heat and Mass Transfer, 2008. **51**(7): p. 1683-1690.
97. Katto, Y. and C. Kurata, *Critical heat flux of saturated convective boiling on uniformly heated plates in a parallel flow*. International Journal of Multiphase Flow, 1980. **6**(6): p. 575-582.
98. Katto, Y. and S. Yokoya, *Critical heat flux on a disk heater cooled by a circular jet of saturated liquid impinging at the center*. International Journal of Heat and Mass Transfer, 1988. **31**(2): p. 219-227.
99. Liu, Z.-H., T.-F. Tong, and Y.-H. Qiu, *Critical Heat Flux of Steady Boiling for Subcooled Water Jet Impingement on the Flat Stagnation Zone*. Journal of Heat Transfer, 2004. **126**(2): p. 179-183.
100. Adeoye, S., A. Parahovnik, and Y. Peles, *A micro impinging jet with supercritical carbon dioxide*. International Journal of Heat and Mass Transfer, 2021. **170**: p. 121028.
101. Adeoye, S. and Y. Peles, *Flow boiling of carbon dioxide with a micro impinging jet*. International Journal of Heat and Mass Transfer, 2022. **187**: p. 122495.
102. Overholt, M.R., et al., *Micro-Jet Arrays for Cooling of Electronic Equipment*, in *ASME 3rd International Conference on Microchannels and Minichannels*. 2005. p. 249-252.

103. Shen, C.H. and C. Gau. *Heat exchanger fabrication with arrays of sensors and heaters with its micro-scale impingement cooling process analysis and measurements.* in *TRANSDUCERS '03. 12th International Conference on Solid-State Sensors, Actuators and Microsystems. Digest of Technical Papers (Cat. No.03TH8664).* 2003.
104. Patil, V.A. and V. Narayanan, *Spatially Resolved Heat Transfer Rates in an Impinging Circular Microscale Jet.* *Microscale Thermophysical Engineering*, 2005. **9**(2): p. 183-197.
105. Browne, E., et al., *Experimental Investigation of Single-Phase Microjet Array Heat Transfer.* *Journal of Heat Transfer-transactions of The Asme - J HEAT TRANSFER*, 2010. **132**.
106. Wen, T., H. Zhan, and D. Zhang, *Flow condensation heat transfer characteristics of R134a in multiport mini-channel by jet impingement cooling.* *Applied Thermal Engineering*, 2019. **147**: p. 399-409.
107. Chen, K., R.-N. Xu, and P.-X. Jiang, *Experimental Investigation of Jet Impingement Cooling With Carbon Dioxide at Supercritical Pressures.* *Journal of Heat Transfer*, 2018. **140**(4).
108. Joo-Kyun, K. and A. Toshio, *A numerical study of heat transfer due to an axisymmetric laminar impinging jet of supercritical carbon dioxide.* *International Journal of Heat and Mass Transfer*, 1992. **35**(10): p. 2515-2526.
109. Chen, K., et al., *Numerical Investigation of Jet Impingement Cooling of a Flat Plate with Carbon Dioxide at Supercritical Pressures.* *Heat Transfer Engineering*, 2018. **39**(2): p. 85-97.

110. Cabeza, L.F., et al., *Supercritical CO₂ as heat transfer fluid: A review*. Applied Thermal Engineering, 2017. **125**: p. 799-810.
111. Hofmann, H.M., M. Kind, and H. Martin, *Measurements on steady state heat transfer and flow structure and new correlations for heat and mass transfer in submerged impinging jets*. International Journal of Heat and Mass Transfer, 2007. **50**(19): p. 3957-3965.
112. Wen, M.-Y. and K.-J. Jang, *An impingement cooling on a flat surface by using circular jet with longitudinal swirling strips*. International Journal of Heat and Mass Transfer, 2003. **46**(24): p. 4657-4667.
113. Tawfek, A.A., *Heat transfer and pressure distributions of an impinging jet on a flat surface*. Heat and Mass Transfer, 1996. **32**(1): p. 49-54.
114. Goldstein, R.J. and A.I. Behbahani, *Impingement of a circular jet with and without cross flow*. International Journal of Heat and Mass Transfer, 1982. **25**(9): p. 1377-1382.
115. Shi, Y., M.B. Ray, and A.S. Mujumdar, *Effects of prandtl number on impinging jet heat transfer under a semi-confined turbulent slot jet*. 2002.
116. Wang, J., et al., *Comparison of the heat transfer characteristics of supercritical pressure water to that of subcritical pressure water in vertically-upward tubes*. International Journal of Multiphase Flow, 2011. **37**(7): p. 769-776.
117. Özdemir, M.R., M.M. Mahmoud, and T.G. Karayiannis, *Flow Boiling of Water in a Rectangular Metallic Microchannel*. Heat Transfer Engineering, 2021. **42**(6): p. 492-516.
118. Bortolin, S., et al., *Flow boiling of R134a and HFE-7000 in a single silicon microchannel with microstructured sidewalls*. International Journal of Heat and Mass Transfer, 2021. **179**: p. 121653.

119. Sitharamayya, S. and K.S. Raju, *Heat transfer between an axisymmetric jet and a plate held normal to the flow*. The Canadian Journal of Chemical Engineering, 1969. **47**(4): p. 365-368.
120. Cardenas, R. and V. Narayanan, *Heat transfer characteristics of submerged jet impingement boiling of saturated FC-72*. International Journal of Heat and Mass Transfer, 2012. **55**(15): p. 4217-4231.
121. Chen, K., R.-N. Xu, and P.-X. Jiang, *Experimental study of jet impingement boiling cooling with CO₂ at subcritical pressures and comparisons with at supercritical pressures*. International Journal of Heat and Mass Transfer, 2021. **165**: p. 120605.
122. Choi, K.-I., A.S. Pamitran, and J.-T. Oh, *Two-phase flow heat transfer of CO₂ vaporization in smooth horizontal minichannels*. International Journal of Refrigeration, 2007. **30**(5): p. 767-777.
123. Gorenflo, D. and S. Kotthoff, *Review on pool boiling heat transfer of carbon dioxide*. International Journal of Refrigeration, 2005. **28**(8): p. 1169-1185.
124. Yun, R., Y. Kim, and M. Soo Kim, *Flow boiling heat transfer of carbon dioxide in horizontal mini tubes*. International Journal of Heat and Fluid Flow, 2005. **26**(5): p. 801-809.
125. Wang, X. and M. Monde, *Critical heat flux in forced convective subcooled boiling with a plane wall jet (effect of subcooling on CHF)*. Heat and Mass Transfer, 1997. **33**(1): p. 167-175.

126. Katto, Y. and K. Ishii. *Burnout in a high heat flux boiling system with a forced supply of liquid through a plane jet.* in *International Heat Transfer Conference Digital Library.* 1978. Begel House Inc.
127. Haramura, Y. and Y. Katto, *A new hydrodynamic model of critical heat flux, applicable widely to both pool and forced convection boiling on submerged bodies in saturated liquids.* International Journal of Heat and Mass Transfer, 1983. **26**(3): p. 389-399.
128. Mitsutake, Y. and M. Monde, *Ultra high critical heat flux during forced flow boiling heat transfer with an impinging jet.* J. Heat Transfer, 2003. **125**(6): p. 1038-1045.